

DESIGN AND FABRICATION OF DIFFRACTIVE LENSES FOR VISIBLE AND
NEAR INFARED WAVELENGTHS

By

NARADA MUNI BRADMAN

A DISSERTATION PRESENTED TO THE GRADUATE SCHOOL
OF THE UNIVERSITY OF FLORIDA IN PARTIAL FULFILLMENT
OF THE REQUIREMENTS FOR THE DEGREE OF
DOCTOR OF PHILOSOPHY

UNIVERSITY OF FLORIDA

2007

© 2007 Narada Muni Bradman

To Pita and Mata

ACKNOWLEDGMENTS

I would like to acknowledge and thank some of those who have helped and hurried me on this wonderful journey. First and foremost, I must thank my Mother and my Father, who were my first teachers and whose unwavering love and support has sustained me throughout my life.

I would like to thank my advisor, Dr. Holloway, for his insightful guidance and for his remarkable patience. I am grateful for the advice and assistance of all of my committee members, Dr. Hummel, Dr. Tanner, Dr. Sigmund and most especially Dr. Mark Davidson. I could not have completed this research without Mark's vast knowledge of all the fabrication equipment I had to use and his assistance in repairing them.

I am especially thankful for the friendship and help of all Dr. Holloway's group members. They created an environment that was truly a joy to work in. I must especially thank Dr. Hsiu Hsin "Hannah" Chung to whom I am eternally indebted for her invaluable collaboration. Special thanks are owed to our group's permanent member, Miss Ludie Harmon, whose expertise and dedication are without compare.

I would like to thank all of my friends in the Hare Krishna community here in Alachua and around the world, who are too numerous to mention individually but whose love and support was greatly appreciated.

Finally, I must thank my dearest Roopa, for her constant encouragement, and for her patience.

TABLE OF CONTENTS

	<u>page</u>
ACKNOWLEDGMENTS	iv
LIST OF TABLES	viii
LIST OF FIGURES	ix
ABSTRACT	xiv
CHAPTER	
1 INTRODUCTION	1
2 LITERATURE REVIEW	3
2.1 Introduction.....	3
2.2 Optical Focusing Systems.....	4
2.3 Diffraction Theory	7
2.3.1 Fresnel and Fraunhofer Diffraction Theory	8
2.3.2 Fraunhofer Diffraction from a Single Rectangular Slit.....	10
2.3.3 Fraunhofer Diffraction from Double Slits.....	13
2.3.4 Fraunhofer Diffraction from Rectangular and Circular Apertures.....	14
2.3.5 Fresnel Diffraction.....	16
2.3.6 Fresnel Zone Plates.....	18
2.3.7 Photon Sieves	20
2.4 Applications of Diffractive Lens	26
2.5 Impetus for Research	26
3 EXPERIMENTAL PROCEDURE	28
3.1 Introduction.....	28

3.2	Photon sieve Fabrication.....	28
3.2.1	Substrate Preparation.....	30
3.2.1.1	Substrate clean.....	30
3.2.1.2	Thin film deposition	30
3.2.1.3	Application of resist	32
3.2.2	Lithographic Patterning.....	35
3.2.2.1	Pattern generation.....	35
3.2.2.2	Electron beam lithography	35
3.2.2.4	Electron beam lithography issues and optimization.....	38
3.2.3	Pattern Transfer	40
3.2.3.1	Sputter etching.....	41
3.2.3.2	Resist removal.....	43
3.2.3.3	Pattern transfer issues and optimization.....	43
3.3	Conclusions.....	45
4	PHOTON SIEVE PROPERTIES	46
4.1	Introduction.....	46
4.2	Characterization.....	47
4.2.1	Characterization Equipment	47
4.2.2	Characterization Procedures.....	51
4.3	Photon Sieve Design Variations	52
4.3.1	Photon Sieves with Various Degrees of Apodization	54
4.3.2	Hybrid Lenses with Circular Apertures.....	70
4.3.3	Segmented Zones.....	78
4.3.4	Large Aspect Ratio Zone Segments Lenses	87
4.4	Results and Discussion	94
4.5	Summary and Conclusions	107
5	CONCLUSIONS	109
5.1	Diffractive Lens Fabrication.....	109
5.2	Diffractive Lens Properties.....	110
5.3	Conclusions.....	111
6	FUTURE WORK.....	112

APPENDIX: MACROS USED TO GENERATE PATTERNS.....	115
Fresnel Zone Plate Macro.....	115
Photon Sieve Macro.....	117
LIST OF REFERENCES.....	122
BIOGRAPHICAL SKETCH.....	129

LIST OF TABLES

<u>Table</u>	<u>page</u>
2-1 Equations defining apodization functions	23
3-1 Spin Coater Parameters	33
3-2 Sputter Etch Parameters	42
4-1 Photon sieve designs	55
4-2 Calculated open area of FZP and various photon sieve patterns with circular apertures	62
4-3 Calculated open area of hybrid photon sieve patterns.....	71
4-4 Comparison of total open areas of hybrid photon sieve designs with circular versus segmented apertures	80
4-5 Calculated open area of hybrid photon sieves w/segmented zone apertures	88
4-6 Measured Focal Lengths vs. Lens design.....	95
4-7 Measured transmission and calculated open area for different designs and FZP ...	99
4-8 Resolution Test.....	106

LIST OF FIGURES

<u>Figure</u>	<u>page</u>
2-1 Components of a human eye	4
2-2 Snell's law of refraction.	5
2-3 An example of a Fresnel Zone Plate.	7
2-4 Diffraction from a slit.	9
2-5 Fraunhofer diffraction through a single slit.	10
2-6 Location of minima in Fraunhofer diffraction from a single slit	12
2-7 Fraunhofer diffraction through a double slit.	13
2-8 Diffraction pattern resulting from light incident on a square aperture.	14
2-9 The Airy Disc	15
2-10 Bessel function of the first kind zero order	16
2-11 Cornu's Spiral.	18
2-12 An aperture illuminated by a source at infinity.	18
2-13 The Rayleigh criterion.	20
2-14 The photon sieve.	21
2-15 Commonly used apodization functions.	23
2-16 Intensity distributions for an apodized photon sieve and a Fresnel zone plate.	24
2-17 Amplitude of contribution from enlarged apertures.	25

3-1	Overview of the diffractive lens fabrication process	29
3-2	Electron beam evaporator system.	31
3-2	PMMA thin film thickness as a function of spin speed as specified by the manufacturer.....	34
3-3	DesignCad pattern of the Fresnel zone plate.....	35
3-4	NPGS run file.....	36
3-5	PlasmaTherm ECR etching system schematic.....	41
4-1	Spectral power distribution for the LS-1 illumination source.....	47
4-2	Measured spectral distribution of filtered source illumination	48
4-3	Schematic of optical rail.....	49
4-4	Apertures for resolution test and modified test setup.....	50
4-5	Schematic of optical bench used for transmission measurements.. ..	51
4-6	A photon sieve created by populating the even Fresnel zones with a maximum density of circular apertures	59
4-7	Calculated transmission window of a FZP and photon sieves with circular apertures, with and without apodization.....	61
4-8	Measured transmissions of the Fresnel zone plate (FZP), unapodized photon sieve, 25%, 50%, and 75% apodized photon sieves.....	62
4-9	The Fresnel zone plate.....	64
4-10	Unapodized photon sieve.. ..	65
4-11	25% apodized photon sieve.....	66
4-12	50% apodized photon sieve.....	67
4-13	75% apodized photon sieve.....	68

4-14	Intensity of first order peak.....	69
4-15	FWHM of first order peaks.....	69
4-16	Calculated area versus zone number for hybrid photon sieves with circular apertures and different degrees of apodization.....	72
4-17	Measured transmission for the FZP and the 25%, 50%, and 75% apodized hybrid photon sieve with circular apertures.....	73
4-18	25% apodized hybrid photon sieve with circular apertures..	74
4-19	50% apodized hybrid photon sieve with circular apertures.....	75
4-20	75% apodized hybrid photon sieve with circular apertures.....	76
4-21	Measured FWHM of peak intensity. FWHM for the hybrid designs with circular apertures with 25%, 50%, and 75% of their area apodized.....	77
4-22	Measured peak intensities for the hybrid designs with circular apertures with 25%, 50%, and 75% of their area apodized.....	77
4-23	Maximally filled zone using circular apertures.....	78
4-24	Optimized transmitting area of the zone using segments of the zone as apertures.....	79
4-25	Magnified view of segmented apertures filling a zone.....	79
4-26	Defining the aspect ratio of an aperture.....	80
4-27	Calculated area distributions of hybrid photon sieve designs with segmented zone apertures.....	82
4-28	Measured transmission of Fresnel zone plate (FZP) and 25%, 50%, and 75% apodized photon sieve designs with segmented zone apertures with AR=1.....	82
4-29	25% apodized hybrid photon sieve incorporating segmented zone apertures with AR=1.....	83

4-30	50% apodized hybrid photon sieve incorporating segmented zone apertures with AR=1.	84
4-31	75% apodized hybrid photon sieve incorporating segmented zone apertures with AR=1.	85
4-32	Measured FWHM of peak intensity for hybrid designs with segmented zone apertures (SZA) with AR=1.	86
4-33	Measured peak intensity for hybrid designs with segmented zone apertures (SZA) with AR=1.	86
4-34	Calculated area distributions for hybrid 75% apodized photon sieves with segmented apertures of various aspect ratios (AR).....	88
4-35	Measured transmission for Fresnel zone plate (FZP), and 75% apodized hybrid photon sieves with segmented zone apertures of aspect ratio 4 (AR=4), 3 (AR=3) and 2 (AR=2).	89
4-36	75% apodized hybrid photon sieve incorporating segmented zone apertures with AR=2.	90
4-37	75% apodized hybrid photon sieve incorporating segmented zone apertures with AR=3.	91
4-38	75% apodized hybrid photon sieve incorporating segmented zone apertures with AR=4.	92
4-39	Measured FWHM of peak intensity for hybrid designs with large aspect ratio segmented zone apertures.....	93
4-40	Measured peak intensity for hybrid designs with large aspect ratio segmented zone apertures.....	93
4-41	Measured transmission for the 25% apodized designs.....	97
4-42	Measured transmission for the 50% apodized designs.....	98
4-43	Measured transmission for the 75% apodized designs.....	98

4-44	Intensity at focal point vs. total transmission for various lens designs	101
4-45	Measured FWHM of peak intensity for large aspect ratio segmented zone apertures.	102
4-46	Measured FWHM of peak intensity for 75% apodized designs.....	103
4-47	Measured FWHM of peak intensity for 50% apodized designs.....	103
4-48	Measured FWHM of peak intensity for 25% apodized designs.....	104
4-49	Resolution test of aperture pair with a 100 μ m separation for 75% hybrid apodized photon sieve with SZ apertures and aspect ratio of 4.	105
4-50	Resolution test of aperture pair with a 18 μ m separation for 75% hybrid apodized photon sieve with SZ apertures and aspect ratio of 4.	105
4-51	Resolution test of aperture pair with a 0.5 μ m separation for 75% hybrid apodized photon sieve with SZ apertures and aspect ratio of 4.	106

Abstract of Dissertation Presented to the Graduate School
of the University of Florida in Partial Fulfillment of the
Requirements for the Degree of Doctor of Philosophy

DESIGN AND FABRICATION OF DIFFRACTIVE LENSES FOR VISIBLE AND
NEAR INFRARED WAVELENGTHS

By

Narada Muni Bradman

August 2007

Chair: Paul H. Holloway

Major: Material Science and Engineering

A process to fabricate Fresnel zone plates and photon sieves has been developed and implemented. This three step process consisted of 1) depositing a thin metal film on a glass substrate, 2) using electron beam lithography to pattern a layer of polymethyl methacrylate (PMMA) that had been spin coated onto the surface of the sample, and 3) using dry etching, with the patterned PMMA acting as a mask, to transfer the pattern to the thin metal film. A variety of diffractive lens designs have been studied. These designs include a Fresnel zone plate (FZP), consisting of alternating transparent and opaque zones, both apodized and unapodized traditional photon sieves in which the transparent zones have been replaced with a distribution of discrete apertures, hybrid photon sieves which incorporate some of the completely open zones of the FZP for a portion of their open area while filling the remainder of the open area with discrete circular apertures,

and hybrid photon sieves photon sieves with segmented zone apertures which combine some of the open zones of the FZP with a distribution of discrete apertures whose shape mimics that of the underlying zone.

All of the diffractive lens design variations exhibited an increased intensity at the first order focus compared to the traditional photon sieve design, and the degree by which the intensity was increased corresponded directly to the extent to which the open or transmitting area of the lens was increased, e.g. the hybrid PS designs with segmented zone apertures exhibited higher transmissions and peak intensities compared to the traditional PS designs and the hybrid designs with circular apertures, with a measured peak intensity that were 41%, 35%, and 34% higher than the measured peak intensities of the 25%, 50%, and 75% apodized traditional photon sieve designs respectively. As a result the hybrid designs with large aspect ratio segmented zone apertures, which made the best use of the open zone area, exhibited the highest intensity at the focal point, e.g. the hybrid diffractive lens design which combined open Fresnel zones for its unapodized open area and segmented zone apertures with an aspect ratio of 4 for its apodized area, exhibited an 55% increase in intensity at the focal point relative to the traditional photon sieve design which filled the Fresnel zones exclusively with circular apertures. The full width half maximum of this design's intensity was also 6% smaller than that of the traditional photon sieve. The measured focal lengths of the photon sieves corresponded closely to the design focal lengths, varying no more than 1.3% from the design.

CHAPTER 1 INTRODUCTION

Refraction occurs when a wave traverses an interface between two media with different indices of refraction. For materials with a positive index of refraction, as the wave crosses the interface it bends towards the normal to the interface. Refractive optics¹ take advantage of this to bend light to a focal point. Diffraction can be described as a combination of two effects, namely scattering and interference, the combination of which results in a deviation in the behavior light from the predictions of geometric optics.¹ A wave incident on an obstruction or an aperture is scattered at the edges of the aperture or an obstruction. Diffractive optics²⁻⁴ employ many apertures or obstructions placed such that the scattered waves constructively interfere with each other at a focal point. Although refractive optics are more frequently used, there are a number of niche applications in which diffractive optics can compete with refractive optics.⁵⁻⁹

Refractive lens are most often formed using glass with a spherically curved surface. The thickness of the glass and radius of curvature are determined by the required focal length, the relative refractive indices of refraction of the glass and the medium surrounding the glass (usually air). Diffractive lens are usually formed by introducing a pattern of apertures in an opaque thin film. For some diffractive lens designs this thin film can be free standing. This can result in substantial reductions in both the weight and volume of the lens. As a result diffractive optics can offer significant advantages compared to their refractive counterparts in applications where the volume and weight of the focusing system are important design parameters.

This research consisted of designing, fabricating and testing a variety of diffractive lens designs including a Fresnel zone plate,¹⁰ several photon sieve¹¹ designs, and several hybrid zone plate/photon sieve designs, which incorporated elements of the photon sieve and the Fresnel zone plate.

Chapter 2 consists of background and a review of the literature on diffraction theory in general, focusing particularly the Fresnel zone plate and the photon sieve. The experimental processes developed to fabricate the Fresnel zone plates and photon sieves are outlined in Chapter 3. The various diffractive lens designs investigated and the results of testing the designs are discussed in Chapter 4. The conclusions reached in the course of this research are presented in Chapter 5 and interesting directions for future investigations are suggested in Chapter 6.

CHAPTER 2 LITERATURE REVIEW

2.1 Introduction

Optical elements that focus in transmission can be broadly classified based on the mechanism by which they focus. Refractive focusing elements bend light to a focal point by using a media of the appropriate shape and refractive index.¹ Diffractive focusing elements rely on scattering and constructive interference of the light to produce a focal point.¹⁰ Although the use of refractive focusing elements dominate in applications for focusing of light in the visible and IR wavelength ranges, there are some applications for which diffractive optical elements offer some significant advantages. Specifically, diffractive optics can offer significant advantages compared to their refractive counterparts in applications where the volume and weight of the focusing system are important design parameters.^{5,7}

First proposed by Kipp in 2001,¹¹ the photon sieve represented an evolutionary design step in an attempt to mitigate some of the shortcomings of a preexisting diffractive optical element, the Fresnel zone plate(FZP).¹⁰ The zone plate consists of alternating transparent and opaque zones of appropriate widths such that for a particular design wavelength a focal point results. However, secondary maxima of light blur the focus of a FZP. The photon sieve (PS) reduces the secondary maxima by altering the FZP design. In the PS the completely transparent zones of the FZP are replaced with a distribution of transparent apertures in the zone. The optical properties of the photon sieves can be

adjusted by appropriate manipulation of the distribution and density of the apertures populating the transparent zones. However, the PS transmits less light than the FZP.

This review of the literature will begin with a brief discourse on some of the different kinds of optical focusing elements, citing examples of refractive and diffractive systems. This is followed by a discussion of diffraction theory and its application to diffractive focusing elements. This review of the literature concludes with a justification of the proposed research and a discussion of how to improve the transmission and resolution of the FZP or the PS by adjusting the geometry and distribution of the apertures.

2.2 Optical Focusing Systems

Everyone is familiar with at least one kind of optical focusing element. The human eye is probably the most familiar example of an optical focusing system. Several separate elements of the human eye are responsible for refracting or bending incident light to a focal point. Refraction occurs when a wave traverses an interface between two media with different indices of refraction. The cornea and the lens of the eye are both composed of layers of cells with differing indices of refraction. The cornea has an index of refraction of ~ 1.40 ,¹² while the refractive index of the lens varies from 1.406 at the center to about 1.386 at the edges.¹³

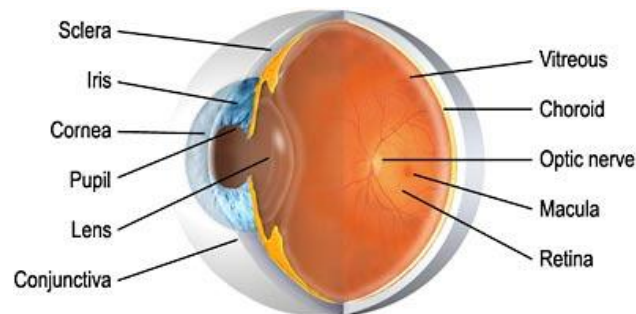


Figure 2-1. Components of a human eye¹⁴

As light crosses the interface between air and the eye at the surface of the cornea, its speed is reduced and it bends towards the normal to the interface. The degree to which the light bends can be described in accordance with Fermat's principle which states that "light takes the path of least time" and Snell's Law,¹ which relates the direction of propagation of light in terms of angles relative to the normal to the interface, to the indices of refraction of the media on either side of the interface.

$$\frac{n_1}{n_2} = \frac{\sin \theta_2}{\sin \theta_1} \quad 2-1$$

As illustrated below, n_1 and n_2 are the indices of refraction of the media on either side of the interface, and θ_1 and θ_2 are the angles relative to the interface normal along which light propagates in each of the medias, as shown in Figure 2-2.

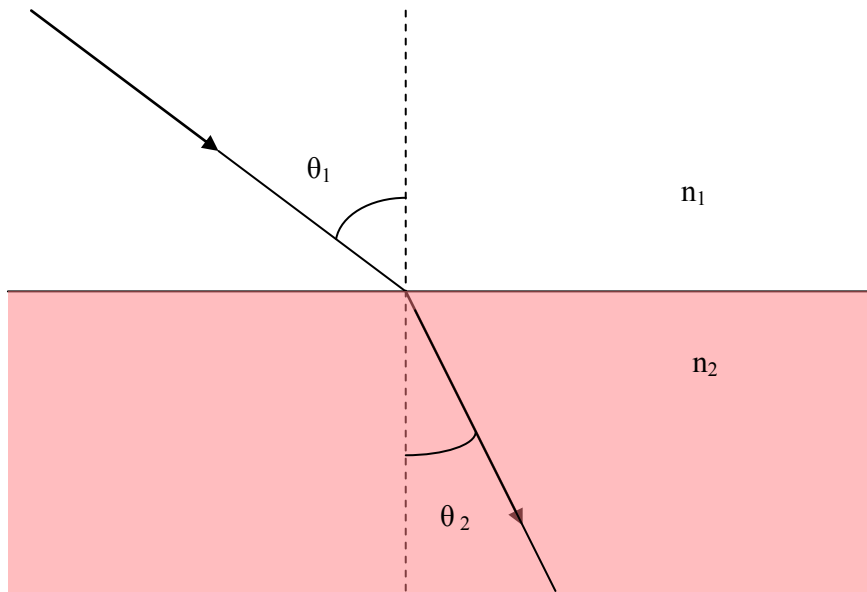


Figure 2-2. Snell's law of refraction. Shown is the direction of propagation of light at an interface between media with differing indices of refraction

There are a wide variety of materials with a range of indices of refraction and negligible absorption in the visible wavelength range.¹⁵ For this reason it is relatively easy to design a refractive lens to focus visible wavelength radiation. For shorter

wavelength radiation, such as extreme ultraviolet light or x-rays, most materials absorb a large fraction of the incident radiation. As such, an alternative means of focusing short wavelength radiation is necessary. For longer wavelengths, such as the infrared wavelengths, a similar problem is encountered. Appropriate materials, with an acceptably high transparency, are not as numerous. This is especially true when selecting refractive lens materials to focus the long wavelength infrared (LWIR-wavelengths 8-12 μm), for which there are significantly fewer suitable materials, and those materials' transparency is reduced by 8-10% compared to the selections for focusing visible wavelengths,¹⁵⁻¹⁸

In contrast to refraction discussed above, diffraction is the combinations of two effects, the scattering of waves as they propagate past small obstructions or through small openings and the subsequent constructive interference of the scattered waves. If a sufficiently large number of appropriately sized and located obstructions or openings are present, constructive interference of the scattered and/or transmitted waves can result in an increase in the amplitude of light wave at a particular location, i.e. result in a focal point. The Fresnel zone plate (FZP) is an example of a diffractive optical element. The zone plate consists of radially symmetric alternating transparent and opaque zones. An example of such a zone plate is depicted in Figure 2-3, where the dark circles represent transmitting zones and the light areas are opaque. Incident light scatters as it propagates past the opaque zones and constructive interference of the scattered light results in a focal point. Because the FZP can be designed using the appropriate materials to focus short wavelength radiation without suffering from the absorption problems that occur with the use of refractive lens, it is used extensively to focus x-rays and other short wavelength radiation.¹⁹

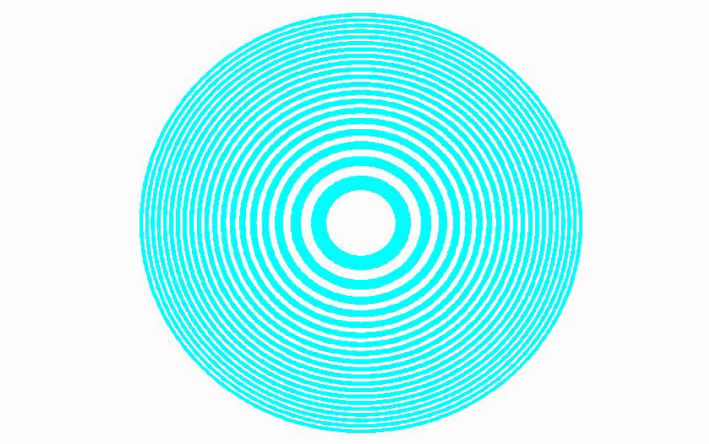


Figure 2-3. An example of a Fresnel Zone Plate. The dark areas are transmitting and the white areas are opaque. A 20 zone FZP lens is depicted.

However, when used to focus visible or NIR wavelength radiation, the zone plate suffers several considerable disadvantages compared to its refractive counterparts. Because roughly half of the area of a zone plate is opaque, a significantly smaller fraction of the incident radiation is transmitted to the focal point than when using a comparable refractive lens. Another problem encountered is the chromatic aberration of the FZP, or the focusing of different wavelengths at different focal lengths. Additionally, the focal plane intensity distribution of zone plates typically exhibit ring shaped secondary maxima which introduce a blur to the image and result in a reduced contrast.¹¹

2.3 Diffraction Theory

There are a number of formulations that can be used in diffraction theory to describe the propagation of an electromagnetic wave. These formulations can be broadly categorized in terms of their description of the wave, either as a vector or approximated as a scalar. It must be acknowledged that the formulations utilizing vector descriptions of the EM wave are more rigorous and generally applicable; however, in instances where the aperture is large compared to the wavelength of the EM wave, scalar approximations provide accurate representations of the behavior of the diffracted wave and are in good

agreement with the results provided by the more rigorous vector formulations. Some of the more established scalar approximations include Huygen's principle,¹⁰ the Rayleigh-Sommerfeld theory²⁰ and the Kirchoff formulation.^{10,20} The Fresnel approximation, which is reviewed below, is derived from the Kirchoff formulation and the Fraunhofer, approximation also reviewed below, is actually a special case of the more general Fresnel approximation.

2.3.1 Fresnel and Fraunhofer Diffraction Theory

It is useful to distinguish between two classifications when describing diffraction, Fraunhofer diffraction and Fresnel diffraction. In the instance when both the incident and diffracted wave are essentially planar in nature, the diffraction can be described as Fraunhofer diffraction. Physically, this occurs when the distances from the source of illumination to the aperture and from the aperture to the observation plane are large enough to neglect the curvature of the incident and diffracted waves. For this reason, Fraunhofer diffraction is also sometimes described as far field diffraction.¹⁰ Fresnel diffraction, sometimes described as near field diffraction,¹⁰ represents a more general description of diffraction and allows for the instance in which either the source or the plane of observation are sufficiently close to the diffracting object so that the propagating wavefront must be considered spherical. Consider both cases in which diffraction occurs from a single rectangular slit, illustrated below in Figure 2-4. The case illustrating Fraunhofer diffraction is depicted in Figure 2-4a, with the distances from the slit to the source and from the slit to the observation point, O, are sufficiently large such that the curvature of the propagating wave front can be neglected. The case illustrating Fresnel diffraction is shown in Figure 2-4 b, with the distance from the slit to the source and from

the slit to the observation point O small enough so that the curvature of the propagating wavefront must be taken into consideration.

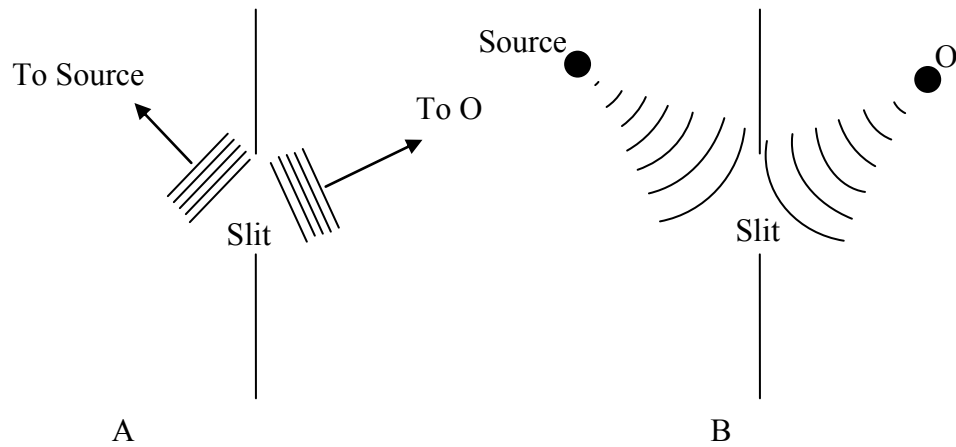


Figure 2-4. Diffraction from a slit. A) Fraunhofer diffraction from a single slit. B) Fresnel diffraction from a single slit

The distinction between Fresnel and Fraunhofer diffraction can be quantified by the following expression:

$$\frac{1}{2} \left(\frac{1}{d'} + \frac{1}{d} \right) \delta^2 \ll \lambda \quad 2-2$$

where δ is the characteristic size of the aperture (in the case of circular aperture this is the diameter, in the case of a rectangular aperture this is the shorter length), d' is the distance from the source to the aperture, d is the distance from the aperture to the point of observation and λ is the wavelength of the incident and diffracted light. If the criteria state by Equation 2-2 is satisfied, the conditions for Fraunhofer diffraction have been met. On the other hand if the criteria expressed in Equation 2-2 are not satisfied, the source or the point of observation are sufficiently close to the aperture such that the curvature of the wavefront must be taken into consideration, i.e. the diffraction should be analyzed as the more general Fresnel diffraction.

2.3.2 Fraunhofer Diffraction from a Single Rectangular Slit

Consider the instance in which the source of illumination and the observation plane are sufficiently far from the aperture such that the wave front arriving at and departing from the aperture may be considered planer. Additionally, the rectangular aperture is sufficiently large in one dimension relative to the other dimension that it may be considered a one dimensional slit. As the wavefront propagates past the slit, wavefronts from one region of the slit will constructively or destructively interfere with one another (i.e., will diffract) and the resulting distribution of intensity at the observation plane, as shown in Figure 2.5 will be observed as is described below.

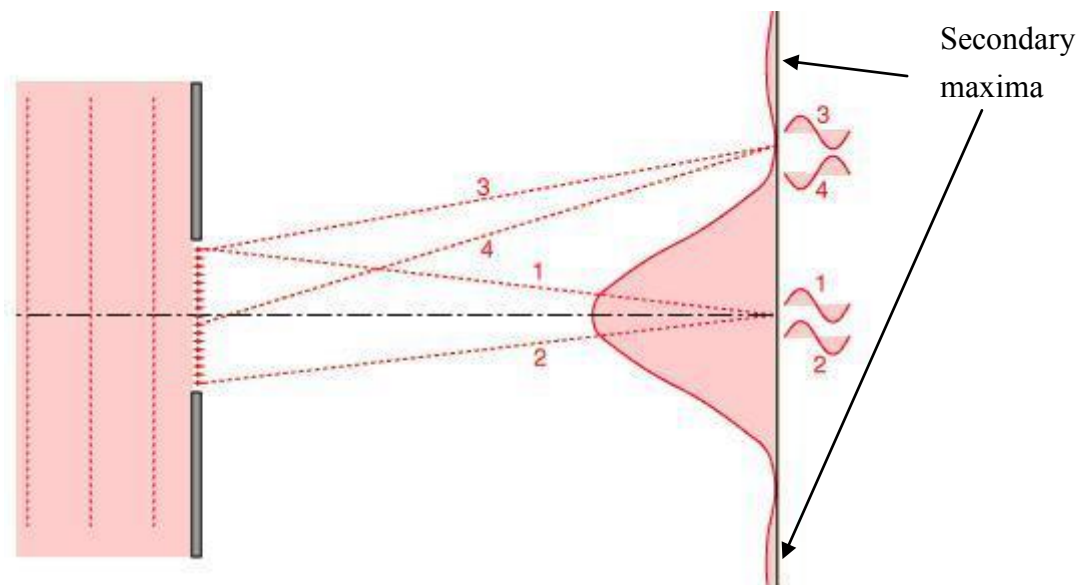


Figure 2-5. Fraunhofer diffraction through a single slit²¹

The wavefront incident on the slit can be considered as a collection of small elements, each of which act as a point source, known as Huygen's wavelets.¹⁰ Consider four of these point sources, labeled 1 through 4 in the Figure 2-5. Light traveling from point sources symmetric about the centerline, such as point source 1 and point source 2, travel a path such that the difference in the distance traveled is equal to one wavelength.

The light from the two point sources arrives at the centerline in phase and constructively interfere, resulting in an increased amplitude of the wave. Conversely, when light from point sources travel distances that differ by a half wavelength (paths 3 and 4), they arrive at a point out of phase, destructively interfere at that point and result in a very low amplitude of the wave. Light traveling from point source 3 and point source 4 result therefore in the first minima in the diffraction pattern. Although more of the point sources will constructively interfere at the centerline on the observation plane than at other locations, there are other locations on the observation plane where the difference in path length will be a full wavelength and constructive interference will result in secondary maxima. A quantitative description of the intensity distribution is provided in Equation 2-3.²²

$$I_{\theta} = I_0 \frac{\sin^2\left(\frac{\delta}{2}\right)}{\left(\frac{\delta}{2}\right)^2} \quad 2-3$$

where I_{θ} is the intensity at an angular distance θ from the axis, I_0 is the intensity of the zero order maximum, and δ is the phase displacement. The phase displacement δ , can be related to the deviation angle θ by Equation 2-4.

$$\delta = \frac{2\pi a \sin \theta}{\lambda} \quad 2-4$$

where a is the width of the long slit, and λ is the wavelength of light incident on the slit. Expressing the intensity distribution in terms of the deviation angle, as in Equation 2-5, yields the conditions for the locations of the minima in the diffraction pattern shown in Figure 2-5.

$$I = I_0 \frac{\sin^2\left(\frac{a\pi \sin \theta}{\lambda}\right)}{\left(\frac{a\pi \sin \theta}{\lambda}\right)^2} \quad 2-5$$

The intensity of the diffracted light will approach a minimum as the argument of the sine approaches integer multiples of π . This condition is expressed in Equation 2-6.

$$m\lambda = a \sin \theta \quad 2-6$$

where m is an integer. A graphical representation of Equation 2-6 is shown in Figure 2-6.

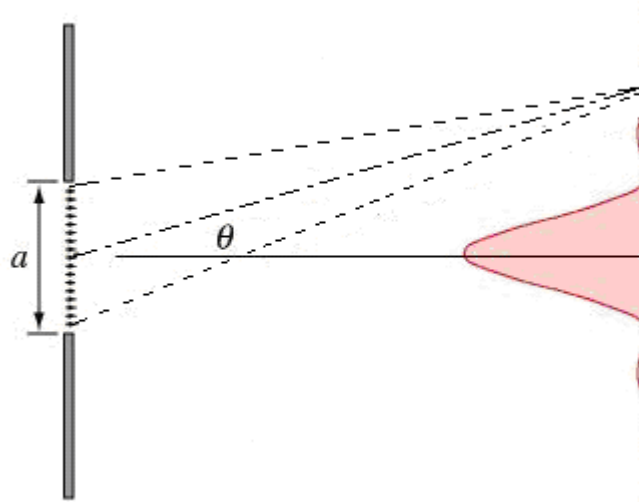


Figure 2-6. Location of minima in Fraunhofer diffraction from a single slit. ²²

Although the minima are spaced equally from the zero order maxima at the central axis, the maxima do not fall precisely between successive minima. Rather, they are displaced slightly towards the zero order maximum, with the first order maximum located at $\frac{a\pi \sin \theta}{\lambda} = 1.403\pi$, the second order maximum at $\frac{a\pi \sin \theta}{\lambda} = 2.4590\pi$, and higher orders more closely approaching the halfway point between minima. ¹

2.3.3 Fraunhofer Diffraction from Double Slits

The intensity distribution for the diffraction pattern of an aperture consisting of two parallel slits can be described by Equation 2-7²³

$$I_{\theta} = I_0 \frac{\sin^2\left(\frac{a\pi \sin \theta}{\lambda}\right)}{\left(\frac{a\pi \sin \theta}{\lambda}\right)^2} \cos^2\left(\frac{b\pi \sin \theta}{\lambda}\right) \quad 2-7$$

where b is the distance between the parallel slits. The distribution function for the single slit acts as an envelope for the interference fringes, whose distribution is described by the \cos^2 term. The resulting diffraction pattern is illustrated in Figure 2-7.

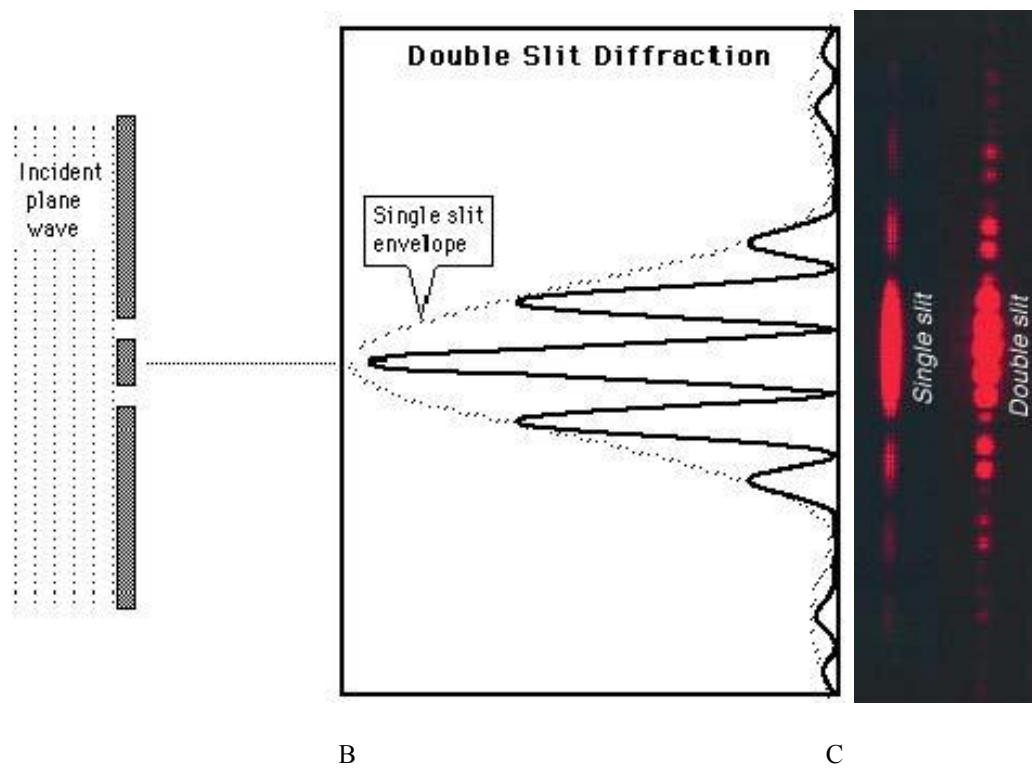


Figure 2-7. Fraunhofer diffraction through a double slit. A) A plane wave incident on a double slit aperture. B) The intensity distribution in the resulting Fraunhofer diffraction pattern. C) photographs of the diffraction pattern for a single and double slit.²⁴

2.3.4 Fraunhofer Diffraction from Rectangular and Circular Apertures

When both of the dimensions of the slit are comparable in size, diffraction from each of the edges becomes significant and warrant consideration. For a single rectangular aperture, with dimensions of a and b , the intensity distribution is give by Equation 2-8.²³

$$I = I_0 \left(\frac{\sin \alpha}{\alpha} \right)^2 \left(\frac{\sin \beta}{\beta} \right)^2 \quad 2-8$$

where $\alpha = \frac{a\pi \sin \phi}{2\lambda}$ and $\beta = \frac{b\pi \sin \theta}{2\lambda}$. The resulting diffraction pattern for a square

aperture (i.e. $a = b$), shown in Figure 2-8, has minima defined by $\alpha = \pm m\pi$,

and $\beta = \pm m\pi$, where m is a positive integer²³.

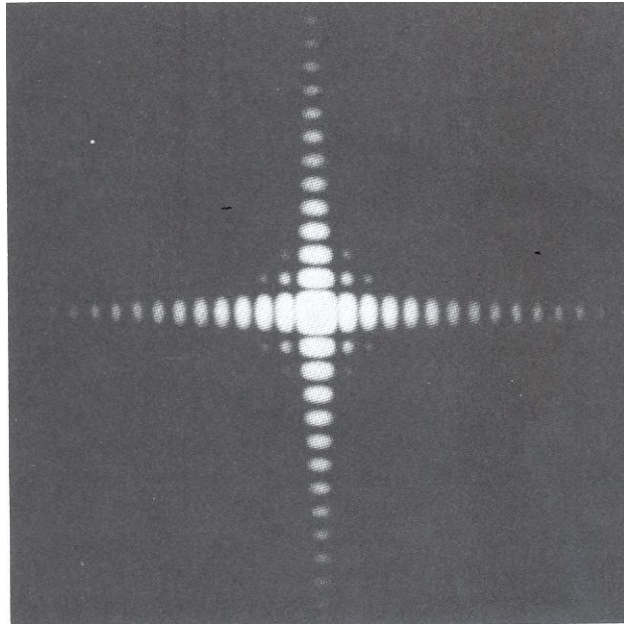


Figure 2-8. Diffraction pattern resulting from light incident on a square aperture.

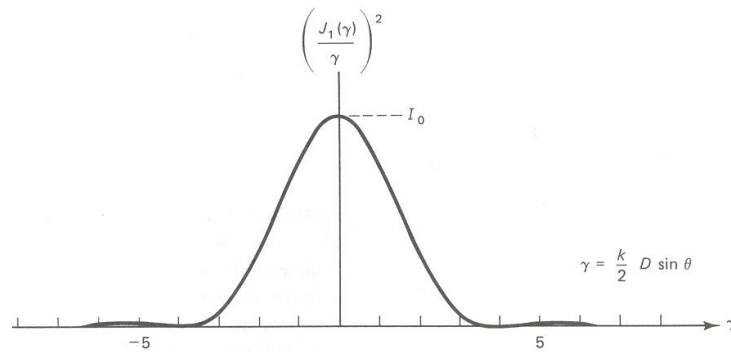
Using a single circular aperture results in a diffraction pattern known as the Airy disc¹⁰. The Airy disc pattern, shown in Figure 2-9, consist of a circular central maximum surrounded by successive rings of concentric maxima of decreasing intensity. The intensity distribution of the Airy disc pattern is described by Equation 2-9

$$I = I_0 \left[\frac{J_1(\gamma)}{\gamma} \right]^2 \quad 2-9$$

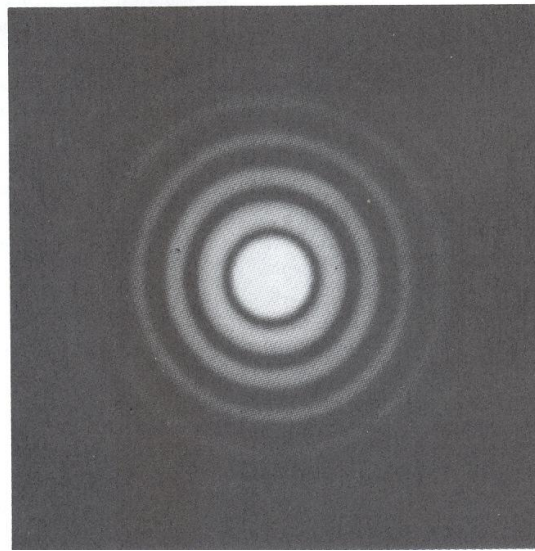
where I_0 is the intensity at the center of the diffraction pattern, i.e. at the zero order maximum, J_1 is the Bessel function of the first kind zero order, and γ is defined as

$$\gamma = \left(\frac{k}{2} \right) D \sin \theta \quad 2-10$$

where D is the diameter of the aperture, k is the wave vector magnitude ($2\pi/\lambda$) and θ is the angle measured from the normal of the aperture.



A



B

Figure 2-9. The Airy Disc. A) The irradiance pattern of a circular aperture B) diffraction pattern of a circular aperture, the central circle is known as the Airy disc.¹⁰

A plot of the Bessel function of the first kind zero order is shown in Figure 2-10, and it exhibits oscillatory behavior similar to that of a sine function. However as the argument of the function increases, the amplitude of the oscillations decrease.

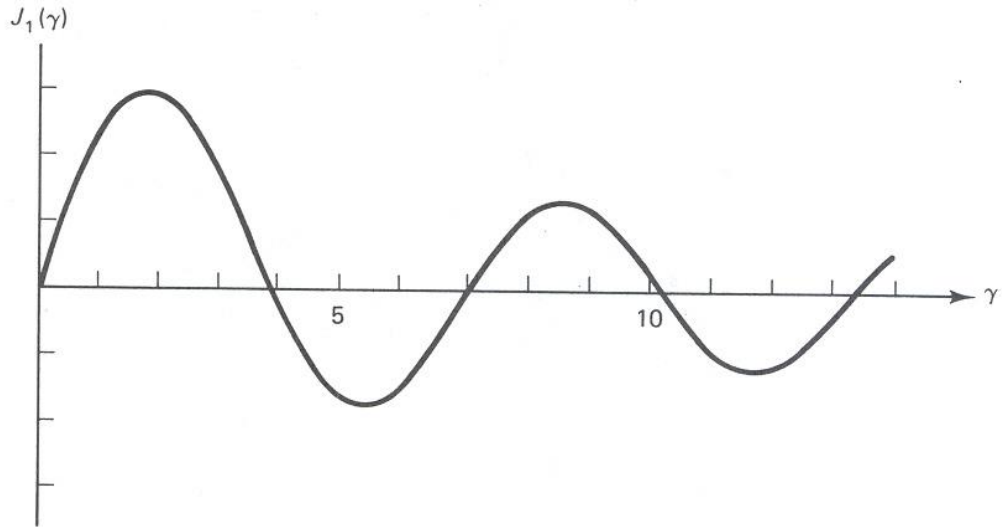


Figure 2-10. Bessel function of the first kind zero order. ¹⁰

Inspecting Figure 2-10 reveals that the Bessel function of the first kind zero order goes through zero for the first time when γ is 3.832. This corresponds to the first dark ring in the diffraction pattern, shown in Figure 2-9. The location of the first dark ring is determined by the wavelength of incident illumination and the diameter of the aperture, as described in Equation 2-11.

$$\gamma = 3.832 = \left(\frac{k}{2}\right) D \sin \theta \text{ or } D \sin \theta = 1.22\lambda \quad 2-11$$

2.3.5 Fresnel Diffraction

As mentioned previously, diffraction is described as Fresnel diffraction when either the light source or the plane of observation is sufficiently close to the diffracting aperture so that the incident light can no longer be considered planar. This is illustrated in Figure

2-4 b. For the case of a single slit, the intensity distribution of the diffraction pattern can be described by:

$$I = \frac{1}{2} \left(\frac{ab\lambda}{a+b} \right) \left[\left(\int \cos \frac{1}{2} \pi v^2 dv \right)^2 + \left(\int \sin \frac{1}{2} \pi v^2 dv \right)^2 \right] \quad 2-12$$

where a is the distance from the source to the slit, b is the distance from the slit to the observation plane, λ is the wavelength, and v is a substitutional variable related to the phase difference between rays from different wavefront elements and is defined as

$$v = h \sqrt{\frac{2(a+b)}{ab\lambda}} \quad 2-13$$

The integrals in Equation 2-11 are known as the Fresnel integrals. The intensity distribution is often written as

$$I = \frac{1}{2} \left(\frac{ab\lambda}{a+b} \right) [x^2 + y^2] \quad 2-14$$

where x and y are the Fresnel integrals defined as

$$x = \int \cos \frac{1}{2} \pi v^2 dv \quad 2-15$$

$$y = \int \sin \frac{1}{2} \pi v^2 dv \quad 2-16$$

If the Fresnel integrals are solved between a lower limit of $v_1 = 0$ and an upper limit of $v_2 = \infty$, and then plotted versus each other, a curve known as Cornu's spiral results. This spiral, shown in Figure 2-11, can be used to determine a graphical solution to diffraction problems. The amplitude due to a particular wavefront element corresponds to an element of length along the curve; however the total amplitude corresponds to the

shortest distance between the ends points of this element of length, or the chord. The square of this chord is the intensity.

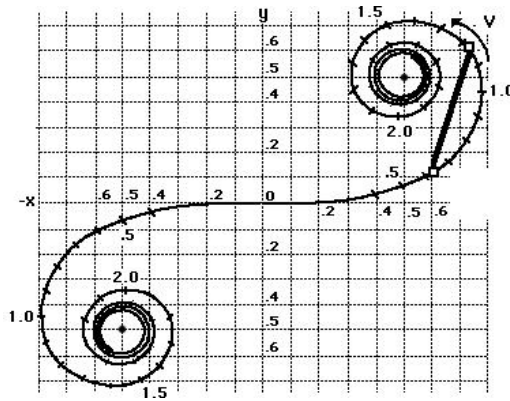


Figure 2-11. Cornu's Spiral. The x and y coordinates are the results of evaluating the Fresnel integrals shown in Equation 2-15 and 2-16 for Fresnel diffraction conditions.¹

2.3.6 Fresnel Zone Plates

Consider the case of Fresnel diffraction through a circular aperture. For simplicity assume that the source of the light is at an infinite distance from the aperture and as such the wavefronts are planar as they arrive at the aperture. This is depicted in Figure 2-12.

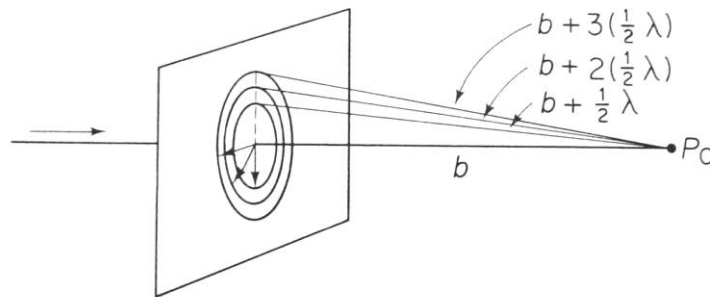


Figure 2-12. An aperture illuminated by a source at infinity. It is divided into zones spaced such that their boundaries lay a half of a period from each other.¹

The aperture can be divided into zones, such that the boundary of each of the zone is $\frac{1}{2}\lambda$ further from the point P_o . Applying Pythagoras' theorem yields the radius at the boundaries of the zone as

$$R_m = \sqrt{\left(b + \frac{1}{2}m\lambda\right)^2 - b^2} \quad 2-17$$

where R_m is the radius to the boundary of the zone, m is the number of the boundary under consideration, λ is the wavelength of the incident illumination, and b is the distance along the optic axis from the FZP to the point P_o , as defined in Figure 2-12. Additionally, careful inspection will reveal that the area of each of the zone is essentially equal to one another, and therefore the contributions for each zone is approximately equal. However, since the distance from each zone differs by a half of a wavelength, the contribution from each zone destructively interferes at point P_o and the resultant is zero intensity. Blocking the odd numbered zones results in the contributions from the remaining zone arriving at point P_o in phase so that they constructively interfere; P_o becomes the focus of a zone plate. The focal length of the zone plate can be derived and is given by

$$f = b \approx \frac{R_m^2}{m\lambda} \quad 2-18$$

where m is the number of zones in the zone plate. It can be seen by Equation 2-18 that the focal length depends on the inverse of the wavelength. As a result different wavelengths will focus at different distances from the lens, a defect referred to as longitudinal chromatic aberration. The spatial resolution of a lens is defined as the minimum separation between two objects at which the objects can still be resolved and is often defined in terms of the Rayleigh criterion. The Rayleigh criterion describes the minimum distance between two point sources at which they can still be resolved and states that this minimum distance is defined by the point at which the central maximum in the Airy disc of one of the apertures begins to overlap the first minimum of the Airy disc of the other aperture. This is shown in Figure 2-13. The spatial resolution of the zone plate depends

on the width of the outermost zone.

For the instance in which the incident illumination is incoherent and the apertures is circular, the Rayleigh criterion is met when there is a 26.5% reduction in intensity between the two maxima.²⁰

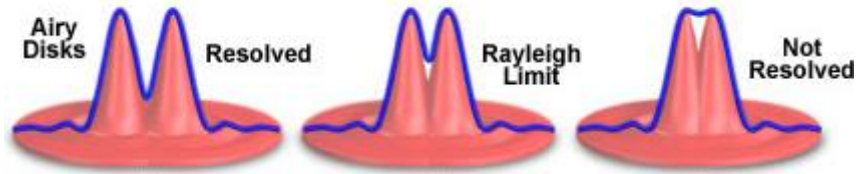


Figure 2-13. The Rayleigh criterion. Shown are the focal plane intensity distributions from a pair of point sources in which the Airy discs are well resolved, barely resolved at the Rayleigh limit and not resolved.²⁵

The spatial resolution of the FZP can be derived¹³ and is given by

$$\delta m = \frac{1.22\Delta r_n}{m} \quad 2-19$$

where δm is the spatial resolution, Δr_n is the width of the outer most zone, and m is the diffraction order. It is evident that the resolution of the FZP is limited by the width of the outermost zone, which is in turn limited by the lithography and fabrication techniques used in its fabrication. The photon sieve offers a means of reducing fabrication complexity and circumventing the resolution limit imposed by available methods of fabrication.

2.3.7 Photon Sieves

The photon sieve, first proposed by Kipp in 2001,¹¹ has been subsequently modeled theoretically by Cao²⁶⁻³⁰ and Lin³¹ and experimentally tested by Menon³² and Anderson.³³ A photon sieve consist of a large number of apertures or pinholes, placed such that they satisfy the requirements for constructive interference at a desired focal point, i.e. they are distributed such that they are centered in Fresnel zones and as such the

distance that light travels from the source to the focal point via the center of a pinhole must be an integral number of wavelengths. This requirement is stated in Equation 2-20 and illustrated in Figure 2-14.

$$\sqrt{r_n^2 + p^2} + \sqrt{r_n^2 + q^2} = p + q + n\lambda \quad 2-20$$

where r_n is the distance between the center of the pinhole and the optical axis, p is distance between the plane that contains the source and plane that the photon sieve lies in, and q is the distance between the plane containing the photon sieve and the focal plane.

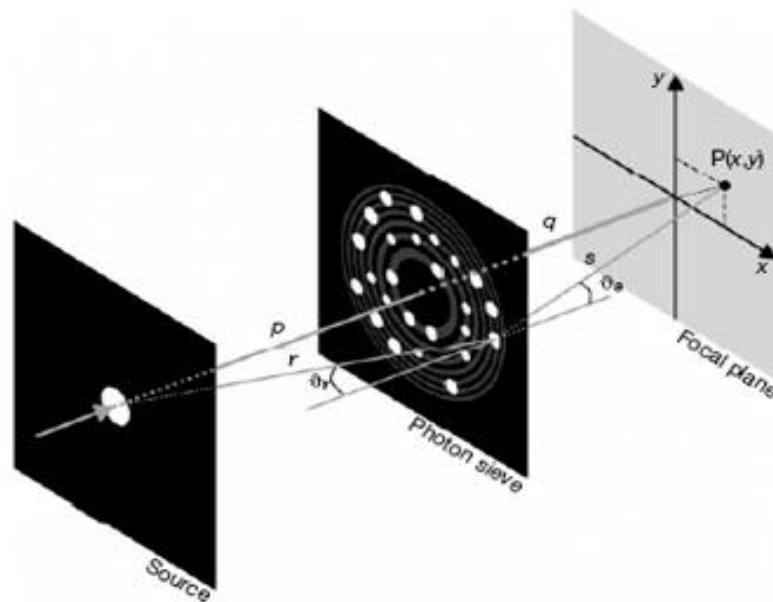


Figure 2-14. The photon sieve. Representation of source, photon sieve and focal planes and relevant distances.¹¹

It is not immediately apparent what advantage there is to be achieved by simply exchanging the completely transparent zones of a Fresnel zone plate with the partially occluded zones of a photon sieve. In fact, as the zones of the FZP alternate between completely transparent and completely opaque, the reduction in transmitting area translates directly into decreased intensity at the focal point. However, using pinholes distributed over the Fresnel zone is advantageous for several reasons. Kipp¹¹ showed that

the pinholes could have diameters larger than the underlying Fresnel zone, which results in easier fabrication and improved resolution. They also showed that distributing pinholes on the Fresnel zones affords the opportunity to employ apodization as a means of smoothing the transmission window and thereby reducing the secondary maxima. As discussed above, the area of each zone in a Fresnel zone plate is essentially equal to one another and each of the zones contributes equally to the amplitude of the intensity at the zero order focus. However, at the outer extremity of the FZP, the contribution plummets from some finite value to zero. Another way of saying this is to say that the function that describes the transmission, called the transmission window, has a discontinuous step. This discontinuity in the transmission window results in intensity oscillations (secondary maxima) in the diffraction pattern.¹¹

Apodization refers to the modification of the transmission window in order to redistribute the energy in the diffraction pattern, usually in order to reduce the intensity of secondary maxima.²³ This modification is implemented by applying some continuous function, an apodization function, to smooth the discontinuity of the transmission window. In the instance of the photon sieve, modifying the transmission function is achieved by varying the density of the pinholes in the Fresnel zones such that each successive zone contains fewer pinholes. This allows the transmission function to vary smoothly to zero, rather than with the discontinuity as in the step function of the zone plates' transmission window. Apodization is widely used in a variety of fields including astronomy^{6,34-36}, microscopy³⁷⁻³⁹, and Raman spectroscopy^{40,41}. Some of the more commonly used window functions applied in apodization are plotted (Figure 2-14), showing how they vary continuously to zero. The equations that define these functions

are shown in Table 2-1. The Cosine window was used as apodization function in this research.

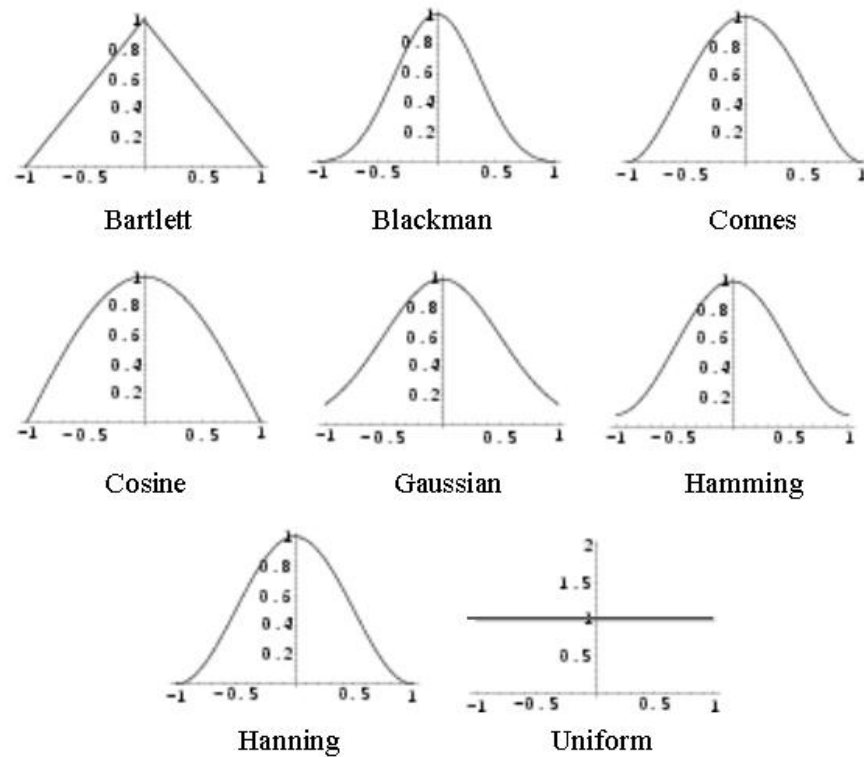


Figure 2-15. Commonly used apodization functions. The functions are plotted showing how each varies from its peak value to its minimum⁴².

Table 2-1. Equations defining apodization functions⁴².

Type	Function
Bartlett	$1 - \frac{ x }{L}$
Blackman	$0.42 + 0.5 \cos\left(\frac{\pi x}{L}\right) + 0.08 \cos\left(\frac{2\pi x}{L}\right)$
Connes	$\left(1 - \frac{x^2}{L^2}\right)^2$
Cosine	$\cos\left(\frac{\pi x}{2L}\right)$
Gaussian	$e^{-x^2/(2\sigma^2)}$
Hamming	$0.54 + 0.46 \cos\left(\frac{\pi x}{L}\right)$
Hanning	$\cos^2\left(\frac{\pi x}{2L}\right)$
Uniform	1

Kipp demonstrated that apodization of a photon sieve could effectively suppress secondary maxima, as compared to the unapodized zone plate with a rectangular transmission window.¹¹ Shown in Figure 2-16 are both the experimentally measured intensity distribution at the focal plane and the calculated intensity distribution at the focal plane, for transmissions through an apodized photon sieve and an unapodized Fresnel zone plate.

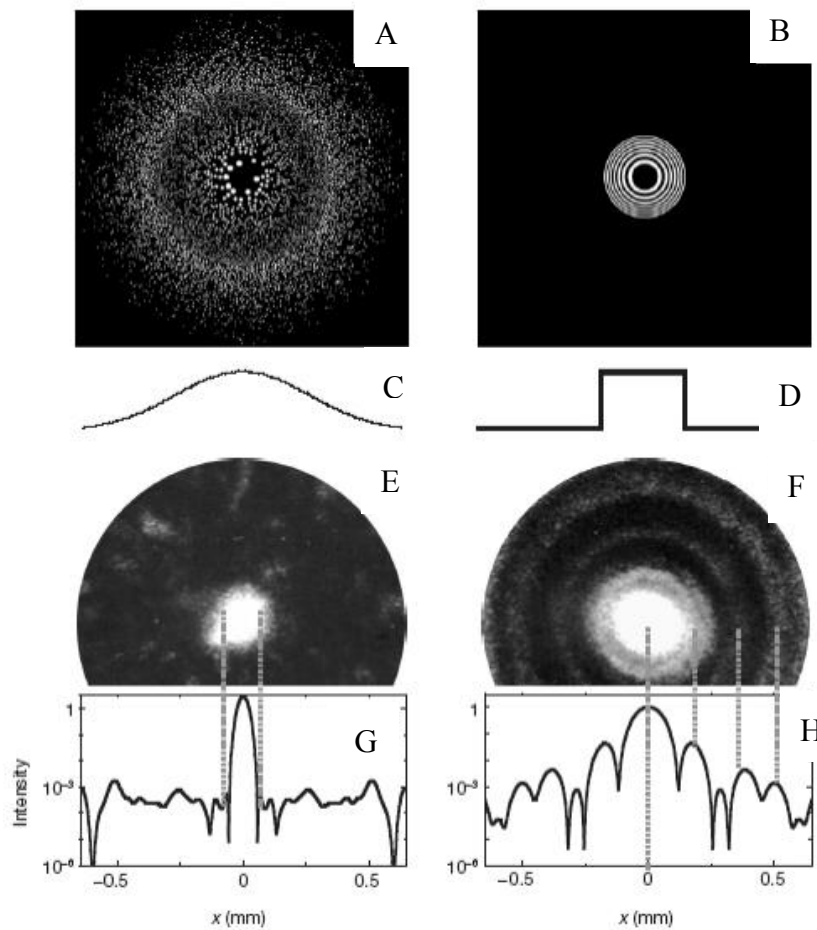


Figure 2-16. Intensity distributions for an apodized photon sieve and a Fresnel zone plate. A) Intensity distribution for photon sieve. B) Intensity distribution for a Fresnel zone plate. C) Weber type transmission window. D) Non-apodized rectangular transmission window. E) Photographed intensity at focal plane for photon sieve. F) Photographed intensity at focal plane for FZP. G) Calculated intensity distribution for a photon sieve. H) Calculated intensity distribution for a FZP.

Inspection of the intensity distributions reveals that the apodized photon sieve achieves a significant suppression of the secondary maxima (by at least 2 orders of magnitude) because of its smoother transmission window. Kipp showed that as the diameter of the pinhole was increased the net contribution from that pinhole at the focal point varied and went through a maximum before again decreasing. This variation in the net contribution that results when varying the pinhole size is shown in Figure 2-17.

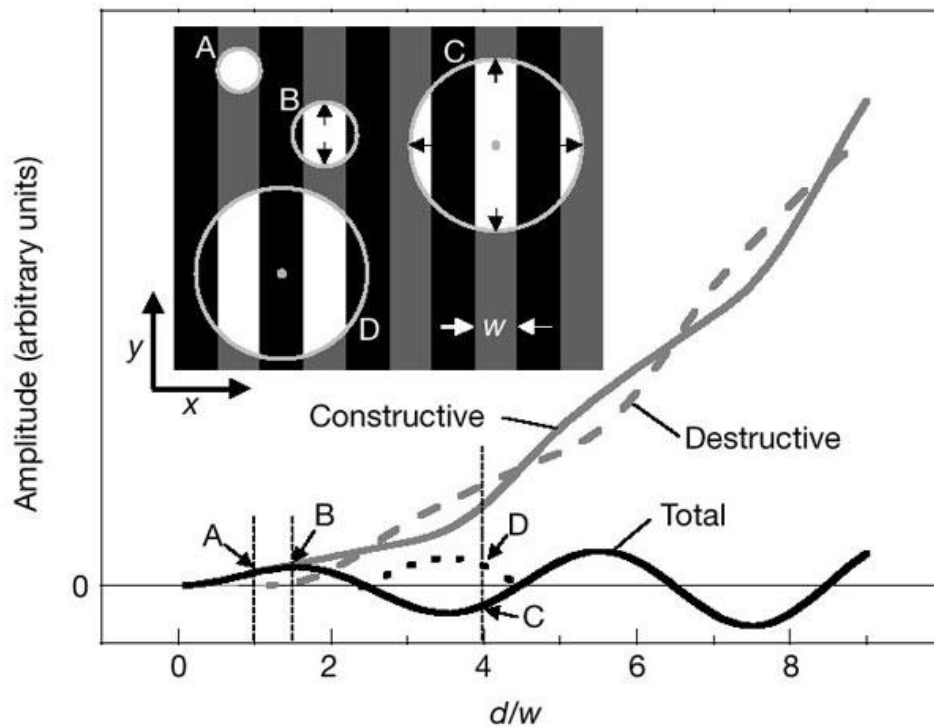


Figure 2-17. Amplitude of contribution from enlarged apertures. Shown are apertures of increasing diameter placed on underlying transparent Fresnel zones (represented by the light gray) and their constructive and destructive contributions at the focal plane. The amplitude of the contribution is plotted versus the pinhole diameter to zone width ratio.¹¹

The increase in the net constructive contribution at the focal point as the d/w ratio was increased as in from point A to point B in Figure 2-17, was verified experimentally by Menon.³²

2.4 Applications of Diffractive Lens

Diffractive lenses such as FZP or PS are generally fabricated by patterning a thin metal film or a metal foil. Because they can be constructed to avoid the absorption issues that arise when using refractive optics, zone plates have been used extensively to focus x-rays for microscopy.^{43,44} Kipp pioneered the use of photo sieves for x-ray microscopy in 2001.¹¹ Zone plates and photon sieves have also been used to focus x-rays and extreme ultraviolet (EUV) radiation for maskless lithography.^{8,19,45-50} Smith⁵¹ first proposed using an array of zone plates coupled with MEMS shutters to lithographically expose patterns without the use of a mask. Gil^{8,48} and Menon³² have modeled using photon sieves in similar arrays to carry out maskless lithography. Although diffractive optics have been primarily used to focus short wavelength radiation they are also well suited in applications where volume and weight are important design considerations. Examples of such applications include micro unmanned aerial vehicles⁵, and space-based telescopes.^{6,7,9,35,52} Anderson⁶ proposed a photon sieve based telescope and Artzner³⁵ proposed using photon sieves in the EUV telescope of the Solar Orbiter.

2.5 Impetus for Research

Although large body of work has been devoted to Fresnel zone plates, the majority of this work has been focused on zone plates designed for short wavelength radiation (i.e. X-ray and EUV wavelengths). There has been little research concerning the use of zone plates or photon sieves at longer wavelengths (visible and near infrared). It is of interest to investigate whether the photon sieves designed for long wavelengths can be optimized to improve their transmission characteristics and resolution. Several approaches can be incorporated simultaneously to achieve this goal. The shape of the pinhole apertures used in the photon sieve can be adjusted to more closely conform to the zone shape. This

would more efficiently use the available transmitting area and yield an increase in intensity at the focal point. Some of the zones of the photon sieves can be left completely open rather than populating them with discrete apertures. This can be done without altering the shape of the transmission window and should therefore increase the transmission without contributing to the secondary maxima,

CHAPTER 3 EXPERIMENTAL PROCEDURE

3.1 Introduction

In this chapter the process developed to fabricate photon sieves and Fresnel zone plates will be described. A variety of fabrication processes were explored and subsequently discarded in the course of developing of the following process. Alternative processes included a reversed image etching process, a lift-off process, a direct wet etching process, and the current direct dry etching process with several different resist schemes. The details of these processes are excluded for the sake of brevity but can be referred to in the dissertation of Hsiu Hsin Chung.⁵³ The process used for fabrication in this research was a direct dry etching process using PMMA both as an electron beam resist and a mask material in the dry etching pattern transfer step. There is some precedent in the use of PMMA both as a high resolution electron beam resist⁵⁴⁻⁵⁹ and as a mask material for pattern transfer.^{60,61}

3.2 Photon Sieve Fabrication

The direct dry etching process used in the fabrication of photon sieves can be described in terms of three major steps, namely: substrate preparation, patterning, and pattern transfer via etching. An overview of the entire process is shown in Figure 3-1 with a detailed description of each of the processing steps in subsequent sections.

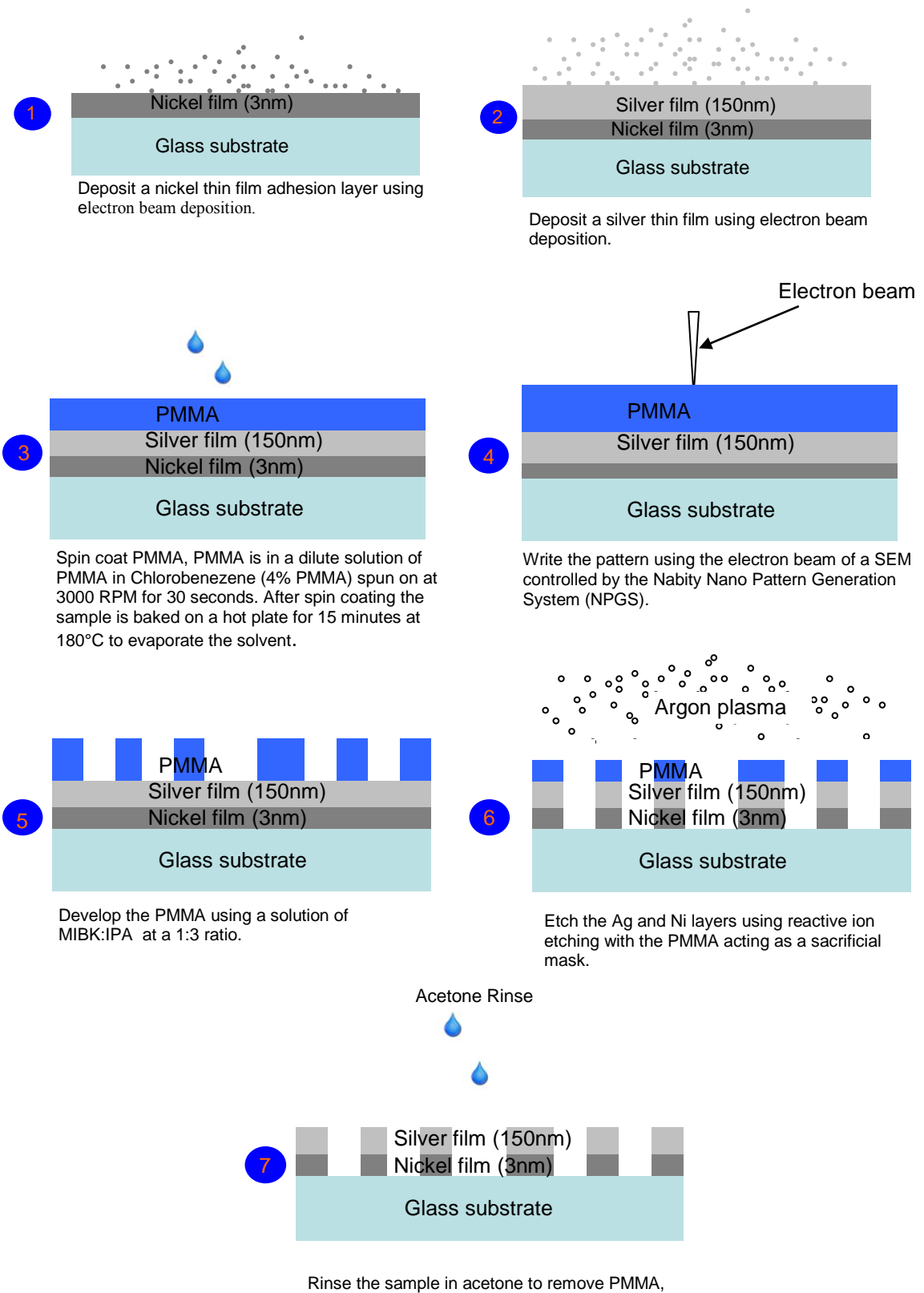


Figure 3-1. Overview of the diffractive lens fabrication process.

3.2.1 Substrate Preparation

Substrate preparation consist of partitioning and cleaning the glass substrates, depositing thin metal films via electron beam deposition, and applying a layer of electron beam resist.

3.2.1.1 Substrate clean

Fisher Scientific 12-549 microscope slides⁶² were used as substrates. The 1 inch by 3 inch by 1mm thick slides were scored using a diamond scribe and fractured into 1 inch by 1 inch pieces. These pieces were hand scrubbed using a brush in a solution of Alconox detergent in DI water. The substrates were rinsed with DI water remove any Alconox residue and then further cleaned by sequentially submersion in a three tier cascading DI water bath with nitrogen bubblers to remove any particulate matter remaining on the surface. Substrates were submerged in the first tier for 5 minutes, in the second tier for 5 minutes and in the third tier for 10 minutes. Subsequently, they were dried using a stream of dry nitrogen.

3.2.1.2 Thin film deposition

The metal thin films were deposited using an electron beam evaporation system.⁶³ The critical elements of the system are illustrated in Figure 3-2. The dry mechanical pump, a Leybold Dryvac 100P scroll pump,⁶⁴ evacuates the chamber to low vacuum in the range of 100-150 millitorr. The cryogenic pump,⁶⁴ a CTI Cryogenics Cryo Torr 8, evacuates the chamber to high vacuum, in the range of 10^{-6} Torr. A thermocouple gauge in the roughing line was used to measure the pressure at low vacuum (1-1000 milliTorr) and an ionization gauge is used to measure chamber pressure at high vacuum ($<10^{-3}$ Torr). An INFICON crystal monitor⁶⁵ and INFICON XTC/2⁶⁶ deposition controller

allowed real time monitoring of the deposition rate and semi-automatic control of the thickness of the deposition.. The water cooled hearth, which held up to five crucibles, could be rotated to allow any one of the crucibles to serve as a deposition source.

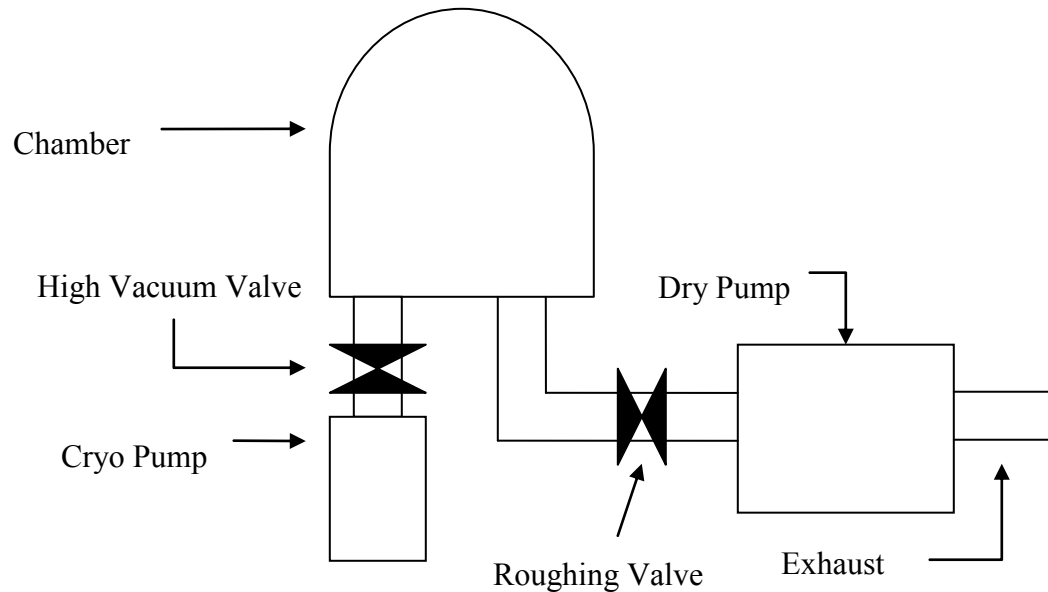


Figure 3-2. Electron beam evaporator system. This system was used to metallize the glass substrates

In a standard deposition, two of the 1 inch by 1 inch substrates were mounted above the hearth containing the crucibles. Care was taken to mount the substrates as close as possible in direct line of sight of the crucible in order to minimize variations in thickness of the deposited metal across the substrate area. The source to substrate distance was approximately 15 cm. The INFICON deposition controller was inputted with the density (8.910g/cm^3) and the Z ratio (0.311) of nickel, and with the total deposition thickness of 30\AA .

The chamber was first evacuated using the dry rough pump. While the chamber was being evacuated the substrates were heated by two 100 watt halogen bulbs to aid in the removal of any residual adsorbed moisture. When the readout of the thermocouple

gauge indicated a pressure of ~ 150 mTorr, the roughing valve was closed and the dry pump was turned off. The high vacuum valve, between the cryo pump and the chamber was opened and the chamber further evacuated until the ionization gauge indicated a pressure of $\sim 3 \times 10^{-6}$ Torr. Once the chamber had been evacuated, the power to the electron source filament was turned on and the current was slowly increased to raise the temperature to that necessary for thermionic emission. With a shutter between the source and substrates, the current to the filament was manually adjusted until the deposition rate stabilized at one angstrom per second. Once the deposition rate had stabilized, the shutter was manually opened and the substrates were exposed to the evaporating nickel. The INFICON deposition controller automatically rotated the shutter to shield the substrates from the evaporating nickel when 30 angstroms of nickel had been deposited. Once the shutter was closed, the current to the filament was turned off and the hearth was rotated to allow heating of the crucible containing silver. The INFICON deposition controller was inputted with the density (10.50g/cm^3) and Z ratio (0.529) of silver, as well as the total deposition thickness of 1500 \AA . Current to the electron source filament was again increased with the shutter closed until the crystal monitor indicated that the deposition rate had stabilized at 20 angstroms per second. The shutter was opened and silver was deposited until the crystal monitor controller closed the shutter at a thickness of 1500 \AA . The substrate was allowed to cool for 15 minutes before closing the high vacuum valve and back filling the chamber with dry nitrogen up to atmospheric pressure.

3.2.1.3 Application of resist

Polymethyl methacrylate (PMMA) was used as high resolution positive tone electron beam resist. PMMA is used extensively as an electron beam resist because of its

low cost and ease of processing. PMMA thin films readily adhere to a most substrate materials without the application of an adhesion promoter. Additionally they are insensitive to white light and stable in air. PMMA is a positive tone resist in which chain scission occurs in areas exposed to an electron beam or ultraviolet radiation. The PMMA in these areas is more susceptible to dissolution in a developer solution than areas that have not been exposed. The PMMA used was obtained from Microchem and was provided as a solution of 4% 950 MW PMMA in chlorobenzene.⁶⁷ The PMMA solution was applied to the sample using a programmable spin coater (Specialty Coating Systems Inc. Model P6708). Three parameters were programmed when using the spin coater: ramp up times, revolutions per minute, and hold times. The following is an example of a set of parameters used to program the spin coater.

Table 3-1. Spin coater parameters

Parameter	Value	Units
RPM1	300	Revolutions per minute
Ramp1	0	Seconds
Time1	15	Seconds
RPM2	3000	Revolutions per minute
Ramp2	5	Seconds
Time2	30	Seconds
RPM3	0	Revolutions per minute
Ramp3	5	Seconds

The spin coater would begin spinning at 300 revolutions per minute, and hold this rate of rotation for 15 seconds. After the 15 seconds had transpired, the spin coater would ramp the rotation rate from 300 rpms up to 3000 rpms over a period of 5 seconds and hold this rate of rotation for 30 seconds. After 30 seconds had transpired, the spin coater would decelerate to zero rpms over a period of 5 seconds. After the spin coater had been

programmed, the sample was placed on the vacuum chuck. The program described above was run twice; once as a clean run where the sample was rinsed with isopropyl alcohol and methanol, and again with the first 15 second hold in the program being used to dispense $\sim 200 \mu\text{L}$ of 4% PMMA in chlorobenzene on the sample. A spin speed versus thickness chart, obtained from the specification sheet for the PMMA from MicroChem is shown in Figure 3-3. The spin curve for the 4%PMMA in chlorobenzene shows that a spin speed of 3000 rpm would result in a PMMA layer thickness of approximately 500nm.

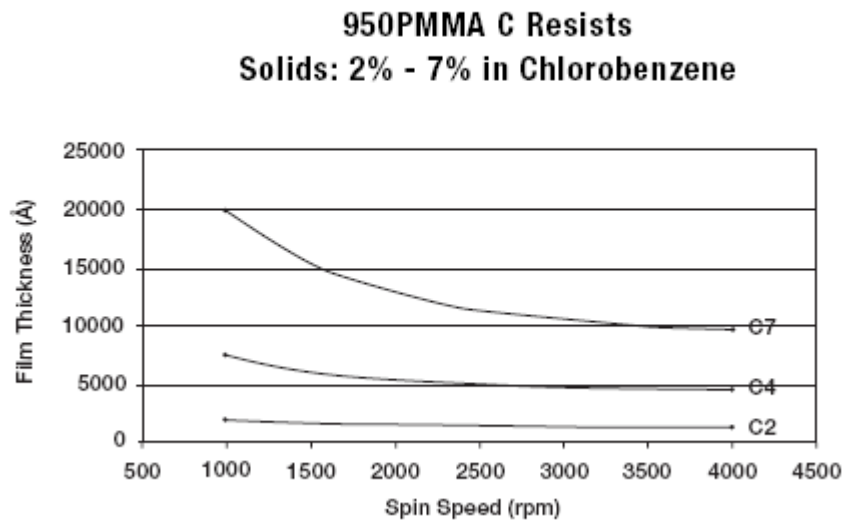


Figure 3-2. PMMA thin film thickness as a function of spin speed as specified by the manufacturer.⁶⁷

After the spin coater had been used to apply a thin film of PMMA to the sample, the sample was soft baked on a hot plate at 180°C for 15 minutes to drive off any remaining solvent. A Cole Parmer Data Plate 720 Series Digital Hot Plate was used to bake the sample under a fume hood.

3.2.2 Lithographic Patterning

Patterning of the resist can be described in terms of three steps; pattern generation using a CAD program, electron beam lithography using a standard scanning electron microscope controlled by a commercial electron beam lithography system and subsequent pattern development.

3.2.2.1 Pattern generation

Photon sieve and Fresnel zone plate patterns are generated with DesignCad LT 2000, a computer aided design software package produced by Upperspace Corporation. DesignCad supports the use of user written macros which facilitates the generation of relatively complex patterns. Examples of macros written to generate patterns are in Appendix A. A DesignCad representation of a Fresnel zone plate (FZP) pattern to be generated by electron exposure of the PMMA resist is shown in Figure 3-3.

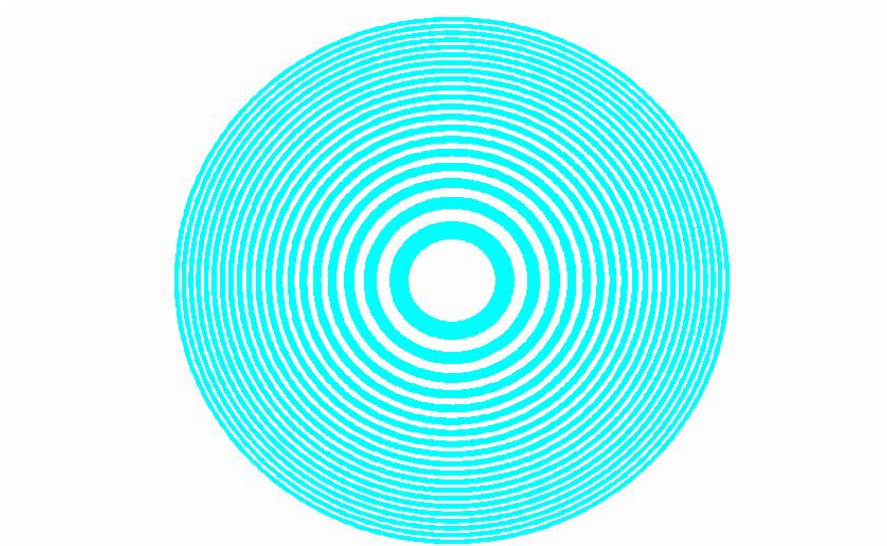


Figure 3-3. DesignCad pattern of the Fresnel zone plate

3.2.2.2 Electron beam lithography

The patterns were loaded into the Nano Pattern Generation System (NPGS),⁶⁸ a scanning electron microscope lithography software package produced by JC Nability

Lithography Systems. The NPGS software allows control over a wide array of variables which are specified in a run file. A screen capture of the run file is displayed below.

Among the important parameters specified in each run file were the patterns to be written, stage movements that were required prior to or after writing each pattern, and the dose ($\mu\text{C}/\text{cm}^2$) to be used when writing the pattern. Multiple lenses were written on a single 1" x 1" substrate, therefore the stage movements between writing each pattern had to be designed to ensure that individual patterns did not overlap with each other. The NPGS software would use the beam current and dose specified by the user to calculate the dwell time of the electron beam.

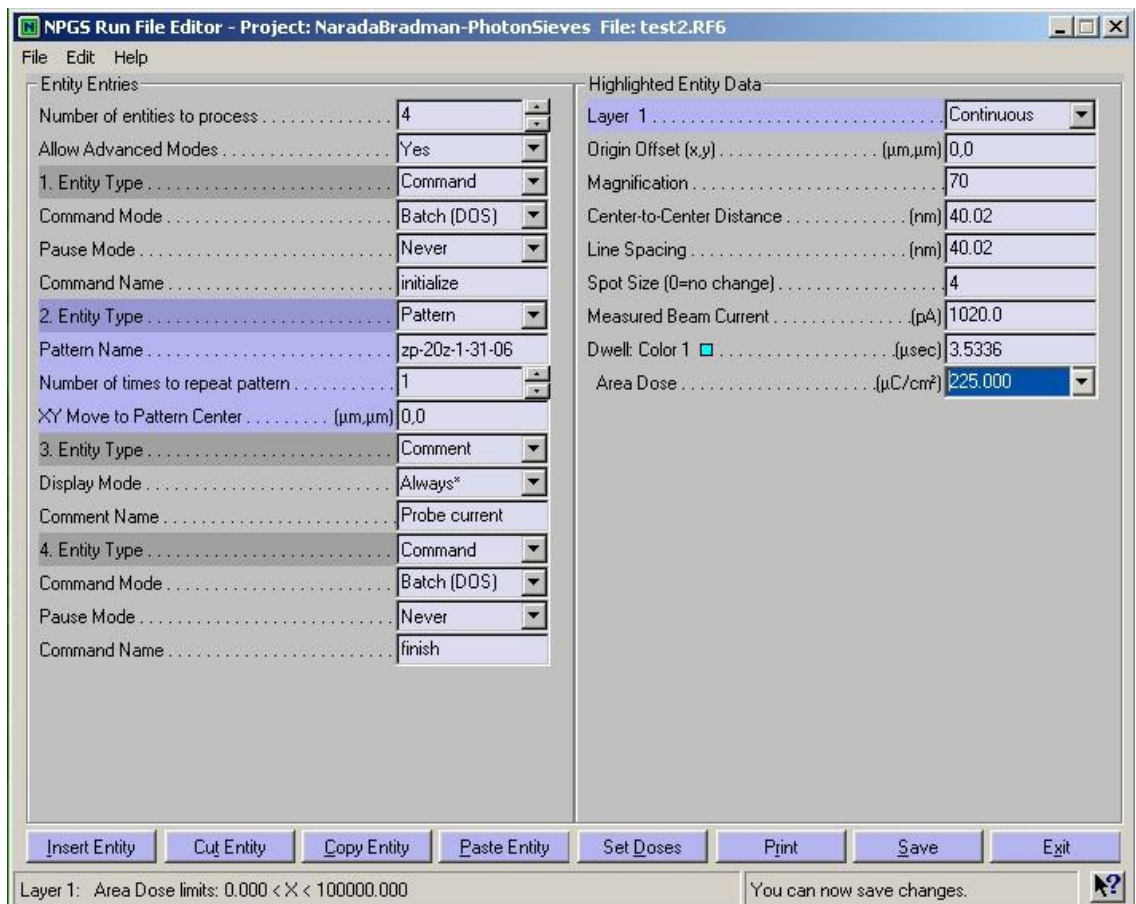


Figure 3-4. NPGS run file. Shown are the pattern file to be written and the interface used to specify the measured beam current as well as the dose to be used in writing the pattern.

The NPGS system was attached to and could control the electron beam of a Philips XL 40 field emission scanning electron microscope (SEM). All of the functions of the SEM were controlled through a computer interface. The XL40 had a large automated stage capable of holding up to five 1" x 1" samples at a time. Generally, two of the five sample positions on the stage were already occupied by a gold standard used to focus and stigmatize the beam, and by the Faraday cup used to measure the beam current. Since there was no load lock, the entire chamber was vented to load or unload samples. The sample chamber was evacuated by a turbomolecular high vacuum pump backed by a mechanical vacuum pump.

The PMMA coated substrates were placed on the sample holder and loaded onto the stage of the SEM. The chamber was closed and pumped down. The accelerating voltage was set to 30 kV, and the probe current is set to spot size 4 (probe current of $\sim 1.2 \times 10^3$ pA). The working distance is set to 10mm, and the beam was focused and stigmatized using a Ted Pella Inc. high resolution gold on carbon standard sample.⁶⁹ After the beam had been focused and stigmatized, the beam current was measured using a Faraday cup to ensure that the entire beam current was collected and secondary emission was suppressed. The Faraday cup consisted of a TEM aperture with a 100 micron hole that has been attached to a sample holder with a drilled hole. A picoammeter attached to the SEM was used to measure the collected probe current. The measured probe current was entered in the NPGS run file. After the probe current had been measured, the stage was moved so the field of view was centered at the edge of the sample. Since the surface of the gold standard and the surface of the sample are at slightly different heights, the height of the stage is adjusted so that the beam was in focus at the surface of the sample.

Although the flatness of the surface was not characterized, the sample was sufficiently flat to avoid variation in the working distance large enough to result in an observable detrimental impact in the lithography. With the beam focused at the sample surface, NPGS was activated and controlled the beam, writing the pattern that had been specified in the NPGS run file. After the NPGS had finished executing the run file, it released control of the beam to the SEM. The beam was turned off, and the chamber back filled with dry nitrogen to bring it up to atmosphere. The sample was removed and placed in a gel box for transportation.

The patterned PMMA was developed by a 90 second immersion in a 1:3 solution of methyl isobutyl ketone and isopropyl alcohol. It was subsequently rinsed with isopropyl alcohol and blown dry using dry nitrogen. Samples were inspected using an optical microscope at 50x magnification immediately following development.

3.2.2.4 Electron beam lithography issues and optimization

There were several issues encountered in the use of electron beam lithography as a patterning process that merit mention and brief discussion.

The field of view of the SEM is determined by the working distance, or the distance from the final aperture assembly to the sample.^{70,71} Because the field of view determines the maximum size of the pattern that can be written, it follows that in order to write larger patterns, the working distance would have to be increased. However, there is a maximum working distance at which lithographic pattern can be successfully achieved. If this maximum working distance is exceeded, the degree of variance in the written pattern from the design pattern can become unacceptably large. There are several factors that contribute to degradation of the lithography at longer working distance; however the

primary culprits are magnetic fields in the vicinity of the lithography tool and mechanical vibration. Magnetic fields in the vicinity of the SEM limit the maximum usable working distance because as the working distance increases, the effect of the magnetic field on the electron beam become more pronounced.^{54,68} To a certain extent, this degradation of the electron beam positioning control can be mitigated by working at higher accelerating voltages. As such, the maximum usable working distance, and therefore the maximum pattern size that can be written, is specific to the electron beam lithography tool used and to the environment in which the tool is used.

It was discussed in Section 3.2.2.2 that the NPGS would allow the electron dose required to expose the resist to be specified as one of the processing parameters. However, there was often a discrepancy between the specified dose and the actual dose received by the sample. This would occur because the specified dose only accounts for the electrons present in the beam and would not take into account the additional flux of electrons backscattered from the substrate. As a result of this additional dose arising from the backscattered electrons, the actual dose received by any given point in a pattern was unique not only to the resist being used, but also to the substrate material, and the density of the elements in the pattern. This problem, known as the proximity effect, is well documented⁵⁴ and a variety of solutions have been proposed and implemented with varying degrees of success. Attempted solutions fall into one of two categories: proximity effect avoidance and proximity effect correction. There are a variety of methods to achieve proximity effect avoidance. Some of the methods include using less sensitive resists or using multilayer resist schemes, and writing at very low energies where the range over which an electron may scatter is less than the smallest element in the pattern.

^{54,72,73} The simplest proximity avoidance method is to iteratively adjust the dose until the elements of the pattern are successfully written with the designed dimensions. Proximity effect correction can also be achieved by a variety of methods. There are three main categories of proximity effect correction: dose modulation, pattern biasing, and a technique called GHOST. Dose modulation involves varying the specified dose for each pattern element taking into account additional electron dose resulting from proximity to other pattern elements. There are a variety of methods that may be used to calculate the dose variation ⁷⁴⁻⁷⁷, however dose modulation in general is computationally intensive and requires specialized software. Pattern biasing involves changing the size of pattern elements to account for the increase in dose they receive from backscattered electrons.^{78, 79} As with dose modulation, this approach is somewhat computationally intensive and requires specialized software. The GHOST proximity correction scheme involves equalizing the background dose by writing the inverse tone of the pattern with a defocused beam.^{80,81}

In this research, the relatively simple method of iteratively adjusting the dose until the elements of the pattern are successfully written with the designed dimensions was used to adjust for the proximity effect.

3.2.3 Pattern Transfer

Pattern transfer was accomplished by means of a sputter etch to transfer the pattern from the resist to the metal thin films. The sputter etch was followed by a resist removal step.

3.2.3.1 Sputter etching

The plasma reactor used for pattern transfer was a PlasmaTherm SLR 770 series electron cyclotron resonance (ECR) system. The PlasmaTherm used a Leybold Turbovac 1000 turbomolecular vacuum pump⁶⁴, backed by a Leybold Trivac BSC mechanical pump to evacuate the main process chamber and a second Leybold Trivac BCS mechanical pump to evacuate the loadlock. The PlasmaTherm is equipped with an ASTEX 4400 ECR plasma source, capable of applying 1000 watts of microwave power at 2.45GHz to ionize process gasses. The sample is biased by a 500 watt RF power supply operating at 13.56 MHz, which acts to accelerate the ionized process gasses toward the sample. A system schematic is shown in Figure 3-5.

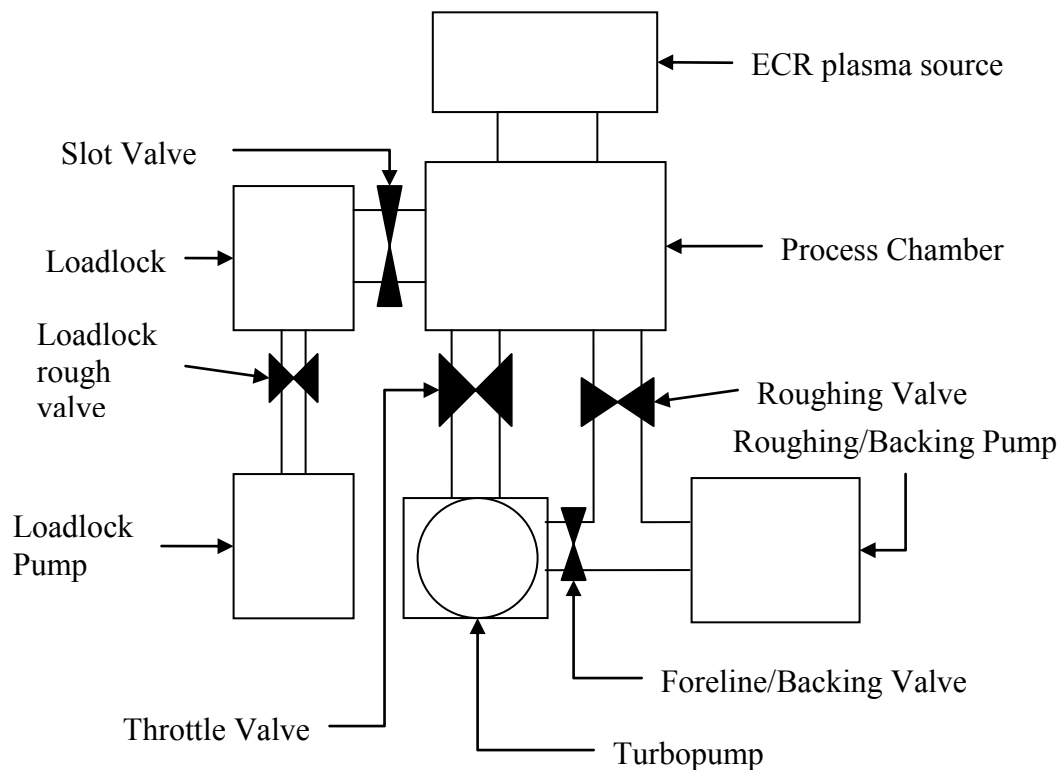


Figure 3-5. PlasmaTherm ECR etching system schematic

The PlasmaTherm allowed control of a number of parameters including process gas flow rate, chamber pressure, RF power, and ECR power and etch time. All of the PlasmaTherm process parameter selection and control parameters were entered via computer interface.

A summary of the process important parameters used to dry sputter etch the silver/nickel films is shown in Table 3-2. A typical pattern transfer run consisted of placing the sample on a 2 inch wafer and loading into the load lock. The load lock was closed and pumped down to approximately

Table 3-2. Sputter etch parameters

Parameter		Units
Process Gas	Argon	
Flow Rate	15	SCCM
Chamber Pressure	1	mTorr
RF Power	100	Watts
ECR Power	800	Watts
Etch Time	15+15	Seconds

3.5 mtorr. While the load lock was being pumped down and before the sample had been transfer to the main process chamber, the process parameters were entered via a computer interface and tested to ensure that a stable plasma could be initiated and maintained. The color of the plasma was also observed to confirm that no residual gasses from a previously executed process remained in the system. After the load lock had completed the pump down cycle and the process parameters had been tested, the wafer and sample were transfer to the main process chamber by an automated mechanical arm. The process gas flow rate and chamber pressure were allowed to stabilize at specified values. The ECR and RF power supplies were activated and until they were automatically shut off after the programmed time interval of 15 seconds. The sample was then removed from

the process chamber to the load lock, which was then vented up to atmospheric pressure. The sample was removed and inspected via optical microscopy. Any debris that were evident on the surface of the sample were removed using a dry nitrogen stream. The sample was subsequently reloaded into the load lock and the entire process repeated to complete the etch.

3.2.3.2 Resist removal

After the sample had been removed from the PlasmaTherm, it was submerged in a beaker of Posistrip EKC830 that had been heated to 80°C on a hot plate.

Posistrip is a resist remover series produced by EKC Technology, a subsidiary of Dupont Electronic Technologies. According to the manufacturer, EKC830 is specifically formulated to remove resist that has been exposed to a harsh process history. The product specification sheet recommends using the resist remover at elevated temperatures, in the vicinity of 75°C.

The sample was left submerged in the Posistrip and maintained at 80°C for 2-3 minutes after which the beaker was placed in an ultrasonic agitator. The sample was agitated until the Positrip had cooled to room temperature, typically 5 minutes.

3.2.3.3 Pattern transfer issues and optimization

A review of literature reveals that a variety of dry etch processes have been investigated to pattern silver. Most prominent among this efforts are the use of halogens as process gases. Examples of gasses used included CF_4 ^{82,83}, CF_4/O_2 ^{83,84}, Cl_2/O_2 ⁸⁵. Plasmas of all of these gasses will react with silver films, however, the etch products are not volatile. Because the etch product of these processes are not volatile, the processes rely on subsequent removal step involving the use of a resist stripper at elevated

temperatures. These processes typically resulted in a rough surface profile and jagged edges on the pattern.

For this research an alternative process was investigated using argon plasma to etch the silver and nickel thin films with the PMMA acting as a mask. The etch was purely physical sputtering with no chemical reactivity to assist in the etch. George⁶⁰ reported that an argon sputter etch could be effectively used to transfer submicron features to a gold thin film using PMMA as a mask. The processing conditions used in research of George⁶⁰ were used as a starting point in developing the pattern transfer process.

Because the etch is entirely physical sputtering, there would be essentially no selectivity with respect to the mask; and because of the relatively low atomic mass of the PMMA its etch rate would be higher than that the etch rate of the metal thin films. However the because PMMA was more than 3 times as thick as the combined metal thin film layers, it would be sufficiently thick act as a sacrificial mask while the silver and nickel layers were etched. It was found that the substrate heating as a result of the plasma bombardment significantly reduced the effectiveness of PMMA as a mask. The PlasmaTherm is equipped with a sample cooling system to alleviate this problem. The cooling system uses a stream of helium applied to the backside of the wafer to remove heat resulting from the plasma bombardment. However, the samples were sitting atop the wafer and in practice it proved difficult to achieve thermal contact between the sample and the wafer to avoid heat build up. To circumvent heat build up in the sample and the resulting accelerated degradation of the PMMA, the etch was divided into several etch steps of 15 seconds each. This approach proved to be effective, resulting in an etch

through the metal thin films while simultaneously reducing the accelerated degradation of the PMMA that resulted from higher temperatures.

The resist removal was initially performed using acetone. Acetone had been previously used to successfully to remove PMMA from substrates. However, the processing in the PlasmaTherm hardened the PMMA to the point that acetone did not completely remove all of the residual PMMA from a sample after the sputter etch step. This hardening probably occurs because of crosslinking of the PMMA which could result from a combination of energy deposited via ion bombardment and from exposure to some ultraviolet radiation from the plasma. PMMA has been know to reverse tone, from positive to negative, when exposed to a dose an order of magnitude in excess of the dose required for exposure. Prolonged ultrasonic agitation at elevated temperatures did not improve removal of the residual PMMA.

An alternative resist removal process was devised using Posistrip EKC830 as a resist removal agent. Posistrip is a resist remover specifically formulated to remove positive photoresist that has been exposed to harsh process conditions. Submerging the sputter etched sample in a beaker of Posistrip at 80°C and subsequently subjecting the sample to ultrasonic agitation proved effective in removing the residual PMMA remaining after the sputter etch processing.

3.3 Conclusions

A relatively simple process to fabricated thin film photon sieves has been developed and tested. The issues associated with the use of PMMA as an etch mask have been address by segmenting the etch process to reduce heating of the PMMA which reduces its etch resistance and by using Posistrip EKC830 as an resist remover.

CHAPTER 4 PHOTON SIEVE PROPERTIES

4.1 Introduction

Photon sieves promise many opportunities to improve on the optical characteristics of the Fresnel zone plate. However, in many instances, capitalizing on these opportunities has resulted in significant trade offs. For example, Kipp¹¹ have shown that an appropriately designed photon sieve occupying the same area, with the same number of transparent zones as a Fresnel zone plate, provides an improved contrast ratio as a result of the suppression of secondary maxima, as discussed above in Chapter 2. However, the photon sieve may suffer from significantly reduced intensity at the primary focus compared to the Fresnel zone plate, primarily as a result of the reduced transmitting area of the photon sieve compared to the zone plate. With an eye towards increasing the transmitting area, several photon sieve patterns were designed. These photon sieve designs were fabricated using the process described in Chapter 3, and tested to characterize their focal length, the maximum intensity at the first order focal point, and their resolution.

This chapter will begin with a description of the testing equipment and procedures. This is followed in Section 4.3 by the results of testing the various photon sieve designs. The results are subsequently discussed in Section 4.4 and the chapter closes with a summary and conclusions in Section 4.5.

4.2 Characterization

The characteristics of the photon sieves that were measured included the maximum focused intensity, the full width at half maximum (FWHM) of the peak intensity, focal length, minimum resolvable separation between two point sources, and the transmitted intensity. The intensity distribution at the focal plane, FWHM of the peak intensity, and focal length of the photon sieve were measured on an optical rail, using a Dataray WinCamD-UCM CMOS detector while the transmission was measured on a separate optical bench, using an Oriel 77345 photomultiplier tube. Because of the differences between the apparatus used in their measurement, the transmission measurements and the peak intensity measurements cannot be directly compared. Both of the experimental apparatus are described in Section 4.2.1.

4.2.1 Characterization Equipment

The illumination source used in the measurement of the focal plane intensity distribution, peak intensity and focal length of the photon sieves was an Ocean Optics LS-1 Tungsten Halogen Light Source with a 900 hour bulb.⁸⁶ The LS-1 is a white-light source optimized for the VIS-NIR (360-2500 nm). The spectral power distribution of the LS-1 as provided by the manufacturer is shown in Figure 4-1.

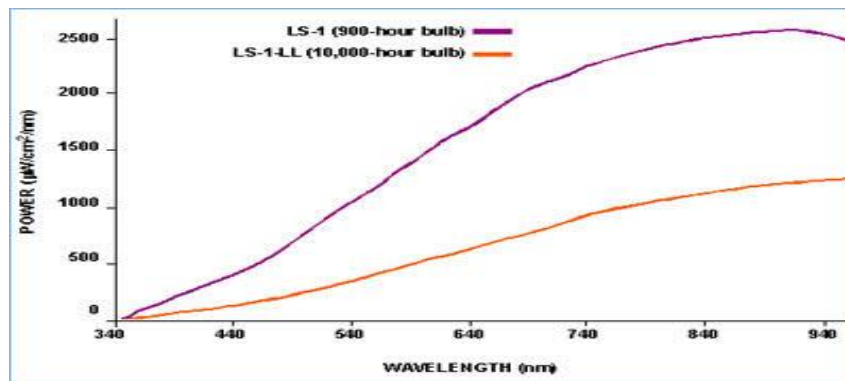


Figure 4-1. Spectral power distribution for the LS-1 illumination source.⁸⁶

The output of the LS-1 illumination source was filtered using an Edmund optics narrow bandpass interference filter with a specified central wavelength of 694nm. The manufacturer specified a central wavelength tolerance of ± 2 nm and a full width half maximum of $10\text{nm} \pm 2\text{nm}$.⁸⁷ The measured spectral distribution of the filtered light is shown in Figure 4-2. The measured central wavelength was 688nm with a full width half maximum of 13nm.

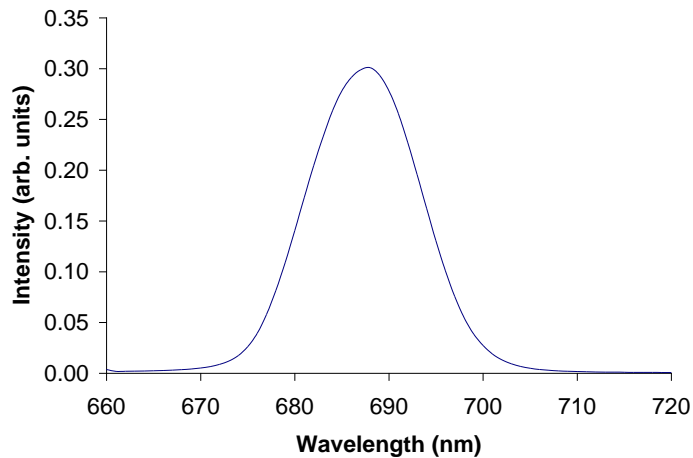


Figure 4-2. Measured spectral distribution of filtered source illumination

The filtered light from the LS-1 source was passed through an Edmund Scientific 100 μm precision pinhole. The 100 μm pinhole was formed in 0.001 inch thick stainless steel and sealed within a 25mm diameter black-anodized aluminum mount for a secure mechanical support. A Dataray Inc. WinCamD was used as a detector. The WinCamD uses a high resolution progressive scan IBIS5A-1300 FillFactory Complementary metal-oxide-semiconductor (CMOS) image sensor with 1280(H) x 1024(V) 6.7 μm^2 active pixels. The detector is also equipped with 4MBs of on-board RAM for image buffering, a FPGA controller and a Cypress CY7C68013 USB 2.0 interface chip.⁸⁸ The detector interfaces with control software installed on a computer via a USB 2.0 connection.

The LS-1 source, narrowband filter, aperture, sample holder and detector were all mounted on an Oriel Corp. optical rail (schematic layout shown in Figure 4-3). The source, filter, aperture and sample holder were fixed while the detector was translated along the optic axis to determine the focal length of the photon sieve.

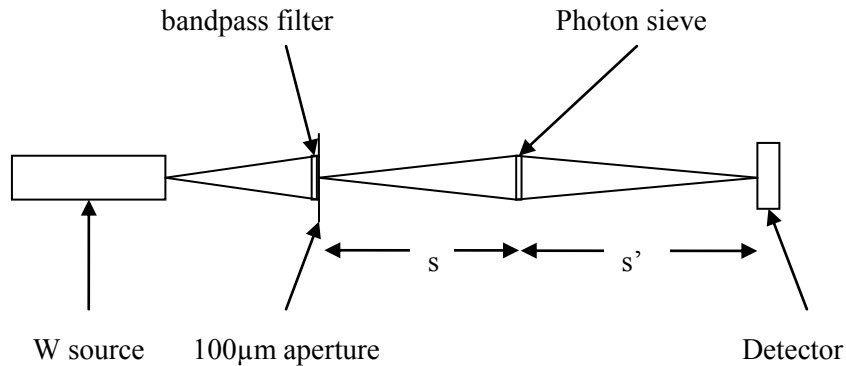


Figure 4-3. Schematic of optical rail. Components include a tungsten halogen illumination source, a 100µm aperture, a narrow band pass filter, a sample holder and a WinCamD CMOS detector. The distance from the source to the photon sieve, s , was fixed at 100mm and the distance from the photon sieve to the detector, s' , was varied to find the focal length.

A slight variation on the setup described was used to measure the resolution of the photon sieves. The 100µm Edmunds Industrial Optics aperture was replaced by a resolution test sample. This test sample consisted of a metallized Fisher Scientific 12-549 microscope slide ($n=1.5$) that had been lithographically patterned with a series of three pairs of 100µm apertures. The pairs of apertures were separated by 100 µm, 18 µm, and 0.5 µm, respectively. As discussed in Chapter 2, the resolution of a zone plate, defined as the minimum separation between two apertures at which the individual apertures can still be resolved, should be determined by the width of the outermost zone. Based on an outer zone width of 14.8 µm, the maximum achievable resolution for the designs tested should be 18µm. The pairs of apertures were separated by distances where they would be clearly

resolved, at $100\mu\text{m}$, barely resolved, at $18\mu\text{m}$ and not clearly resolved, at $0.5\mu\text{m}$. Each of these distances were measured from the edges of the apertures as shown in the SEM micrographs of the aperture pairs are in Figure 4-4a. The test sample was then mounted on a translating slide so that a particular pair of aperture could be imaged. The modified test setup is shown in Figure 4-4B.

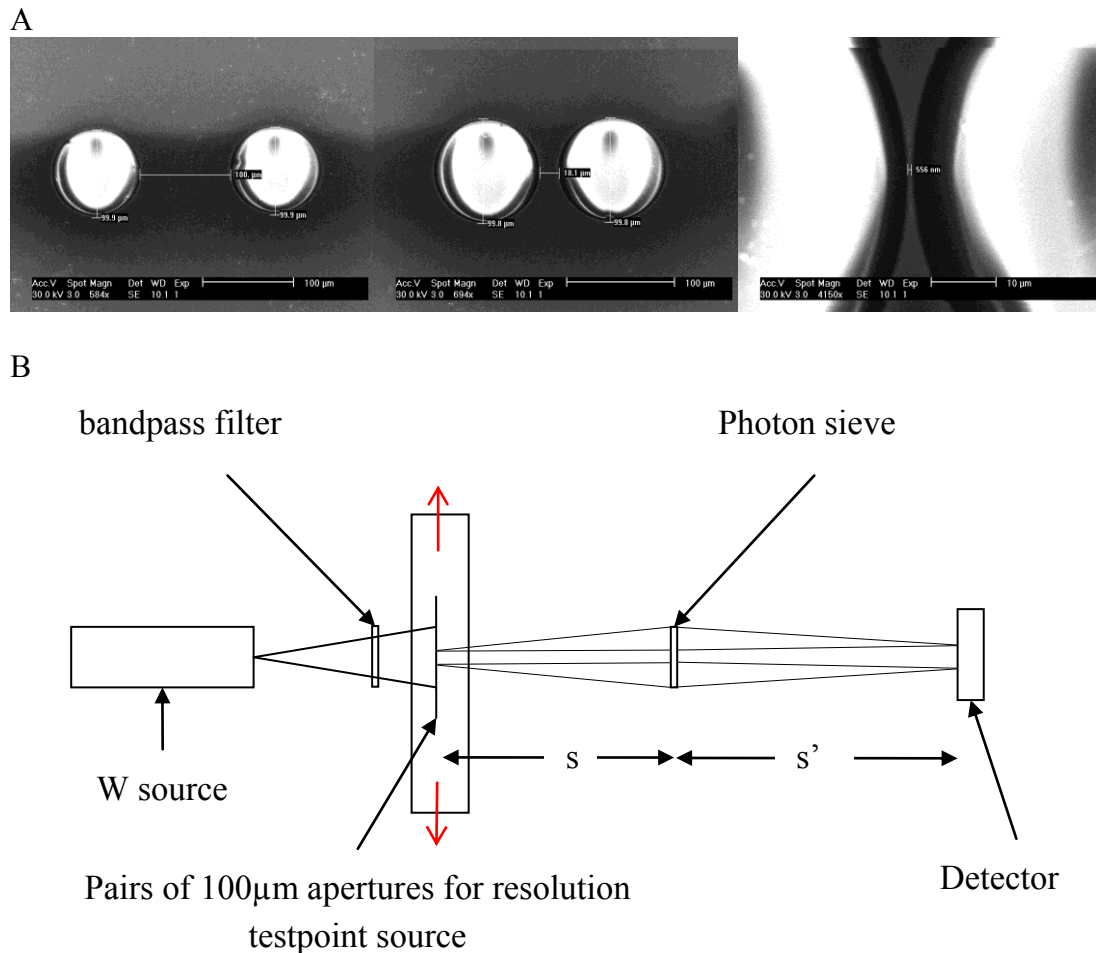


Figure 4-4. Apertures for resolution test and modified test setup. A) SEM micrographs of a resolution test sample consisting of $100\mu\text{m}$ diameter aperture pairs separated by $100\mu\text{m}$ (left), $18\mu\text{m}$ (center), and $0.5\mu\text{m}$ (right at higher magnification of 4150X). B) a modified setup for resolution test with $100\mu\text{m}$ aperture replaced with the resolution test sample mounted on a stage. Stage translation (red arrows) allowed selection of a specific aperture pair.

The transmission of each photon sieve design was characterized using a second optical bench. On this optical bench, illumination from a tungsten halogen source was passed through a 3mm aperture, the sample and the narrow band pass filter. The narrow band pass filter was used to avoid variation between the various experimental setups and allow for the possibility of comparing results from the different setups. The light transmitted was passed via reflective optics to an Oriel MS257 0.25m monochromator. An Oriel model 77345, silicon-based photomultiplier tube (PMT) capable of detecting incident light up to 800nm was used to detect the transmitted intensity. An Oriel Merlin radiometry system was used to interface and control both the monochromator and the detector. The Merlin system also made use of a chopper system that was phase locked to the detector in order to improve the signal to noise ratio. A schematic of the second optical bench is shown in Figure 4-5.

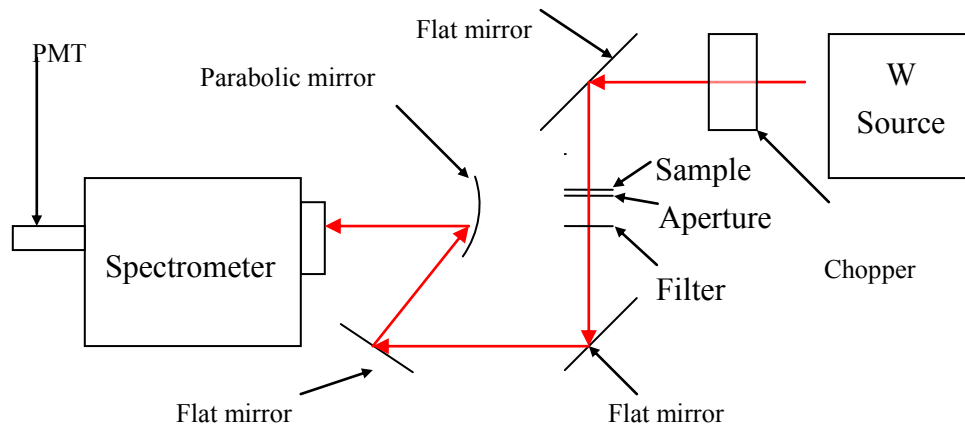


Figure 4-5. Schematic of optical bench used for transmission measurements. Components of note include a tungsten broadband illumination source, a 3mm aperture, a grating spectrometer, and a photomultiplier tube used as a detector.

4.2.2 Characterization Procedures

With the optical rail setup in Figures 4-4, the illumination source was turned on and allowed to stabilize for 30 minutes before any measurements were made. Once the source

had stabilized, the sample was mounted in the sample holder without the narrow bandpass filter in place. This allowed any adjustments in sample position required to bring the photon sieve being tested into alignment. The filter was then placed in line and the cap on the detector was removed. The position of the 100 μm point source aperture and the photon sieve fixed, and the focal length was found by varying the position of the detector to find the position resulting in the smallest spot size and to the maximum measured intensity. An image of the intensity distribution at the focal plane and the intensity profiles in the horizontal and vertical directions were then captured for measurement of the FWHM. This procedure was repeated for each of the photon sieve designs.

The 100 μm point source aperture was replaced with the 100 μm pair resolution test sample, which was mounted on a stage. The stage allowed translation to select which of the aperture pairs was being imaged. The detector was fixed at the previously determined position corresponding to maximum measured intensity and images of the intensity distribution at the focal plane and the raw data of the intensity profiles in the horizontal and vertical directions were then captured for each of the aperture pairs.

The photon sieve was placed on the second optical bench in the position shown in Figure 4-5. The intensity at each wavelength was measured in 1nm increments across the transmission window of the narrowband filter, from 660nm to 720nm in order to measure the transmission for each design. This was done for each of the photon sieve designs.

4.3 Photon Sieve Design Variations

The traditional photon sieve design was generated by replacing the completely open zones of a FZP with a distribution of discrete circular apertures. Several modifications to the design of the traditional photon sieve were considered for

development of increased transmitting area. The first modification considered was the degree of apodization. As described in Chapter 2, apodization consist of adjusting the open area of a photon sieve in such a way as to create a smooth transmission window to reduce the intensities of the higher order maxima. Apodization was achieved by using a cosine function to modulate the open area of the photon sieve. In order to determine how significant an effect the degree of apodization would have, several designs were developed. Each design consisted of a photon sieve in which the onset of apodization was varied (Table 4-1).

The second modification considered was hybridization of the photon sieve pattern. Hybridization consisted of borrowing elements of the Fresnel zone plate and incorporating them into the photon sieve. Specifically, a number of the zones close to the center of the diffractive lens were continuously open as in a FZP rather than populated with discrete apertures as in the traditional photon sieve. From the onset of apodization to the outer edge of the diffractive lens, zones were populated with large numbers of discrete circular apertures as in traditional photon sieve (Table 4-1).

The third modification to the photon sieve design was the replacement of the circular apertures with zone segment apertures. Filling a Fresnel zone with circular apertures will result in a loss of useful transmitting area. Using an aperture whose shape conforms to the shape of the zone would result in a more complete use of the available transmitting area. In these designs, the apodized zones were populated with discrete apertures resembling segments of the underlying zone (Table 4-1).

The final design modification considered was varying the aspect ratio of the segmented zone apertures. Use of large aspect ratio apertures would allow a small

increase in transmitting area. In these designs, the apodized zones were populated with discrete apertures shaped resembling segments of the underlying zone, but with the circumferential extent of the aperture extended to be 2, 3 or 4 times larger than the radial extent. Representative images of these modifications are shown in Table 4-1.

4.3.1 Photon Sieves with Various Degrees of Apodization

The development of a photon sieve design begins by selecting the wavelength of light that will be focused. As discussed in Chapter 2, Equation 2-17 can be used to determine the radial placement of the even and odd Fresnel zones. The processing requirements to maintain optimal conditions for the electron beam lithography were a limiting factor in selecting the diameter of the photon sieve. As the diameter of the outermost zone gets larger, a larger field of view is required to write the pattern. To increase the field of view, a larger working distance is required. However, increasing the working distance increases the distance that electrons must travel in free flight (after leaving the influence of the magnetic lens in the column of the SEM). As the working distance increases, the effect of stray magnetic fields in the vicinity of the SEM becomes increasingly pronounced, resulting in a degradation of the written pattern. If the immediate environment of the SEM is not shielded perfectly from magnetic fields, it is best to minimize the working distance used to reduce the time any magnetic fields would have to affect the trajectory of the electrons after leaving the final lens assembly. This limits the field of view and subsequently limits the size of the pattern that can be written. Experience has shown that the optimum working distance for electron beam lithography in the SEM in the environment at the Major Analytical Instrumentation Center occurs at 10mm. This results in a field of view of $2600\mu\text{m}^2$. However, because the beam is typically poorly focused at the edges of the field, it is advantageous to limit the maximum

size of the pattern to approximately 90% of the field of view. This resulted in the diameter of the photon sieve being limited to $\sim 2.4\text{mm}$. As such the diameter of the outermost zone was specified and used to determine the focal length. The calculated focal length was 50.7mm for a wavelength of 700nm .

Table 4-1. Diffractive lens designs

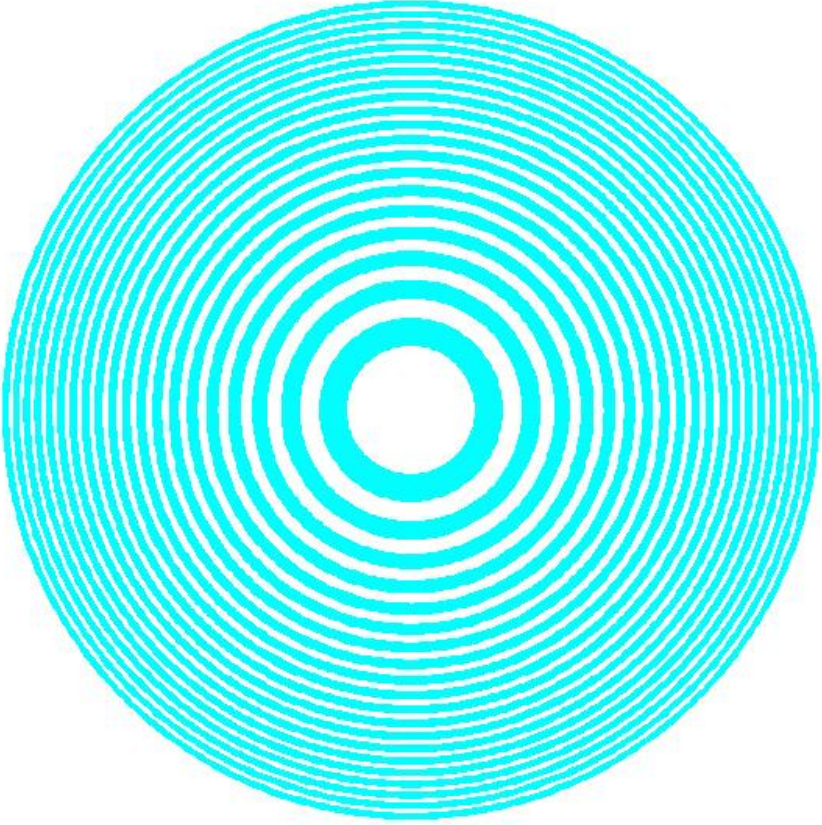
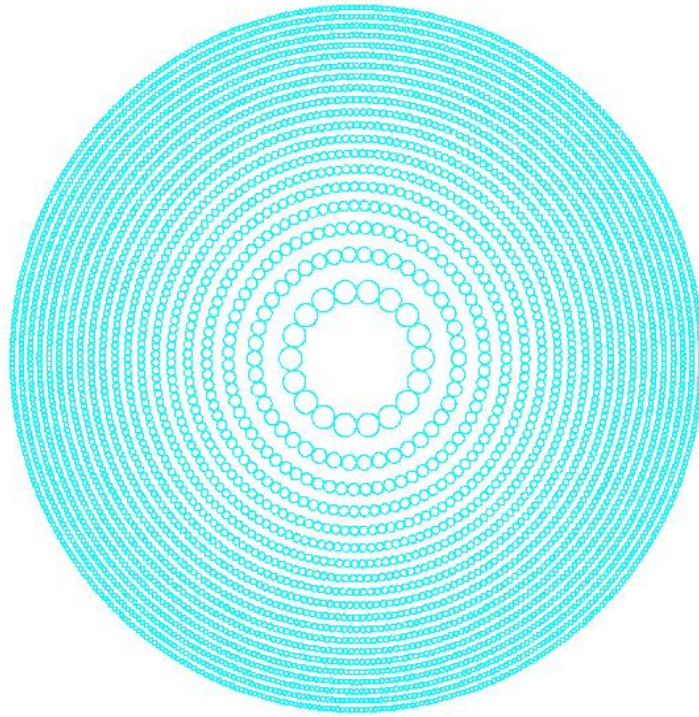
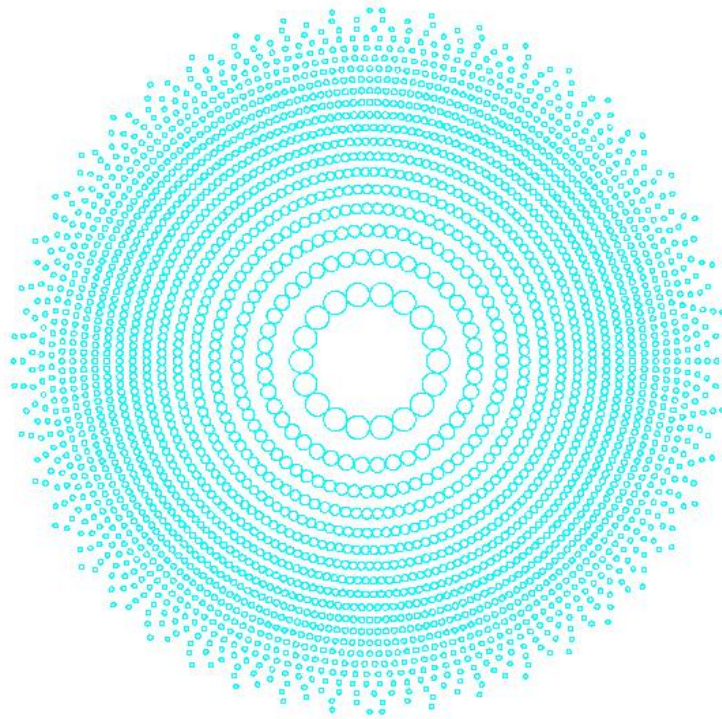
Representative Image
 <p data-bbox="792 1476 927 1507">Zone plate</p>

Table 4-1. Continued

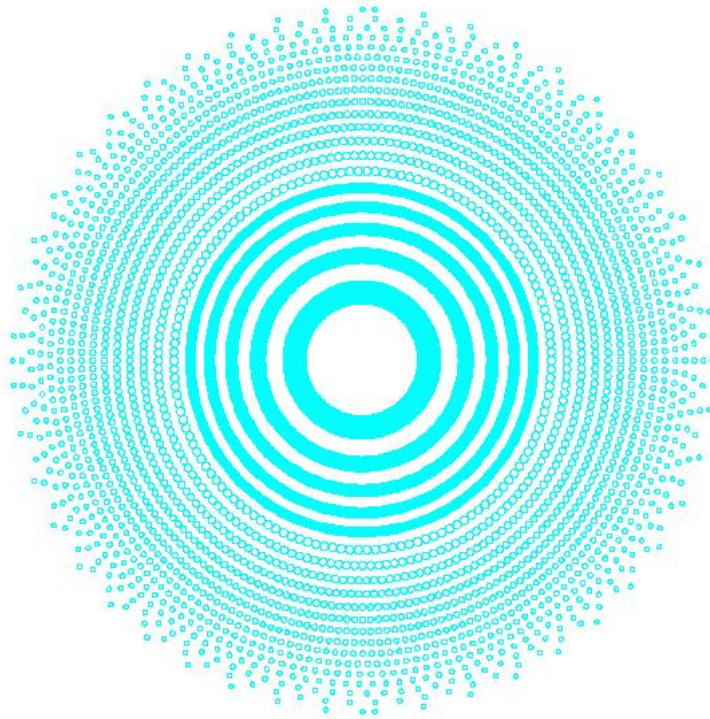


Photon sieve

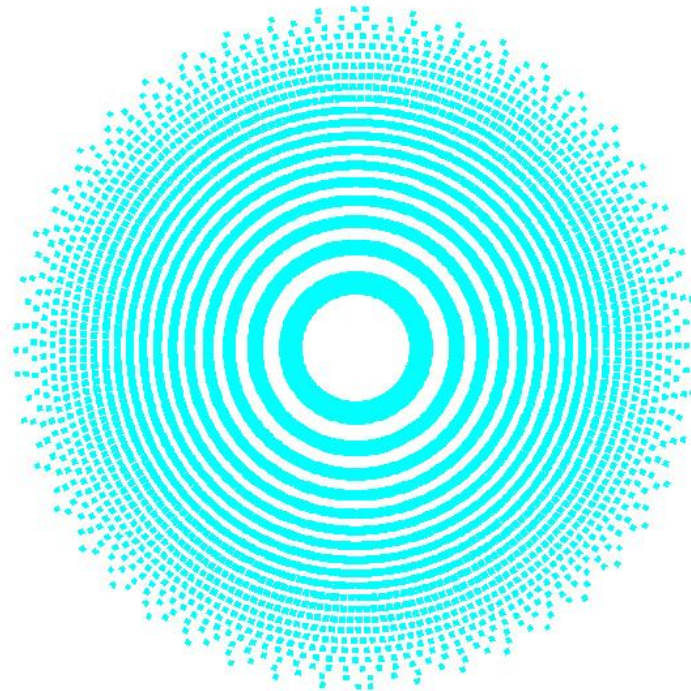


Apodized Photon sieve

Table 4-1. Continued

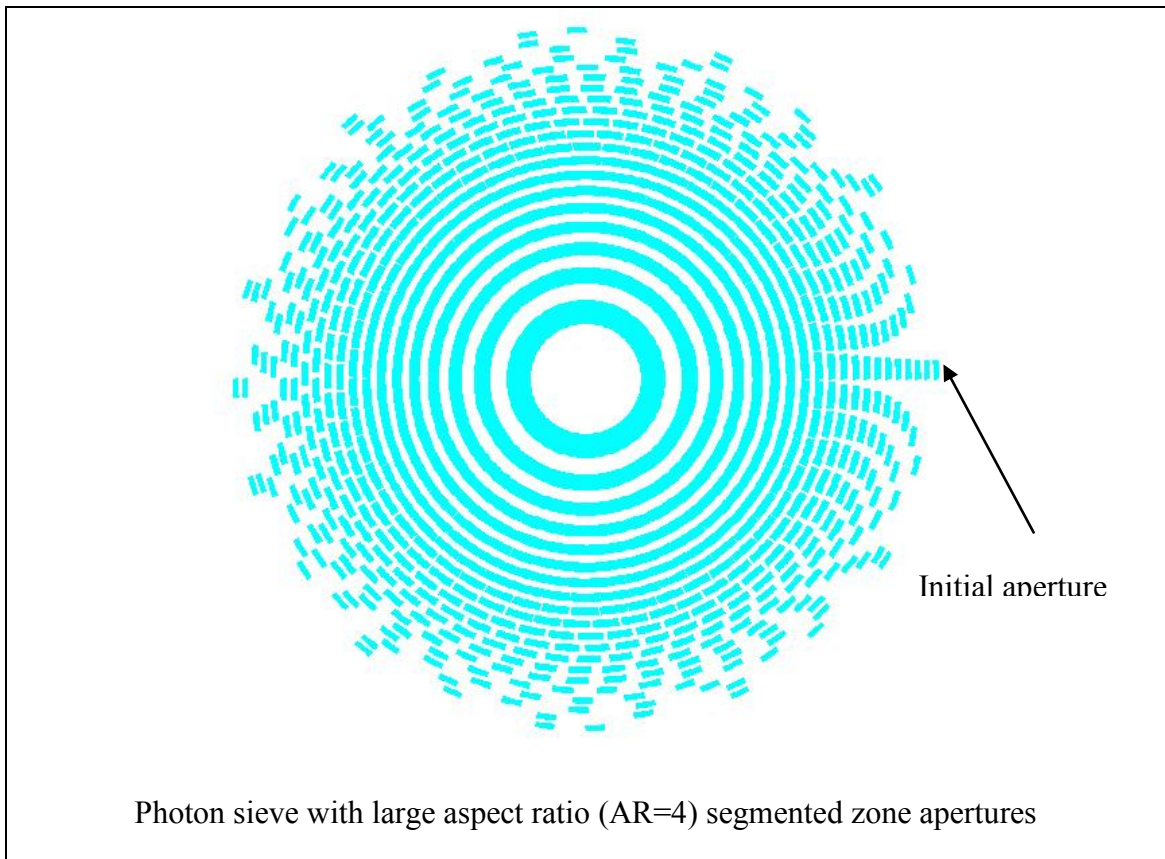


Hybrid Photon sieve w/ circular apertures



Photon sieve with segmented zone apertures (AR=1)

Table 4-1. Continued



The next step in the development of the photon sieve design is to populate all of the even zones of the Fresnel zone plate pattern with transmitting pinholes. Two main criteria were responsible for determining the maximum density of pinholes possible in each zone. The first of these criteria is the width of the zone that the pinhole is occupying. Although Kipp¹¹ has shown that the pinholes can have a diameter several times as large as the width of the zone they are occupying, in these designs the diameter of the pinhole was limited to the width of the zone. Because the width of the zone determines the diameter of the pinhole, it also determines the maximum number of pinholes that can fit in the zone. The second criterion was determined by the limitations of the lithography system used. In any lithographic patterning system, there is some maximum density of pattern

elements that is possible before the fidelity of individual pattern elements is lost. As described in Chapter 3, the maximum pattern density for the electron beam lithography system is defined by the tolerable proximity dose which in turn is determined by a number of interrelated variables including the accelerating voltage on the electron beam, the resist used and the composition of the substrate beneath the resist. In the photon sieve design, the pinholes are spaced such that in a zone populated at maximum density, the closest any individual pinhole may be to another pinhole is $0.5 \mu\text{m}$. A photon sieve with each zone maximally populated in this way is shown in Figure 4-6.

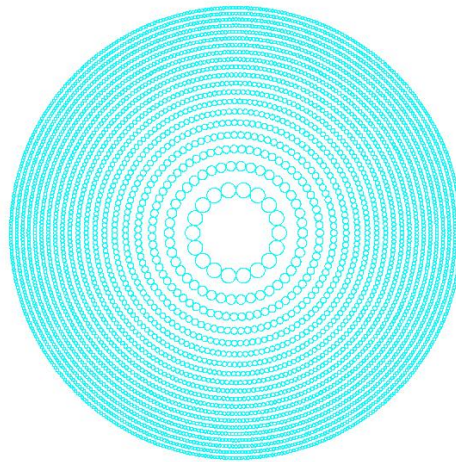


Figure 4-6. A photon sieve created by populating the even Fresnel zones with a maximum density of circular apertures

The photon sieve design in Figure 4-6 is completely unapodized and as a result has a transmission window similar to that of a FZP. As discussed in Chapter 2, there are a number of continuous functions commonly used to generate a smooth transmission window. For these designs a cosine function was used to gradually decrease the density of pinholes in each subsequent zone for a smooth transmission window. An example of the implementation of the cosine function can be seen in Equation 4-1.

$$n = \cos\left(\frac{90 \cdot t}{s}\right) \cdot \left(\frac{c}{2 \cdot r + 1}\right) \quad 4-1$$

where n is the number of pinholes in a particular zone, t is an integer defined by the current zone, s is the total number of zones over which the function is being applied, c is the circumferential distance around the zone, and r is the radius of the pinhole. The “1” in the denominator of the second term of the equation results from the lithographic limitations. An example of how this function is applied to apodize a portion of the open area of a diffractive lens is outlined below.

In order to determine the effects of apodization on transmission and resolving power of the lenses, the zone in which the onset of apodization occurred was varied to produce three designs. The onset of apodization was varied to generate three designs. As an example, consider the first design, in which 25% of the original total open area of the photon sieve was apodized. Recall from Chapter 2 that the width of each of these zones is defined such that all of the zones have equal area. If the photon sieves consist of 20 open zones populated with pinholes, 5 of those zones represent 25% of the total area of the photon sieve. Therefore, for the first design, the cosine function used to apodized the photon sieve was applied over the last 5 zones of the sieve. For the second design, the apodizing cosine function was applied over the last 10 zones, resulting in 50% of the original area of the photon sieve being apodized and for the third design the cosine function was applied over 15 of the 20 zones resulting in 75% of the original area being apodized. Varying the onset of apodization resulted in two immediately observable variations in the patterns generated. First, the slope of the apodization function varies inversely to the percentage of the area that was apodized. This can be seen in the plots of

calculated area versus zone number (area distributions) for a FZP and apodized photon sieves with circular apertures, shown in Figure 4-7.

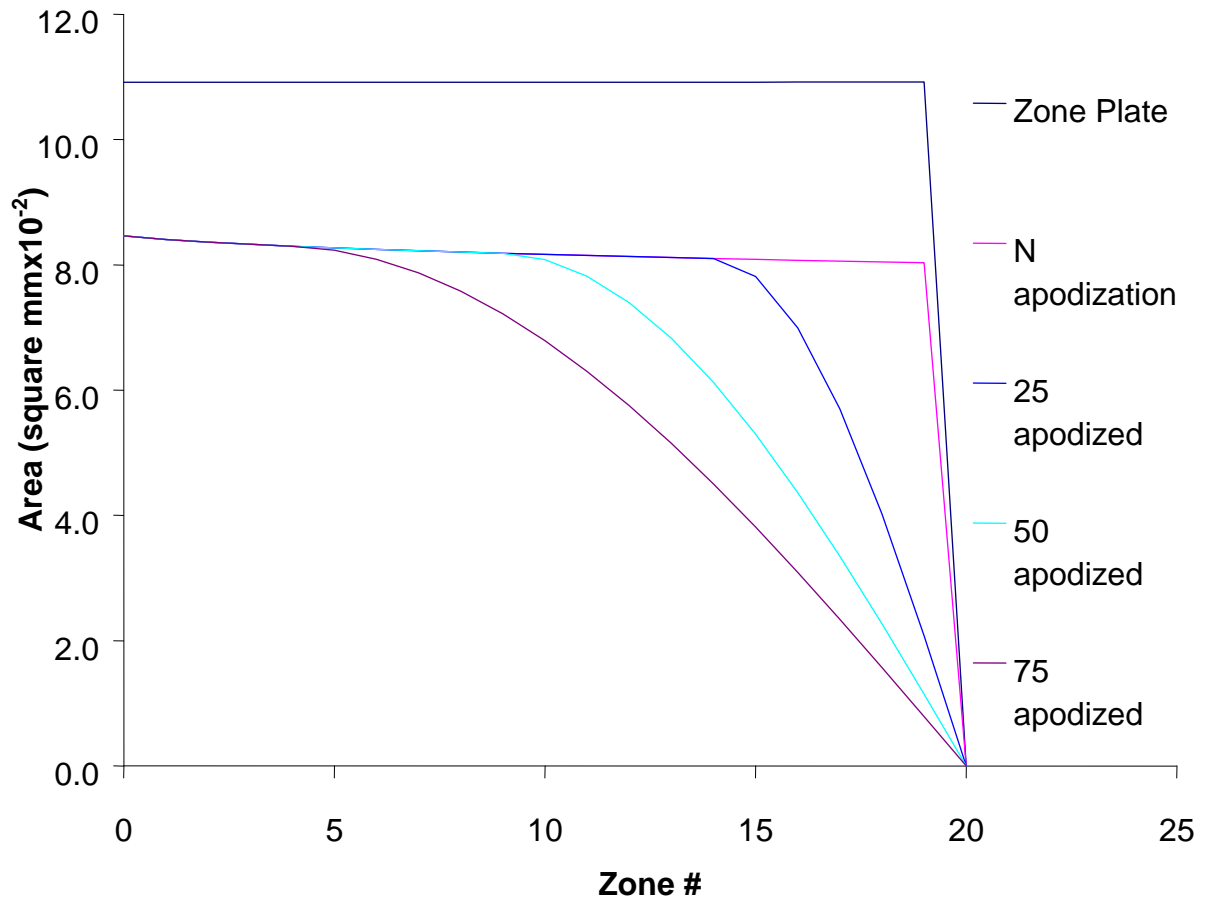


Figure 4-7. Calculated transmission window of a FZP and photon sieves with circular apertures, with and without apodization.

This plot of area versus zone number will be referred to as the transmission window. Second, by inspecting the transmission window shown in Figure 4-7, the total transmitting area also varies inversely to the degree of apodization. The calculated total transmitting areas in square millimeters and as a percentage of the open area of a FZP for each design are tabulated in Table 4-2.

Table 4-2. Calculated open area of FZP and various photon sieve patterns with circular apertures

Pattern	Open Area(mm ²)	Percent of zone plate area
Zone Plate	2.18	100
No Apodization	1.64	75.1
25% Apodized	1.50	68.8
50% Apodized	1.36	62.1
75% Apodized	1.21	55.4

Although the open area of each design was not measured directly to confirm the veracity of the calculations, the trends in the transmission measurements, shown in Figure 4-8, are consistent with the calculated open area tabulated in Table 4-2. Quantitative comparisons of the trends in the calculated open area and the measured transmission are made in Section 4.4.

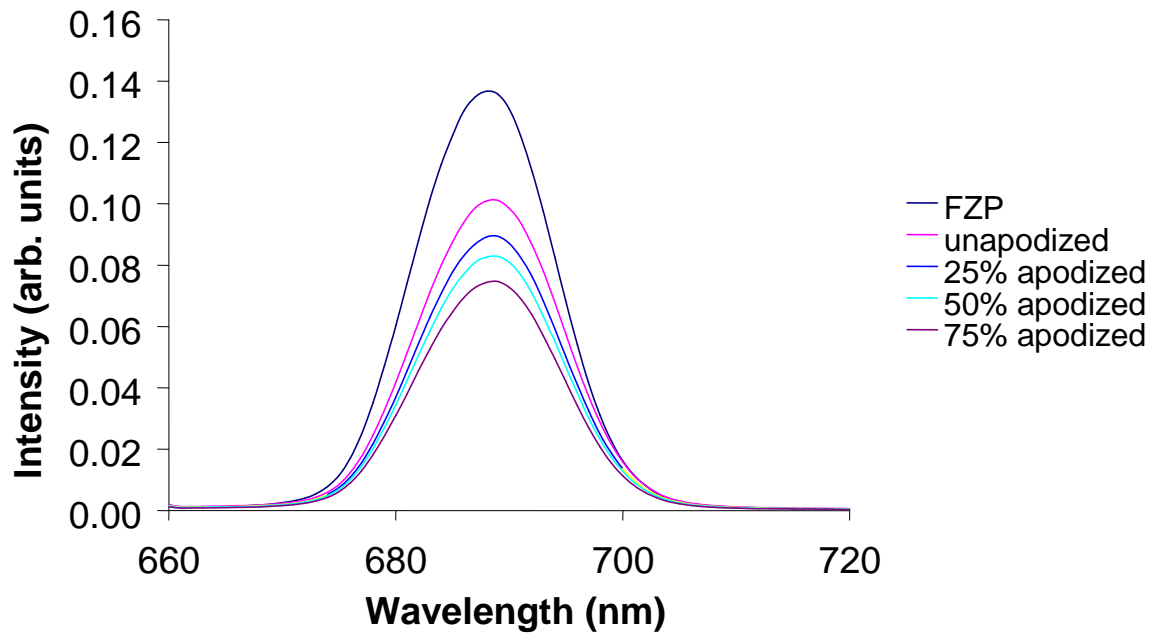
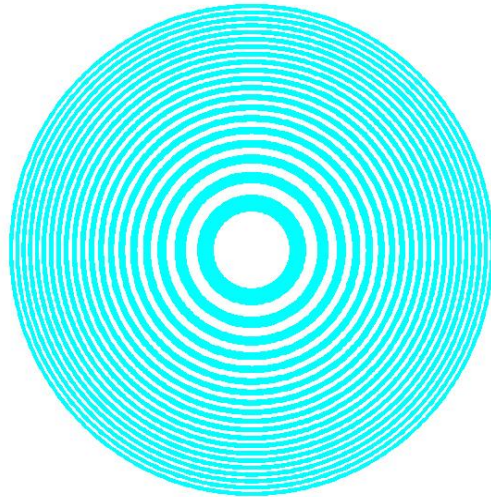


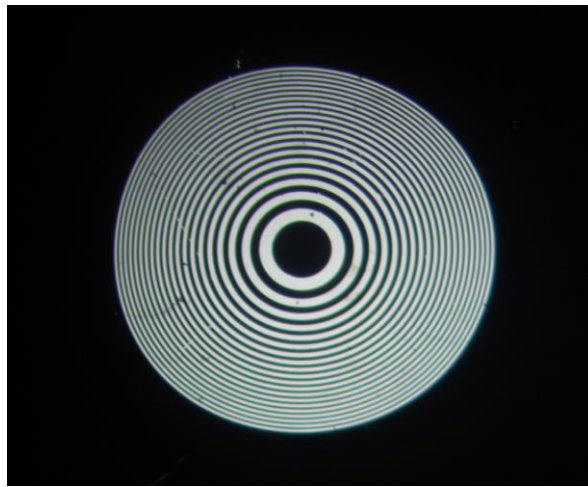
Figure 4-8. Measured transmissions of the Fresnel zone plate (FZP), unapodized photon sieve, 25%, 50%, and 75% apodized photon sieves.

As expected, a reduction in total transmitting area of the apodized sieved resulted in a reduction of the intensity of the transmitted light. However, since Kipp had established that apodization could reduce secondary maxima and subsequently improve image quality¹¹, it was of interest to investigate to what extent the degree of apodization would affect the FWHM and maximum intensity at the focal point. DesignCad representations of each of the patterns, accompanied by optical and SEM micrographs of the fabricated design, are shown in Figures 4-9 through 4-13 for a FZP, unapodized PS, 25% apodized PS, 50% apodized PS and 75% apodized PS, respectively, all PSs with circular holes. The optical and SEM micrographs show that the fabricated photon sieves conform to the intended designs.

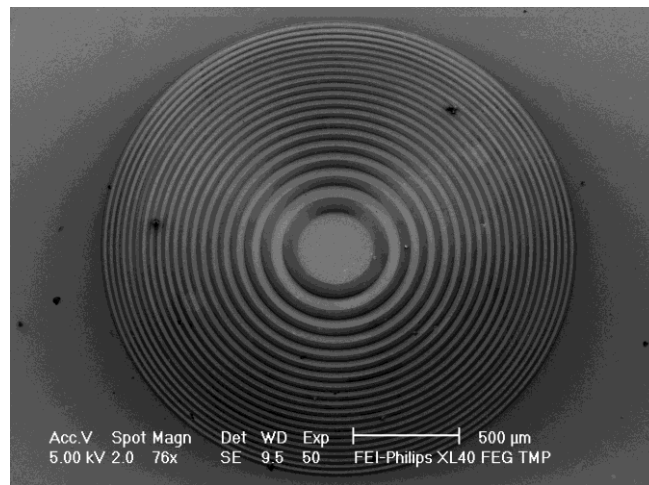
The intensity of the first order peak for the photon sieve designs is shown in Figure 4-14, with the transmission intensity of the zone plate included as a reference. The intensity at the focal point for the unapodized PS is 60% of that for the FZP, and as the degree of apodization increases the intensity at the focal point of the PS decreases, dropping to 50% of the FZP at 75% apodization. The full width half maxima (FWHM) of the spot size resulting from focused transmission through the photon sieve designs are shown in Figure 4-15 along with the FWHM of the intensity distribution pattern for transmission through the zone plate, which is included for reference. Inspection of the FWHM for each of the designs shows that while there is a suggestion of a decreased FWHM at larger degrees of apodization, the error bars show that this trend may not be significant.



A

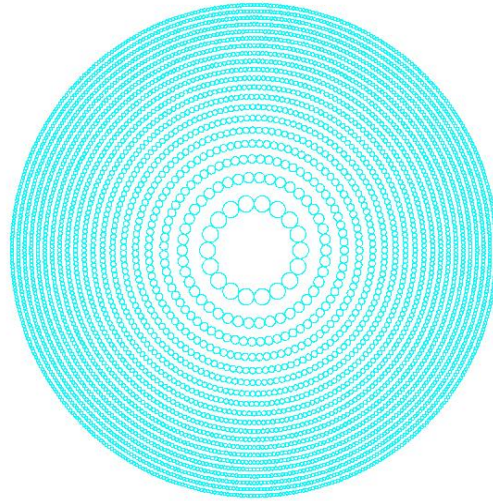


B

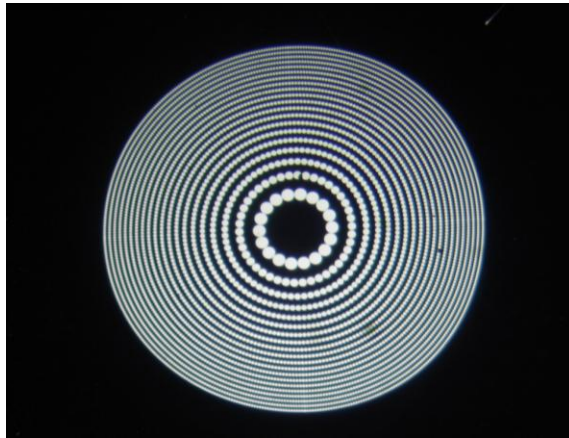


C

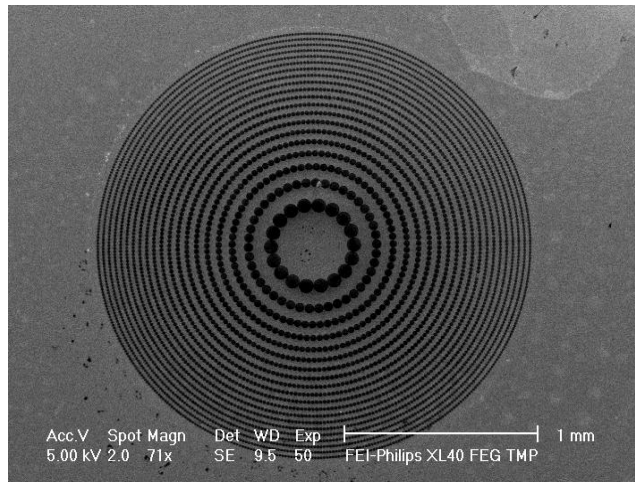
Figure 4-9. The Fresnel zone plate. A) DesignCad representation of FZP. B) Optical micrographs of fabricated FZP. C) SEM micrographs fabricated FZP



A

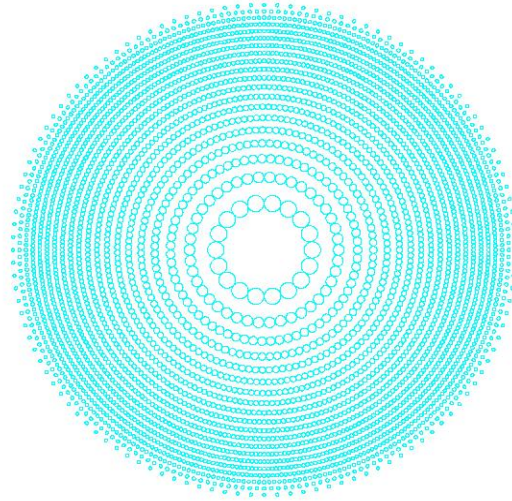


B

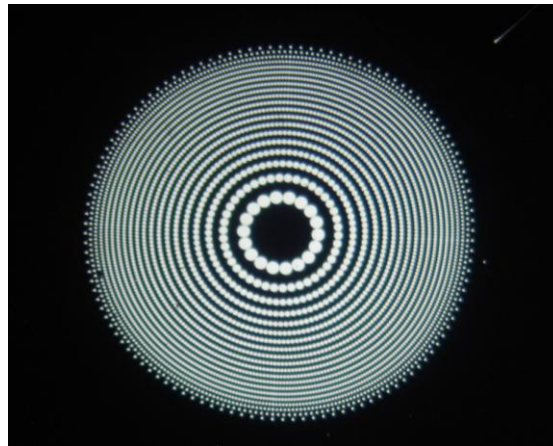


C

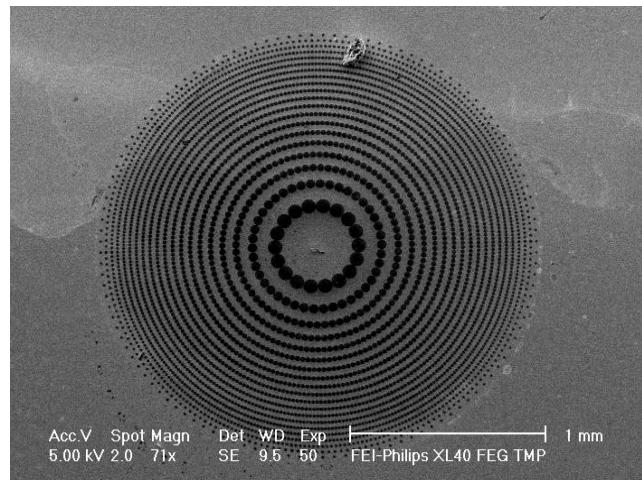
Figure 4-10. Unapodized photon sieve. A) DesignCad representation of unapodized PS. B) Optical micrographs of fabricated PS. C) SEM micrographs of fabricated PS.



A

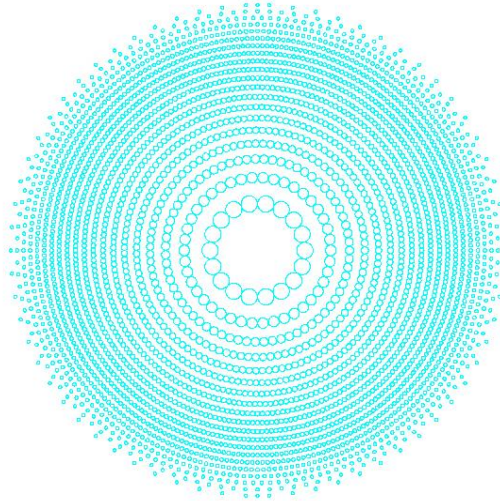


B

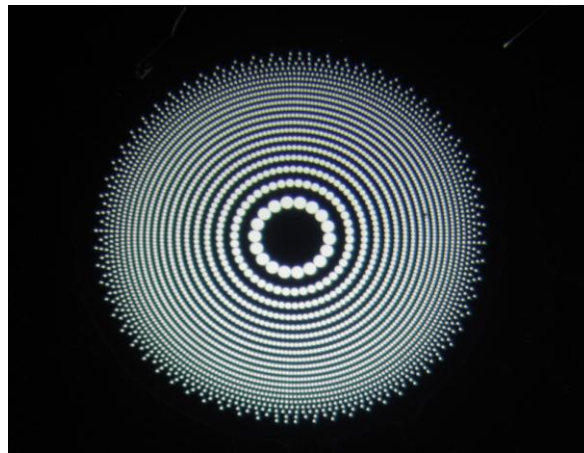


C

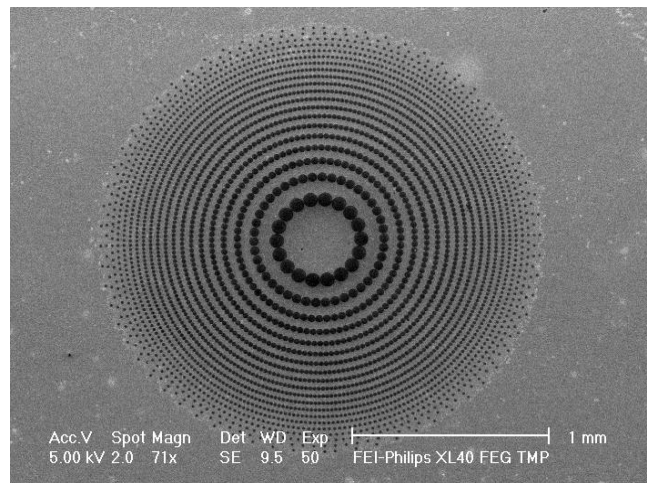
Figure 4-11. 25% apodized photon sieve. A) DesignCad image of 25% apodized PS. B) Optical micrographs of fabricated PS. C) SEM micrographs of fabricated PS.



A

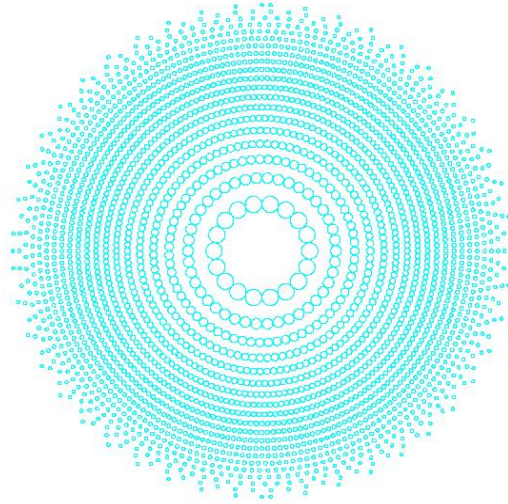


B

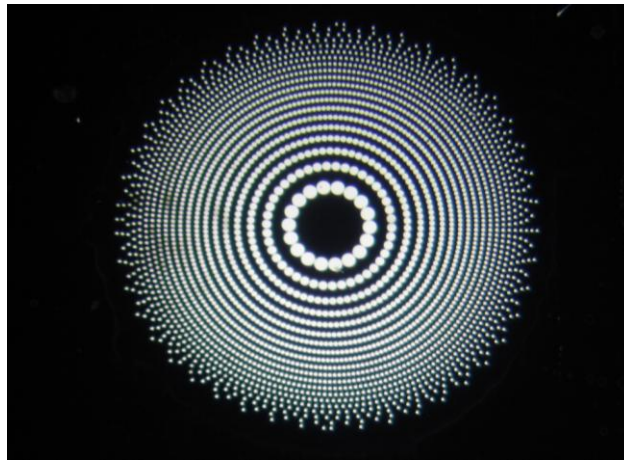


C

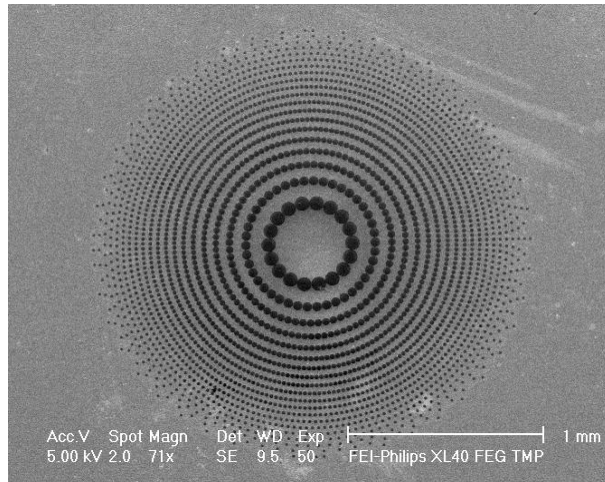
Figure 4-12. 50% apodized photon sieve. A) DesignCad image of 50% apodized PS. B) Optical micrographs of fabricated PS. C) SEM micrographs of fabricated PS.



A



B



C

Figure 4-13. 75% apodized photon sieve. A) DesignCad image of 75% apodized PS. B) Optical micrograph of fabricated PS. C) SEM micrographs of fabricated PS.

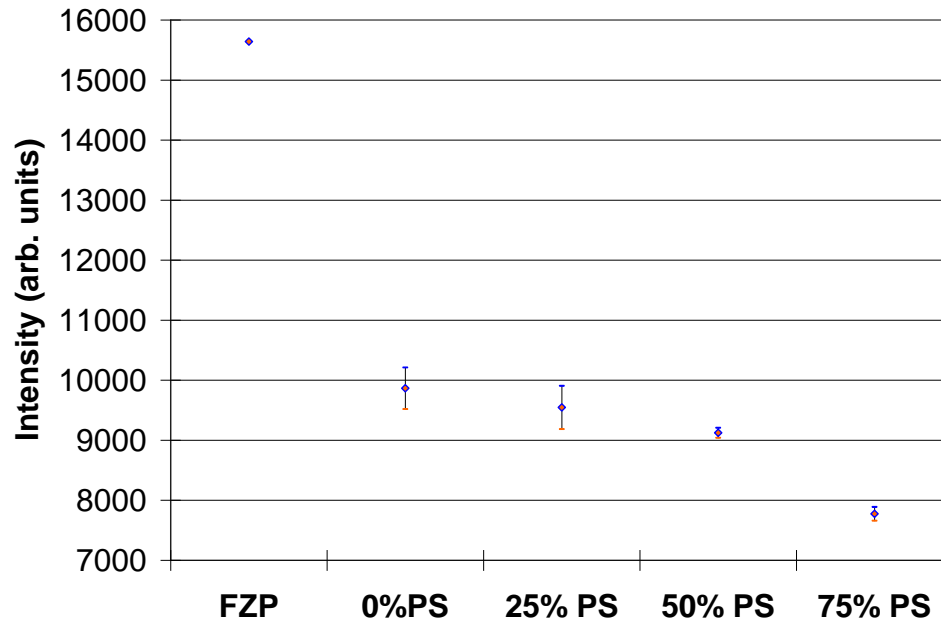


Figure 4-14. Intensity of first order peak. Intensity for the various photon sieve designs.

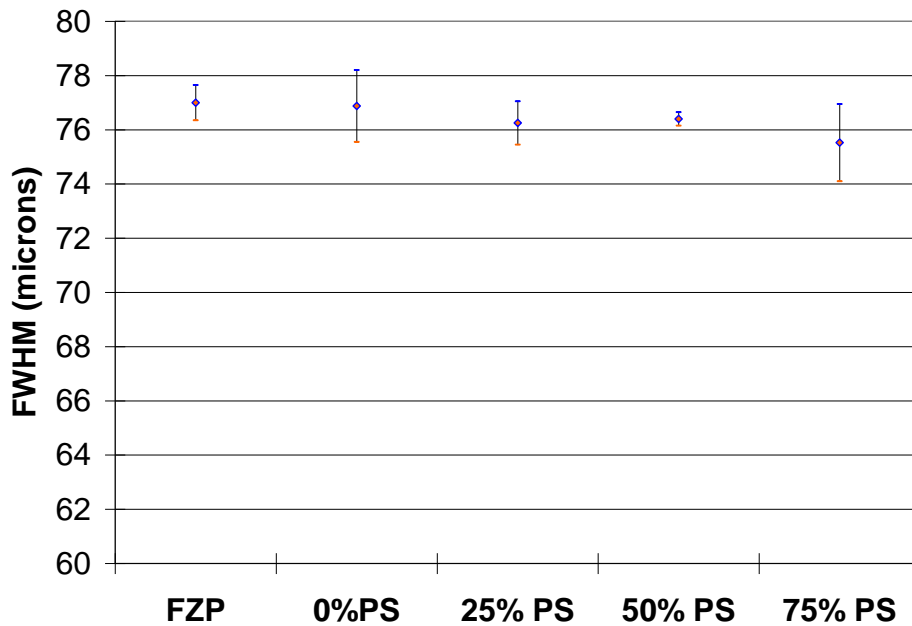


Figure 4-15. FWHM of first order peaks. FWHM of the Fresnel zone plate , the unapodized photon sieve , the photon sieve with 25% of it's area apodized, the photon sieve with 50% of its area apodized and the photon sieve with 75% of its area apodized

4.3.2 Hybrid Lenses with Circular Apertures

The calculated transmission windows (distribution of open area versus zone number) for the FZP and PSs (Figure 4-7) show that even the zones of the photon sieves that are not apodized contribute significantly less transmitting area than the equivalent zones of the FZP. For example, consider the 25% PS, in which 15 of the 20 zones are unapodized. The summed open area of the apertures in the unapodized zones is 124mm^2 compared to 164mm^2 for the first 15 zones of the FZP. As discussed above in Section 4.3.1, this smaller open area for PSs occurs in part because of limitations of the lithographic process which restricts how closely individual apertures can be placed, and in part as a result of the incomplete filling of the zone due to the circular shape of the open apertures. The incomplete filling of the zone by the open circular aperture is directly analogous to a circle inscribed in a square. As a result, the transmitting area is reduced even though the transmission window of these unapodized zones has the same shape as the completely open zones of a FZP. This similarity in the shape of the transmission window results because there is no variation in the density of apertures across these zones. Adopting the completely open zones of the FZP in the place of the unapodized zones would result in an increase in transmitting area without changing the shape of the transmission window over the affected zones. Because contribution from the zones still transition to zero transmission relatively smoothly, the oscillations in the diffraction pattern (i.e. secondary maxima) that result from an abrupt drop in transmission could be avoided. This change in design would allow an increase in the intensity of the primary focus without increasing the contribution to the intensity of the secondary maxima. Therefore the hybrid PS design consists of completely open zones like in a FZP out to the zone where apodization begins, after which the zones are filled with circular apertures,

with a distribution modulated by the cosine function in the outer zones. The calculated open areas of a FZP and each of the hybridized and normal photon sieve designs are compared in Table 4-3.

Table 4-3. Calculated open area of hybrid photon sieve patterns

Pattern	Open Area(mm ²)	Percent of zone plate area
Zone Plate	2.18	100
25% Apodized Hybrid PS	1.90	87.2
25% Apodized PS	1.50	68.8
50% Apodized Hybrid PS	1.62	74.1
50% Apodized PS	1.36	62.1
75% Apodized Hybrid PS	1.34	61.2
75% Apodized PS	1.21	55.4

Hybridizing the photon sieve pattern results in a 27% (from 1.5 to 1.9mm²) increase in transmitting area for the 25% apodized design, a 19% increase (from 1.36 to 1.62mm²) for the 50% apodized design and a 11% increase (from 1.21 to 1.34mm²) for the 75% apodized design. Plots of the calculated open area as a function of open zone number are shown in Figure 4-16. The measured transmission of the FZP and of each of the hybrid designs are shown in Figure 4-17. The total integrated transmission of the 75%, 50% and 25% apodized hybrid design are 59%, 69.5% and 88.6% of the FZP, respectively.

Although the distribution of open area in Figure 4-17 shows that the transmission window for the unapodized portion of the photon sieve remained essentially the same for

the different designs, the plots also show that a discontinuity was introduced at the interface of the unapodized and apodized zones. The sharp drop in area results from the reduction in transmitting area resulting from the incomplete filling of the zone by circular apertures. DesignCad representations of each of the hybrid design patterns accompanied by optical and SEM micrographs of the fabricated design, and a focused image of the $100\mu\text{m}$ aperture are shown in Figures 4-18 through 20.

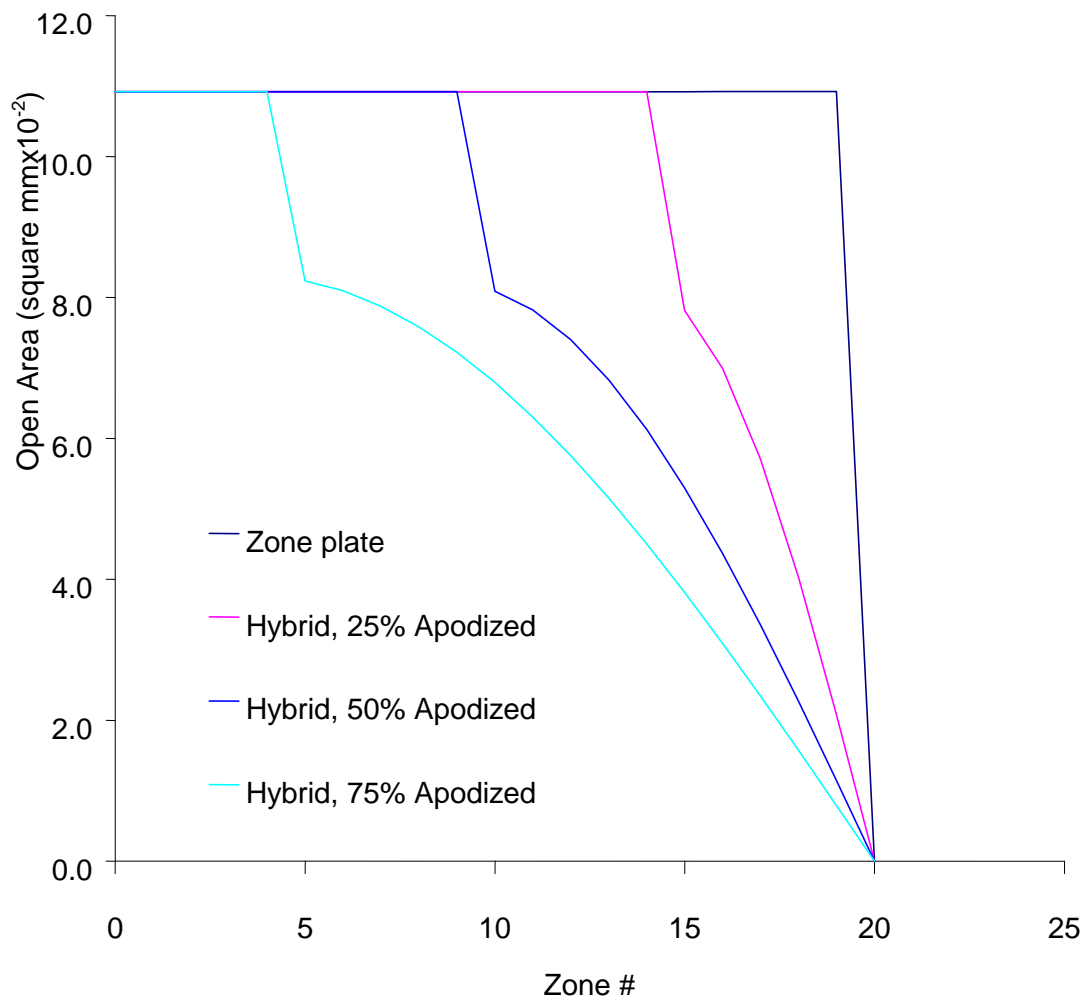


Figure 4-16. Calculated area versus zone number for hybrid photon sieves with circular apertures and different degrees of apodization.

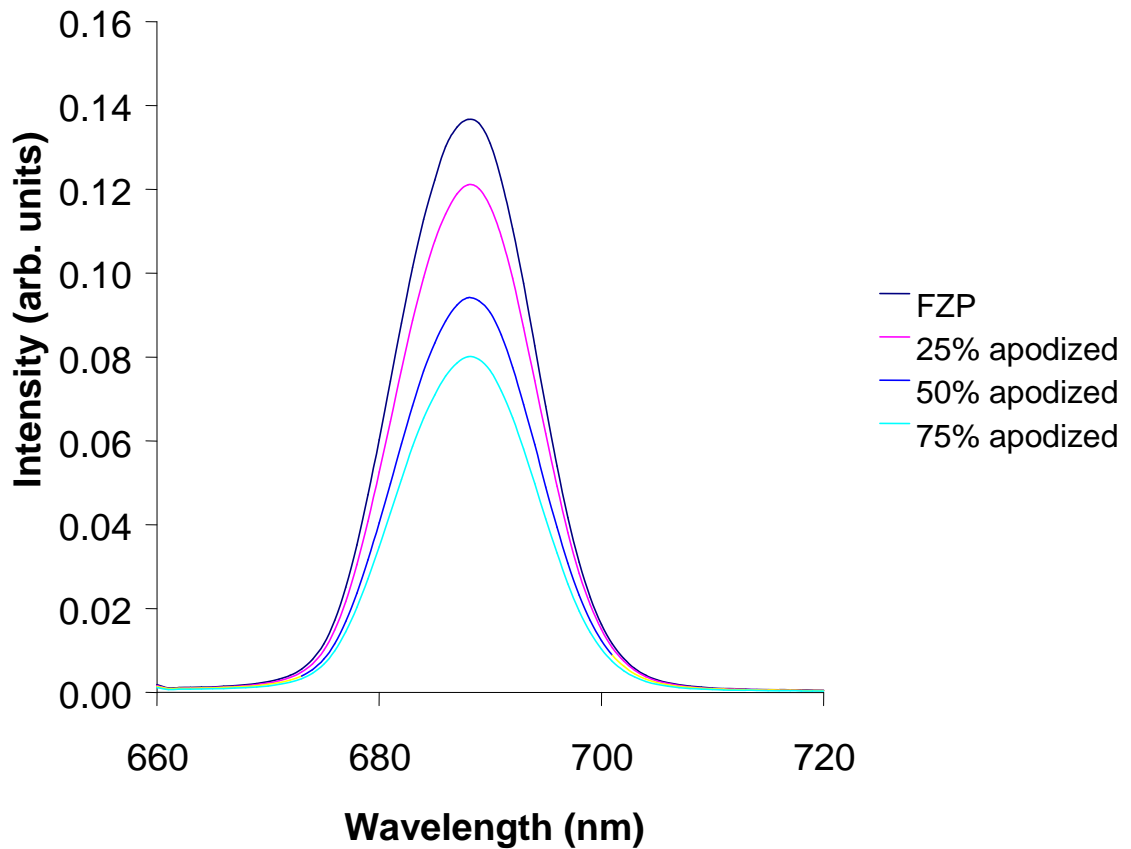
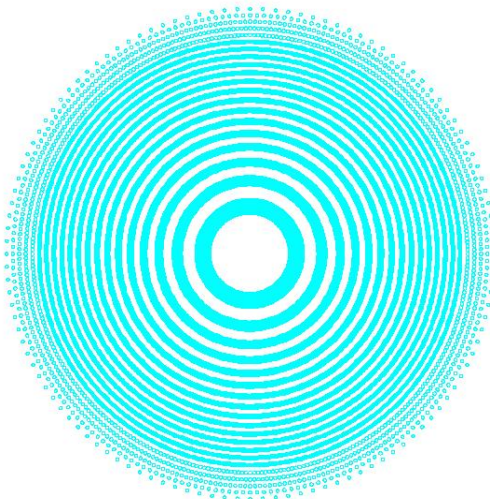
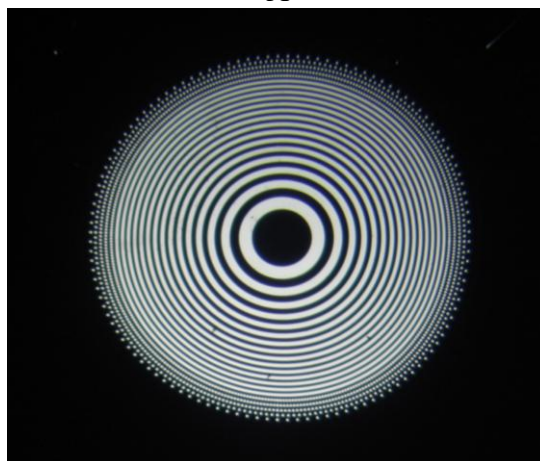


Figure 4-17. Measured transmission for the FZP and the 25%, 50%, and 75% apodized hybrid photon sieve with circular apertures.

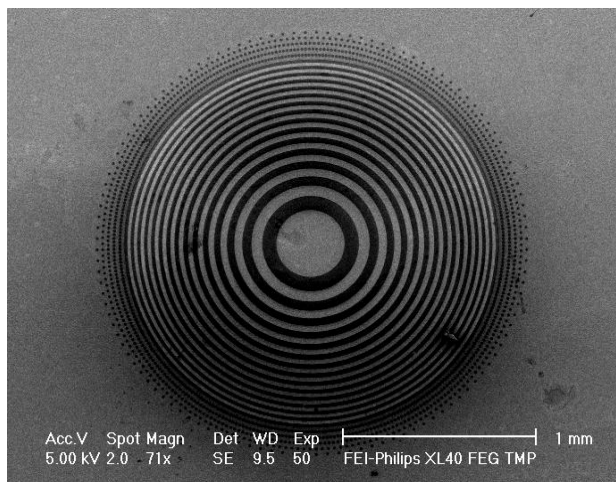
The fabricated lenses match the DesignCad drawing and analysis of the focused images are reported below. The full width half maxima (FWHM) of the first order peak in the intensity distribution for hybrid designs and the zone plate are shown in Figure 4-21. As in the case of normal PS designs, there is a trend towards smaller FWHMs as the degree of apodization increases, and the error bars suggest that the decrease is larger than the possible error. The intensities of the first order peak for the hybrid designs are shown in Figure 4-22, and the 50% and 75 % apodized intensities are 91% and 73% of the 25% lens' intensity.



A

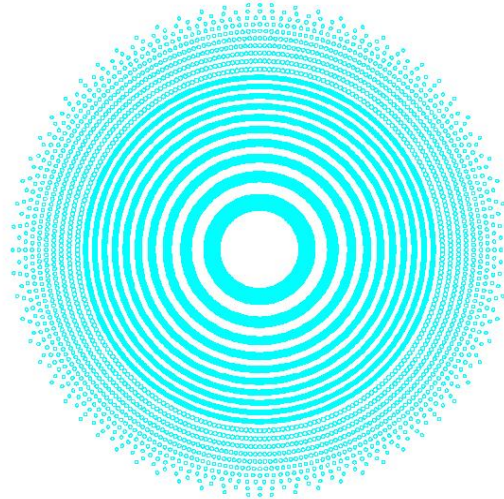


B

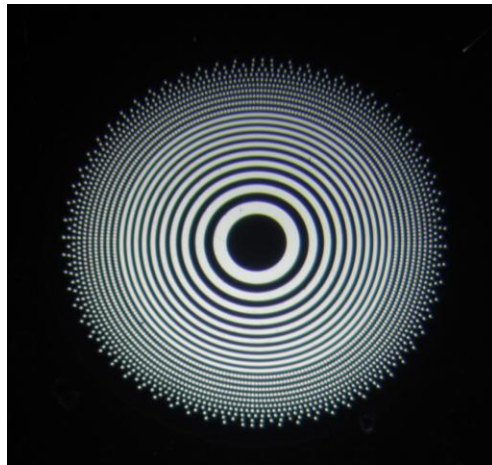


C

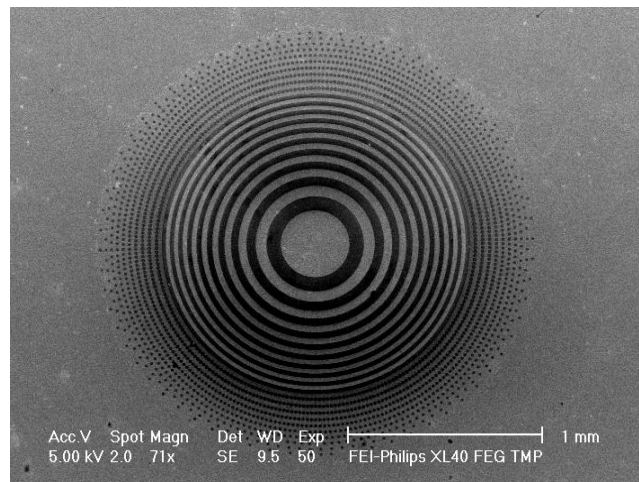
Figure 4-18. 25% apodized hybrid photon sieve with circular apertures. A) DesignCad image of PS. B) Optical micrograph of fabricated PS. C) SEM micrograph of fabricated PS.



A

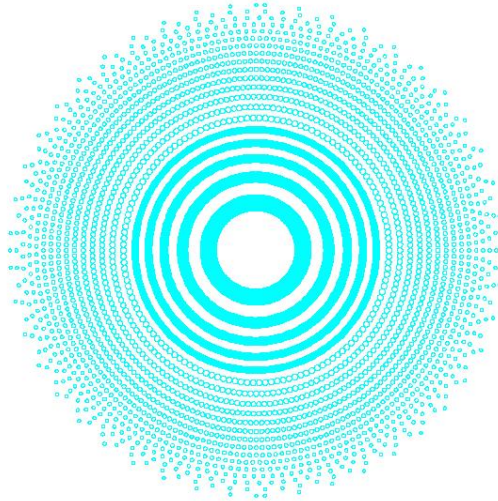


B

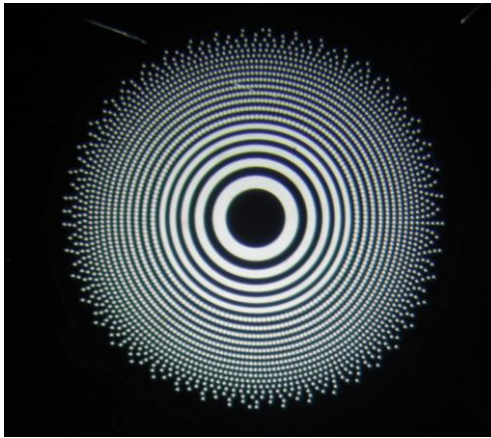


C

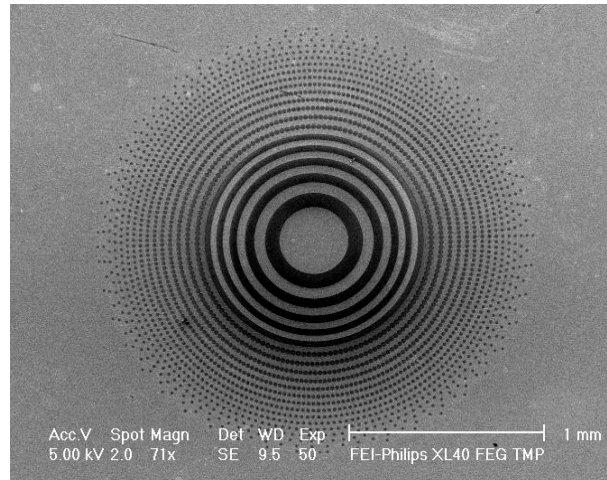
Figure 4-19. 50% apodized hybrid photon sieve with circular apertures. A) DesignCad image of PS. B) Optical micrograph of fabricated PS. C) SEM micrograph of fabricated PS.



A



B



C

Figure 4-20. 75% apodized hybrid photon sieve with circular apertures. A) DesignCad image of PS. B) Optical micrograph of fabricated PS. C) SEM micrograph of fabricated PS.

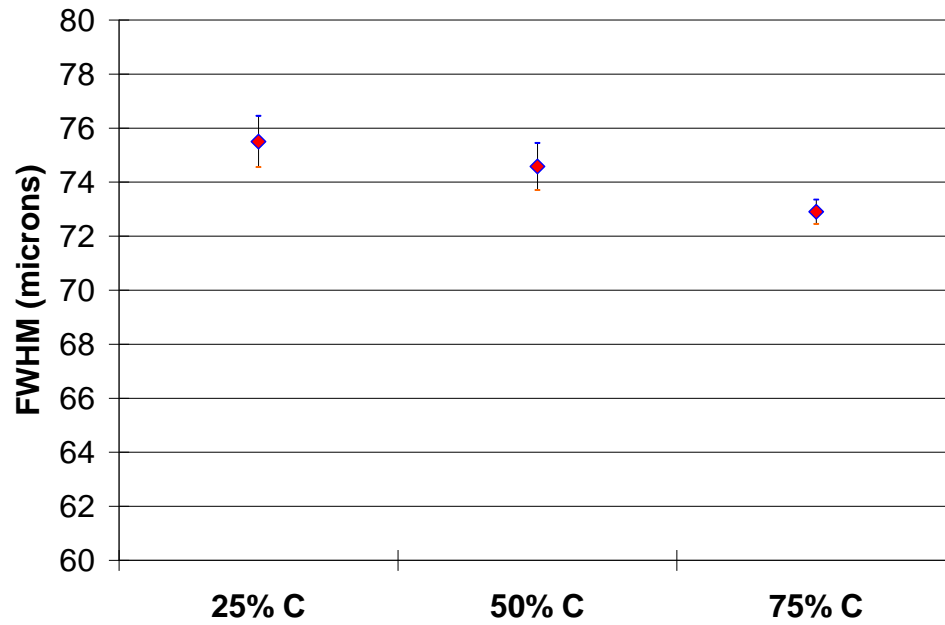


Figure 4-21. Measured FWHM of peak intensity. FWHM for the hybrid designs with circular apertures with 25%, 50%, and 75% of their area apodized.

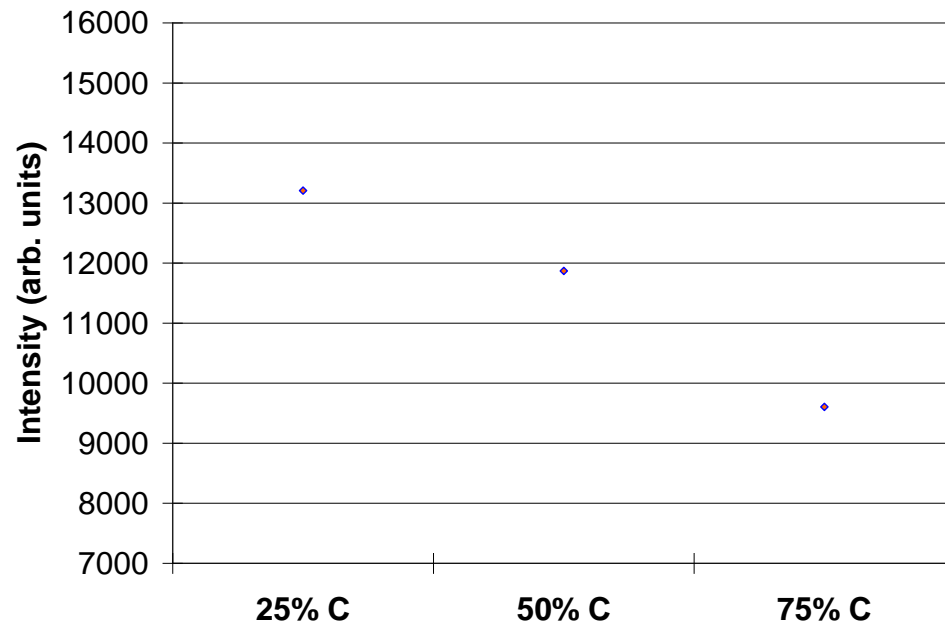


Figure 4-22. Measured peak intensities for the hybrid designs with circular apertures with 25%, 50%, and 75% of their area apodized

4.3.3 Segmented Zones

Based on the designs for the hybrid photon sieve patterns, it is evident that the transmission would be higher if apertures were used that more completely filled the zones, i.e. if the apertures were non circular. As discussed in Section 4.2.1, the maximal filling of unapodized zones is determined by two limiting factors. The first factor is the limitation imposed by the maximum allowable pattern density for electron beam lithography, which cannot be circumvented. However, the second factor is the choice of the appropriate aperture shapes which could not only increase the fraction of the open zone used by the apertures, but could also be used to reduce or eliminate the discontinuity in the transmission window shown in Figure 4-16. An example of a maximally filled zone when using circular apertures is shown in Figure 4-23, where the area inside the circles is open and transmitting, but the roughly triangular areas defined by two adjacent circles and the inner or outer zone boundaries are opaque areas and are non-transmitting.

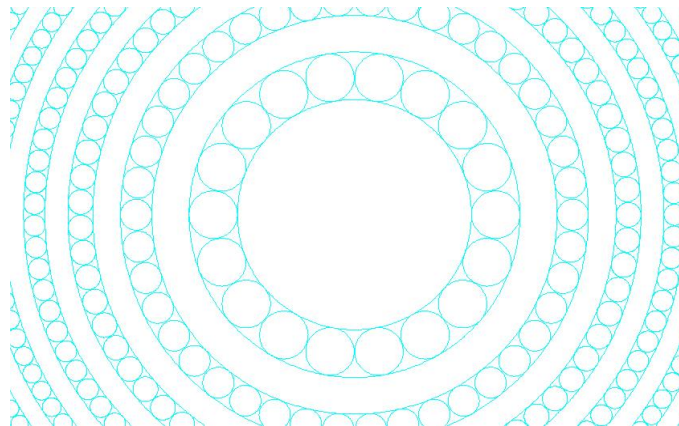


Figure 4-23. Maximally filled zone using circular apertures

Using an aperture shaped to correspond to segments (i.e. conform to the shape) of the zone would result in a more complete use of the available transmitting area, as shown in Figure 4-24.

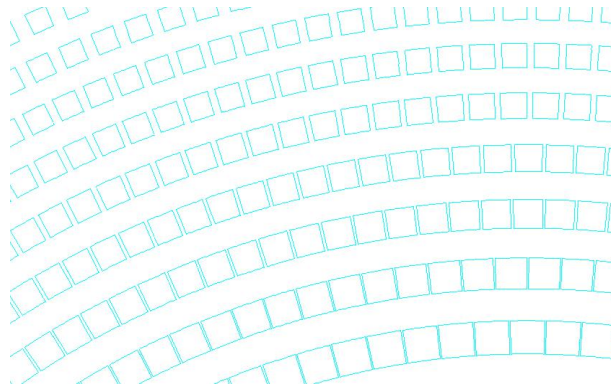


Figure 4-24. Optimized transmitting area of the zone using segments of the zone as apertures.

Although upon cursory inspection, the apertures shown in Figure 2-24 would seem to be square, they are actually segments of the zone they inhabit. The edges of the aperture that coincide with the inner and outer boundaries of the zone are curved to conform to the curvature of the zone. As a result the edges of the apertures that coincide with the inner limit of the zone are slightly shorter than the edges of the apertures that coincide with the outer limit of the zone. This is shown in a magnified view of the pattern shown in Figure 4-25.

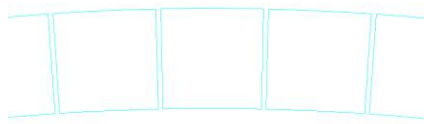


Figure 4-25. Magnified view of segmented apertures filling a zone

To allow direct comparison with the photon sieve designs that used circular apertures, the aspect ratio of the apertures was initially limited to unity. The aspect ratio is defined as the ratio of the two extents of the aperture. These two extents are defined as the circumferential distance through the center of the zone that was enclosed by the

segment, and the length of the intercept of a radial line between the inner and outer boundaries of the segment. The two extents are shown in Figure 4-26 as the lines AB and CD, respectively.

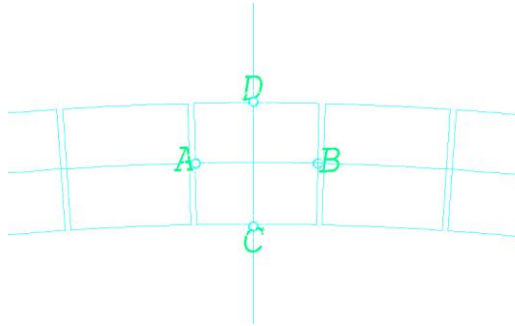


Figure 4-26. Defining the aspect ratio of an aperture.

The aspect ratio, AR, of the aperture is therefore defined by Equation 4-2 as

$$AR = \frac{AB}{CD} \quad 4-2$$

To allow direct comparison to the hybrid photon sieve patterns designed with circular apertures, three hybrid photon sieve patterns with segmented apertures were designed and fabricated. Comparisons of the total transmitting area of the patterns with circular apertures and zone segment apertures are tabulated in Table 4-4.

Using segmented apertures resulted in a 4% increase (from 1.90 to 1.98mm²) in total transmitting area for the 25% apodized design, a 9% increase (from 1.62 to 1.76mm²) in total transmitting area for the 50% apodized design and a 16% increase (from 1.34 to 1.55mm²) in total transmitting area for the 75% apodized design. The calculated distributions of open area versus zone number for each of the designs using zone segment apertures are shown in Figure 4-27. The measured total transmitted intensity increased by 2.0%, 12.9% and 13.4% for segmented versus circular apertures and 25%, 50%, and 75% apodization, respectively.

Table 4-4. Comparison of total open areas of hybrid photon sieve designs with circular versus segmented apertures.

Pattern	Open Area(mm ²)	Percent of zone plate area
Zone Plate	2.18	100
25% Apodized w/segmented	1.98	90.5
25% Apodized w/circular	1.90	87.2
50% Apodized w/segmented	1.76	80.7
50% Apodized w/circular	1.62	74.1
75% Apodized w/segmented	1.55	71.1
75% Apodized w/circular	1.34	61.2

Comparison of the distribution of open area of the hybrid photon sieve designs with circular apertures, shown in Figure 4-16, to the distribution of open area for the hybrid photon sieve designs using segmented zone apertures with an aspect ratio of 1, shown in Figure 4-28, reveals that the use of the segmented apertures significantly reduces the sharpness of the discontinuity in the transmission window at the transition from completely open zones to apodized zones. DesignCad representations of each of the hybrid designs using segmented zone apertures, SEM and optical micrographs of the fabricated design are shown in Figures 4-29 through 4-31. As for the previous PSs and hybrid PSs, the hybrid PS fabricated with segment apertures match very well with the DesignCad images.

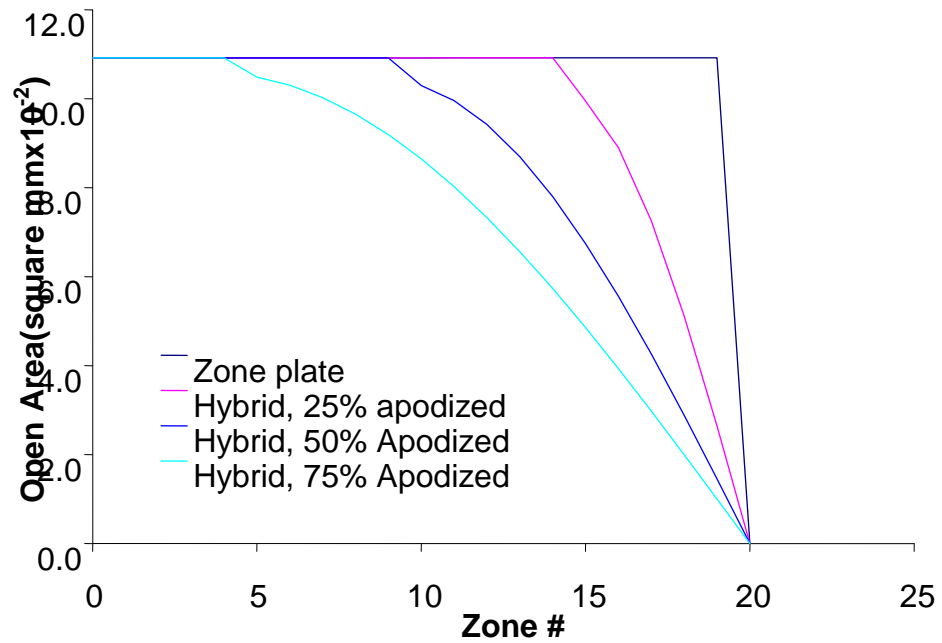


Figure 4-27. Calculated area distributions of hybrid photon sieve designs with segmented zone apertures

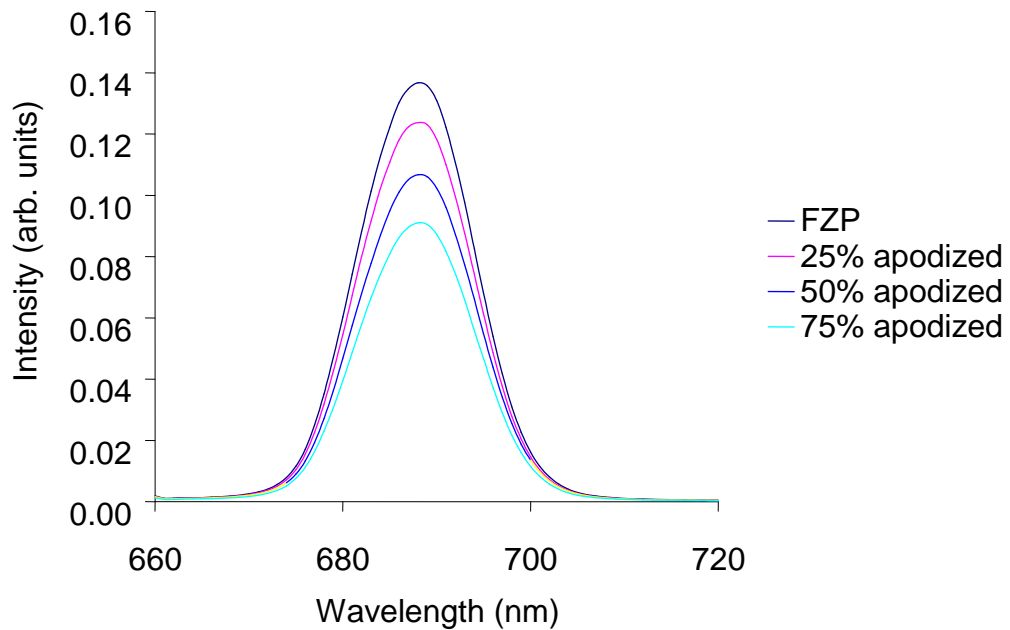
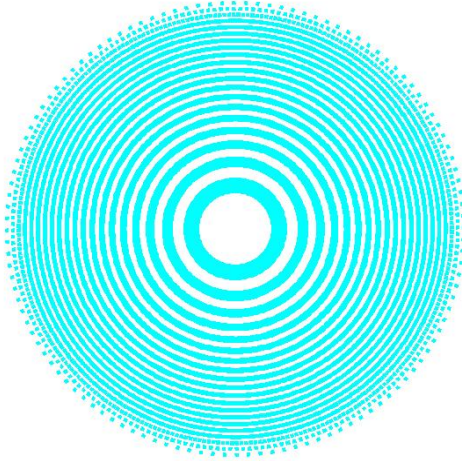
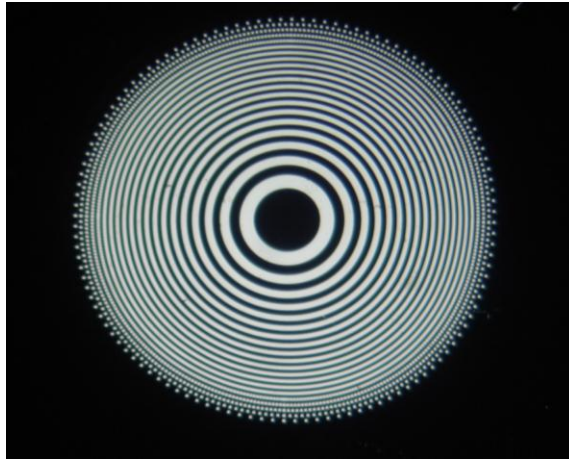


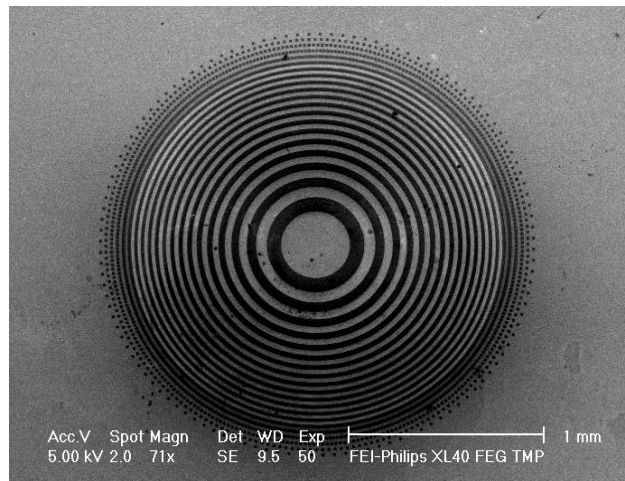
Figure 4-28. Measured transmission of Fresnel zone plate (FZP) and 25%, 50%, and 75% apodized photon sieve designs with segmented zone apertures with AR=1.



A

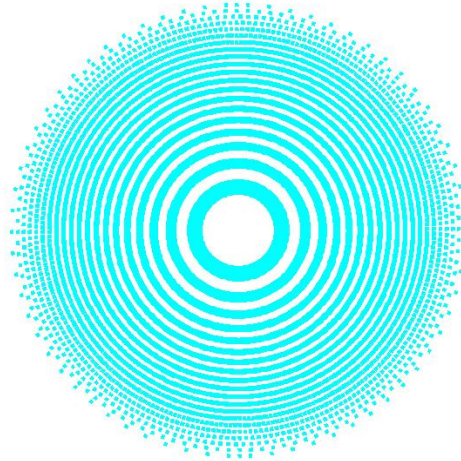


B

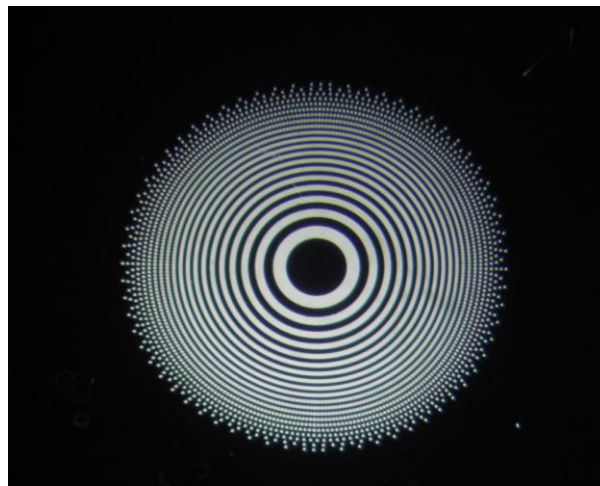


C

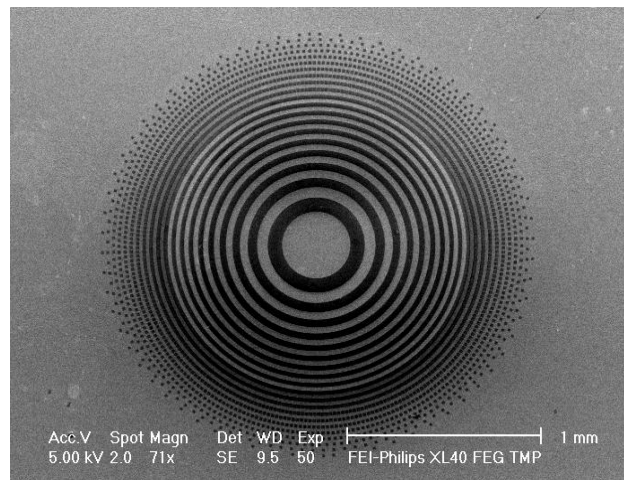
Figure 4-29. 25% apodized hybrid photon sieve incorporating segmented zone apertures with AR=1. A) DesignCad image of PS. B) Optical micrograph of fabricated PS. C) SEM micrograph of fabricated PS.



A

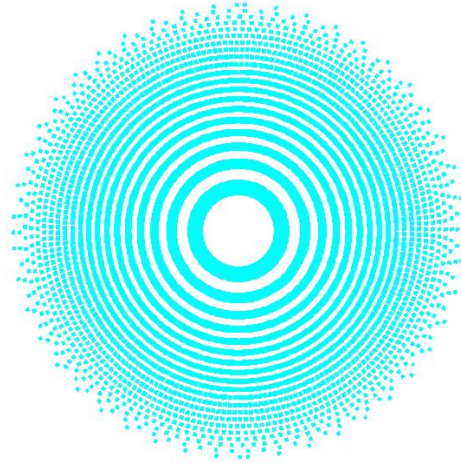


B

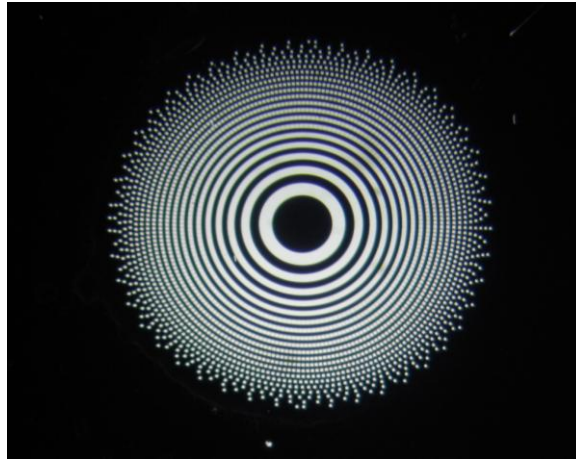


C

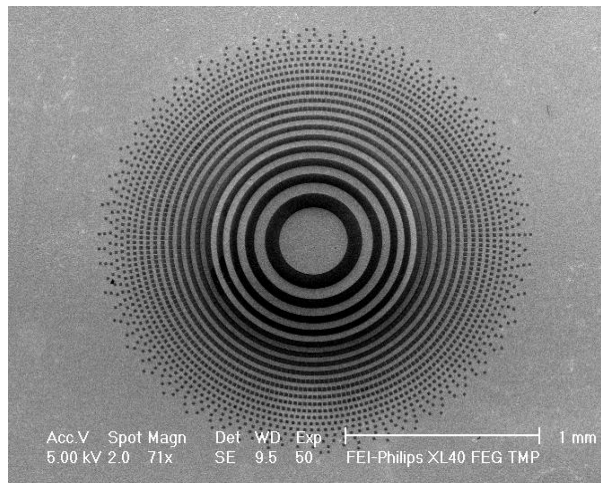
Figure 4-30. 50% apodized hybrid photon sieve incorporating segmented zone apertures with AR=1. A) DesignCad image of PS. B) Optical micrograph of fabricated PS.C) SEM micrograph of fabricated PS.



A



B



C

Figure 4-31. 75% apodized hybrid photon sieve incorporating segmented zone apertures with AR=1. A) DesignCad image of PS. B) Optical micrograph of fabricated PS. C) SEM micrograph of fabricated PS.

The full width half maxima (FWHM) of the first order peak in the intensity distribution of the transmitted light for hybrid lens designs with segmented zone apertures are shown in Figure 4-32. As in both previous designs, the FWHM trends smaller as the degree of apodization is increased, but the magnitude of the changes are within the error bars.

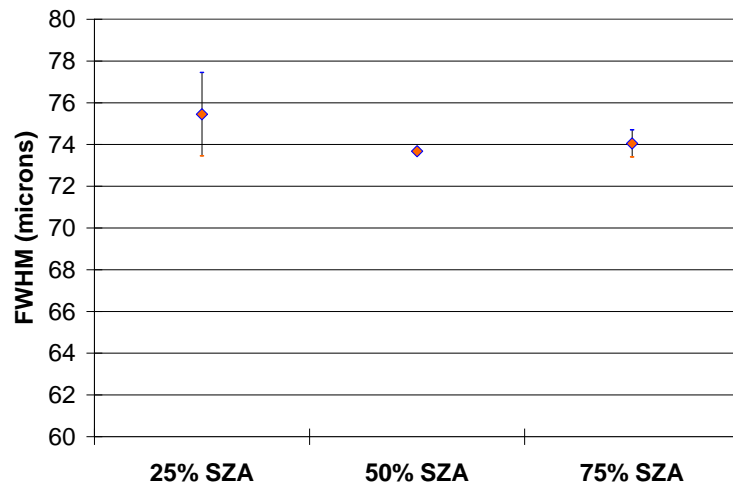


Figure 4-32. Measured FWHM of peak intensity for hybrid designs with segmented zone apertures (SZA) with AR=1.

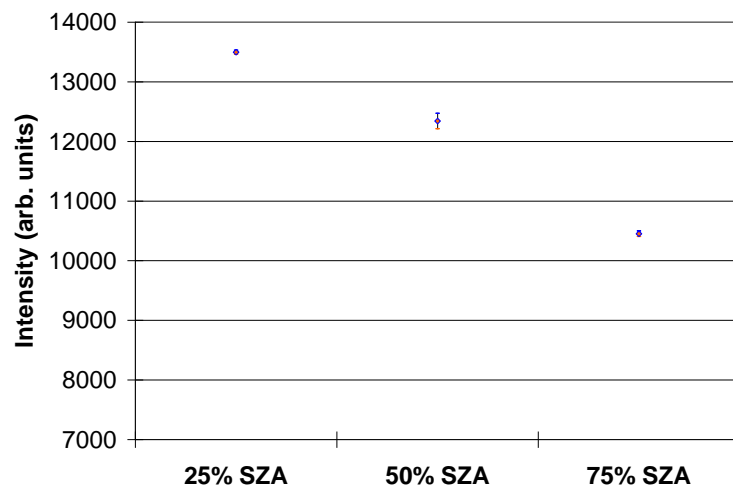


Figure 4-33. Measured peak intensity for hybrid designs with segmented zone apertures (SZA) with AR=1.

The intensities of the first order peak for the hybrid designs with segmented zone apertures are shown in Figure 4-33. The intensity at the focal point is reduced 20% as the degree of apodization in increase from 25 to 75%.

4.3.4 Large Aspect Ratio Zone Segments Lenses

Some small additional increases in the transmitting area can be realized by using large aspect ratio ($AR > 1$) zone segments as apertures. Because the limitations imposed by the lithography system dictate that there be some minimum distance between each pattern element, a zone filled with large numbers of low aspect ratio apertures (e.g. $AR \leq 1$) will have a larger fraction of non-transmitting area because of the required minimum separation distance (set at 500nm in the present case) between each aperture.

Conversely, a zone filled with fewer apertures of larger aspect ratio will have a smaller fraction of non-transmitting area. It was also expected that the small improvement in use of available transmitting area of each zone would be sufficient to further reduce the remaining small discontinuity in the transmission window (Figure 4-27). Area distributions of 75% apodized hybrid with segmented zone apertures of aspect ratios varying from 0.25 to 4 are shown in Figure 4-34. Designs with aspect ratios of less than one incorporated larger numbers of apertures in each zone and as a result of the minimum separation between apertures, suffered from a lower transmitting area, as tabulated in Table 4-5. A low AR also led to an increase in the size and sharpness of the discontinuity in the transmission window at the transition from the completely open zones to apodized zones. On the other hand, designs incorporating apertures with an aspect ratio larger than one showed a slight increase in total calculated open area and elimination of the discontinuity at the transition between completely open unapodized zones and apodized zones. The measured transmission confirms a slight increase (5%) in intensity as the

aspect ratio of the segmented zone aperture is increased from 2 to 4.

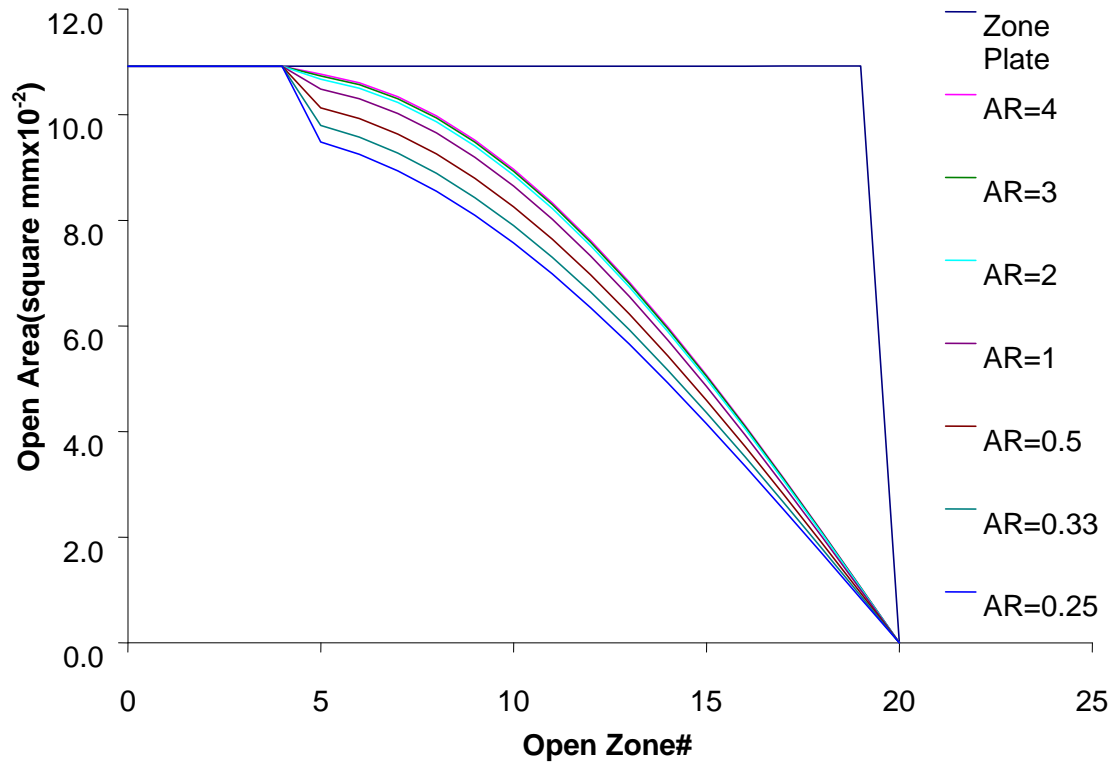


Figure 4-34. Calculated area distributions for hybrid 75% apodized photon sieves with segmented apertures of various aspect ratios (AR)

Table 4-5. Calculated open area of hybrid photon sieves w/segmented zone apertures

Pattern	Open Area(μm^2)	Percent of zone plate area
Zone Plate	2.18	100
75% Apodized, AR=0.25	1.43	65.5
75% Apodized, AR=0.33	1.47	67.2
75% Apodized, AR=0.50	1.51	69.1
75% Apodized, AR=1	1.55	71.1
75% Apodized, AR=2	1.58	72.2
75% Apodized, AR=3	1.59	72.6
75% Apodized, AR=4	1.59	72.8

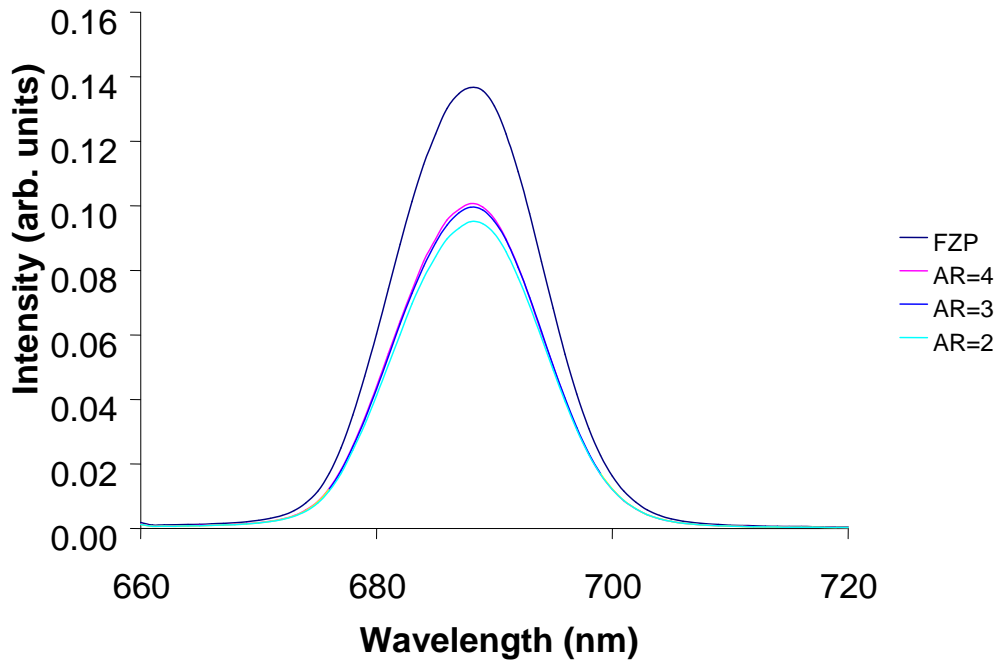
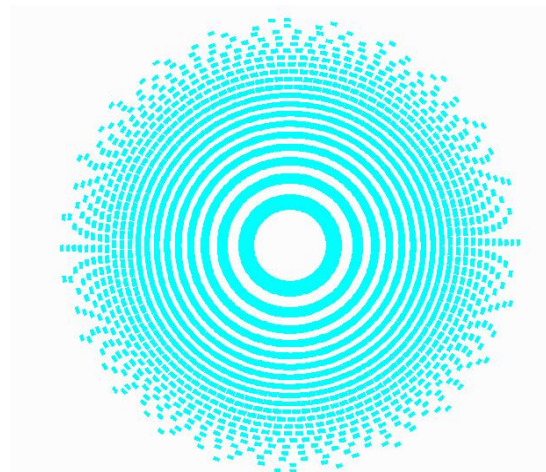
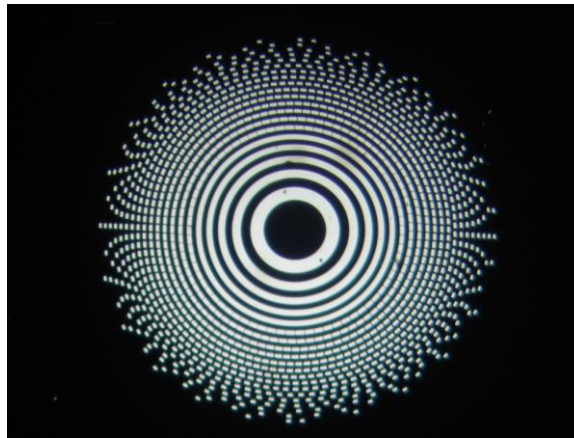


Figure 4-35. Measured transmission for Fresnel zone plate (FZP), and 75% apodized hybrid photon sieves with segmented zone apertures of aspect ratio 4 (AR=4), 3 (AR=3) and 2 (AR=2).

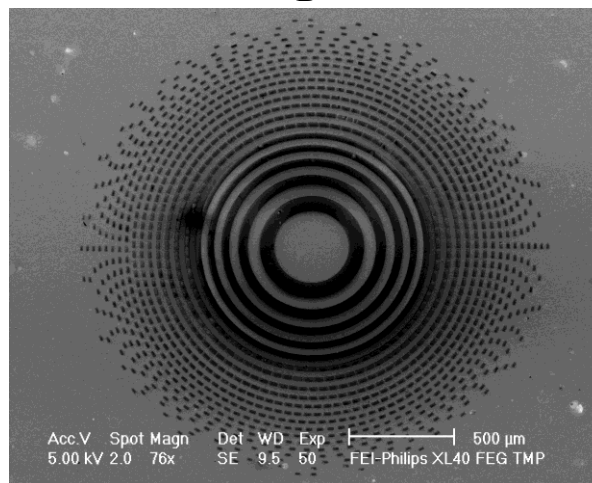
DesignCad representations of the designs, accompanied by optical and SEM micrographs of the fabricated designs incorporating apertures with an aspect ratio larger than one, are shown in Figures 4-36 through 4-38. The optical and SEM micrographs show that the designs have been successfully fabricated. The full width half maxima (FWHM) of the first order peak in the diffraction pattern for hybrid designs with large aspect ratio segmented zone apertures are shown in Figure 4-39 and the transmitted intensities for the hybrid designs with larger aspect ratio segmented zone apertures are shown in Figure 4-40. The data in Figure 4-39 show that the FWHM decreased from $73.5\mu\text{m}$ to $70.6\mu\text{m}$ for ARs of 2 and 4, respectively, with error bars $< \pm 0.3\mu\text{m}$. The measured peak intensity at the focal point increases slightly (9.5%) as the aspect ratio is increase from 2 to 4.



A

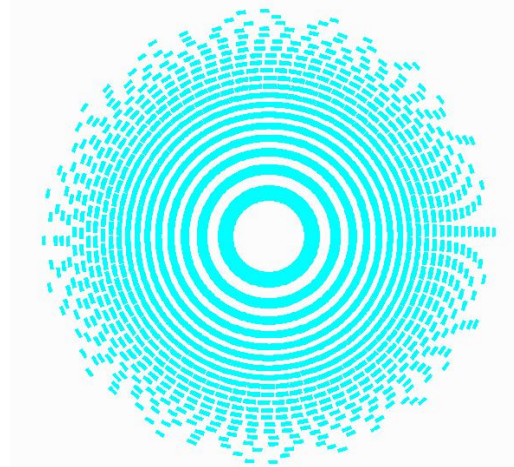


B

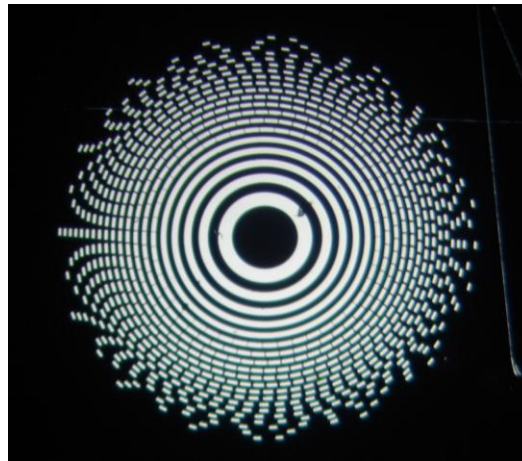


C

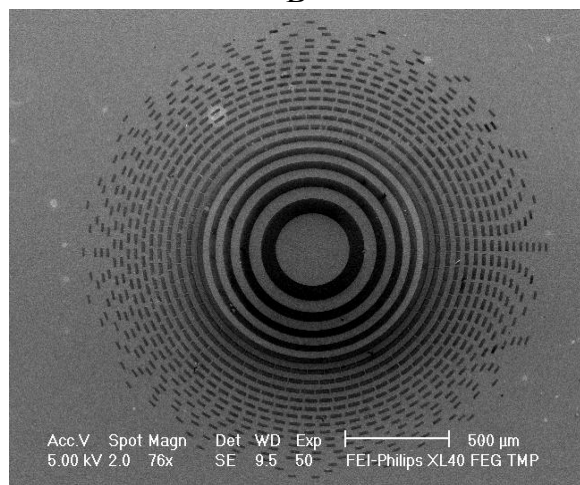
Figure 4-36. 75% apodized hybrid photon sieve incorporating segmented zone apertures with $AR=2$. A) DesignCad image of PS. B) Optical micrograph of fabricated PS. C) SEM micrograph of fabricated PS.



A

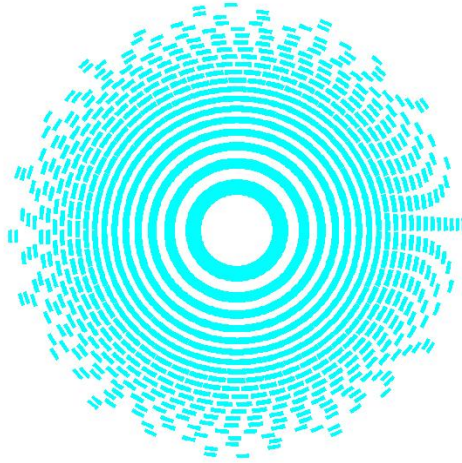


B

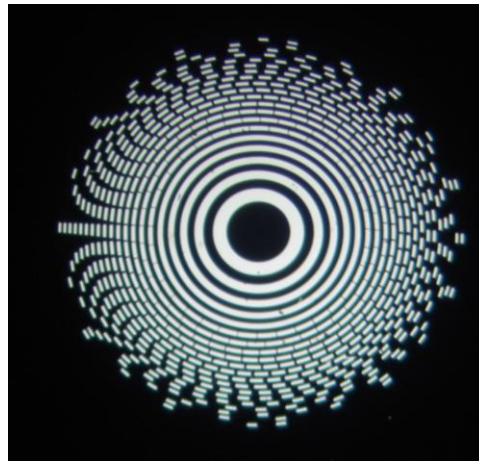


C

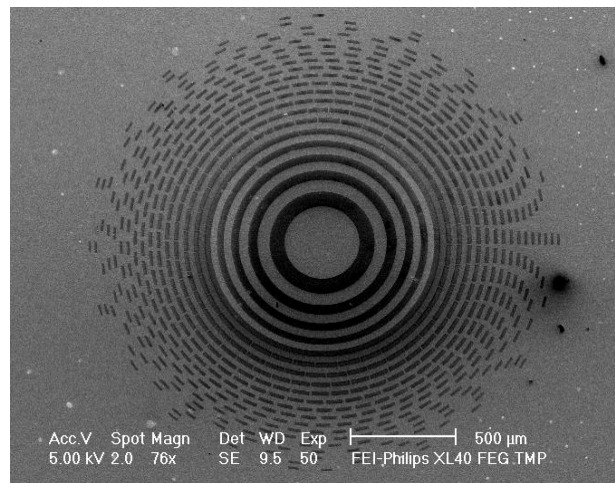
Figure 4-37. 75% apodized hybrid photon sieve incorporating segmented zone apertures with AR=3. A) DesignCad image of PS. B) Optical micrograph of fabricated PS. C) SEM micrograph of fabricated PS.



A



B



C

Figure 4-38. 75% apodized hybrid photon sieve incorporating segmented zone apertures with AR=4. A) DesignCad image of PS. B) Optical micrograph of fabricated PS. C) SEM micrograph of fabricated PS.

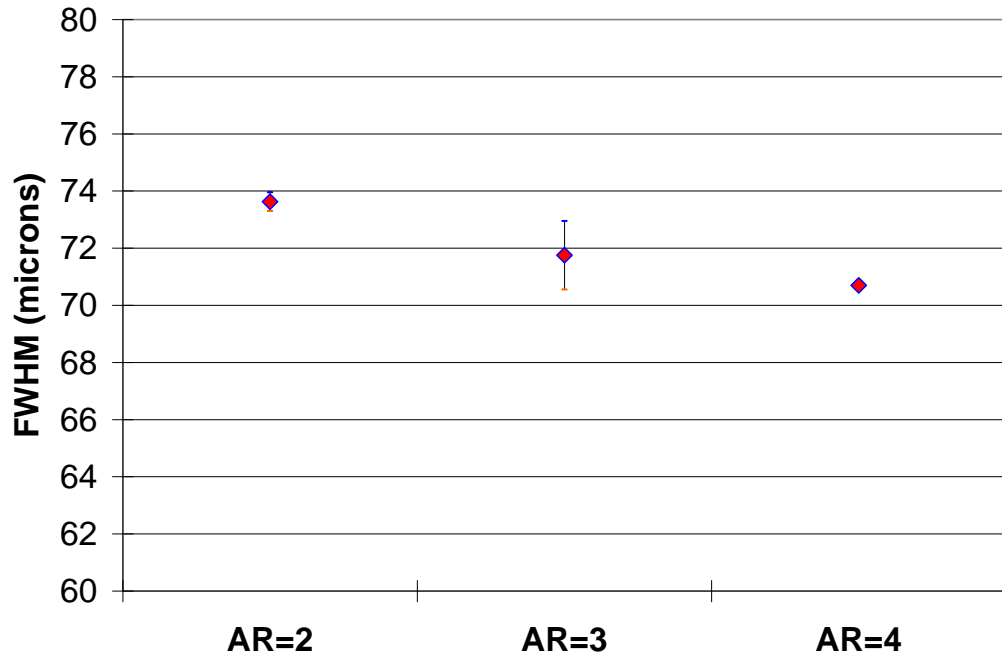


Figure 4-39. Measured FWHM of peak intensity for hybrid designs with large aspect ratio segmented zone apertures

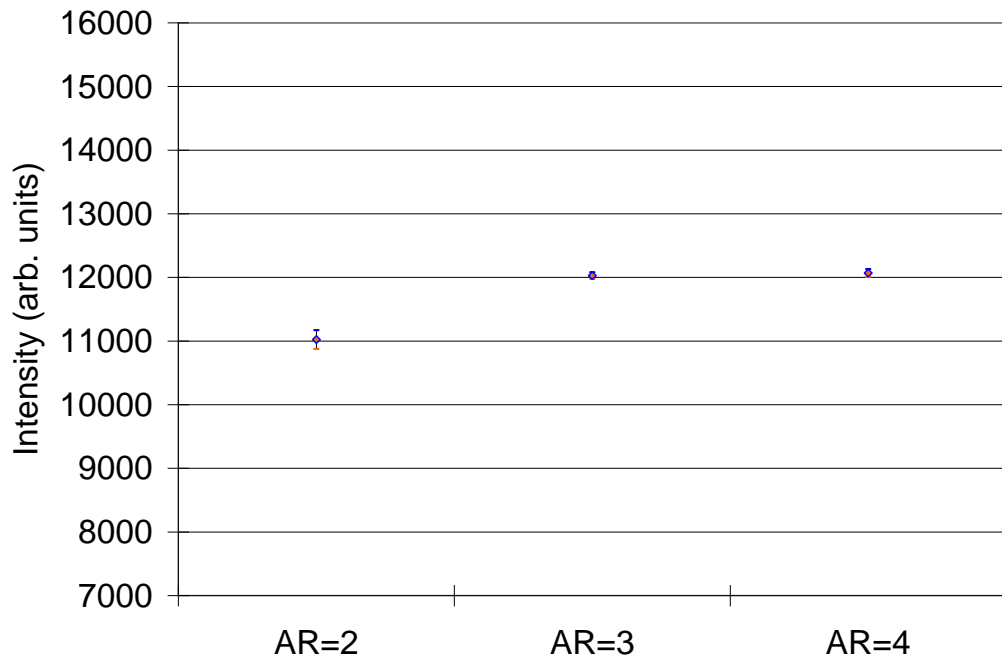


Figure 4-40. Measured peak intensity for hybrid designs with large aspect ratio segmented zone apertures.

4.4 Results and Discussion

The measured focal lengths of all the lens designs (Table 4.6) were within $\pm 2.2\%$ of the design focal length of 50mm. The discrepancy between the design and measured focal lengths can be attributed to a combination of several factors. First, the calculated focal length from the design assumes that the incident wavelength is 700nm; however, the measured spectrum of the incident light transmitted by the narrow bandpass filter shows that the peak transmission actually occurs at 688nm (Figure 4-2). When this difference between design and actual experimental wavelength is taken into account, the experimentally measured focal lengths all fall within $\pm 1.3\%$ of the expected focal length. Other factors contributing to the discrepancy between calculated and measured focal length include the assumption that the incident wavefront is planar. The experimental setup deviates from this ideal situation since the incident wavefront is actually slightly spherical because it originated from a point source that was situated at a finite rather than an infinite distance. Additionally, the calculated focal length from the design does not account for refraction by the glass substrate. The calculated focal length assumes an ideal situation in which the indices of refraction of the media on both sides of the photon sieve are the same. However, one interface of the photon sieve is with air ($n=1$) and the other interface is with glass ($n=1.5$). Light incident on the glass would be refracted, shifting the focal length to a slightly shorter distance. All of these factors may have played a role in generating the small discrepancy between the calculated focal lengths and the measured focal lengths. The measured focal lengths for all of the photon sieve designs are shown in Table 4-6.

Table 4-6. Measured focal lengths vs. Lens design (all units are given in mm unless indicated otherwise)

Designs	Image distance	Object distance	Focal Length	Percent difference from Design(700nm)	Percent difference from Design(688nm)
Fresnel zone plate	103.5	100.0	50.8	0.3	-0.6
Unapodized Photon sieve	105.5	100.0	51.3	1.3	0.4
25% Apodized photon sieve	104.5	100.0	51.1	0.8	-0.1
50% Apodized photon sieve	104.5	100.0	51.1	0.8	-0.1
75% apodized photon sieve	105.5	100.0	51.3	1.3	0.4
25% Apodized hybrid with circular apertures	106.5	100.0	51.6	1.7	0.8
50% Apodized hybrid with circular apertures	106.5	100.0	51.6	1.7	0.8
75% Apodized hybrid with circular apertures	105.5	100.0	51.3	1.3	0.4
25% Apodized hybrid with segmented zone apertures	106.5	100.0	51.6	1.7	0.8
50% Apodized hybrid with segmented zone apertures	106.5	100.0	51.6	1.7	0.8

Table 4-6. Continued

Designs	Image distance	Object distance	Focal Length	Percent difference from Design(700nm)	Percent difference from Design(688nm)
75% Apodized hybrid with segmented zone apertures	107.5	100.0	51.8	2.2	1.3
75% Apodized hybrid with segmented zone apertures, AR=2	103.5	100.0	50.8	0.3	-0.6
75% Apodized hybrid with segmented zone apertures, AR=3	102.5	100.0	50.6	-0.2	-1.1
75% Apodized hybrid with segmented zone apertures, AR=4	102.5	100.0	50.6	-0.2	-1.1

The measured transmission of the each of the photon sieve designs (Table 4-2 through 4-5) show that the transmission decreased when the transmitting area was reduced by apodization. This can be seen in Figure 4-8, which shows the transmission of the traditional photon sieve designs decreasing from 67% to 56% of the FZP's transmission as the degree of apodization was increase from 25% to 75%. Similarly, Figure 4-17 shows the measured transmission of the hybrid photon sieve designs with circular apertures decreasing from 88% to 59% of the FZP's transmission as the degree of apodization was increased from 25% to 75%, but the transmission was from 5% for the

25% apodized to 32% for the 75% apodized, higher than the traditional PS design. Figure 4-28 shows the measured transmission of the hybrid photon sieve designs with segmented zone apertures with an aspect ratio of 1 and Figure 4-35 shows the measured transmission for hybrid photon sieve designs with large aspect ratio (AR of 2-4) segmented apertures, and the transmissions decrease from 90% to 66% of FZP transmission as the degree of apodization is increase from 25% to 75%. As pointed out above, the measured transmissions confirmed the calculated increase in transmission from fully open zones in the hybrid photon sieve designs or by use of segmented zone apertures (Figures 4-41 through 4-43 which compare the transmission of 25%, 50% and 75% apodized designs, respectively). All of the large aspect ratio design were 75% apodized and are included in Figure 4-43 for comparison to the other 75% apodized designs

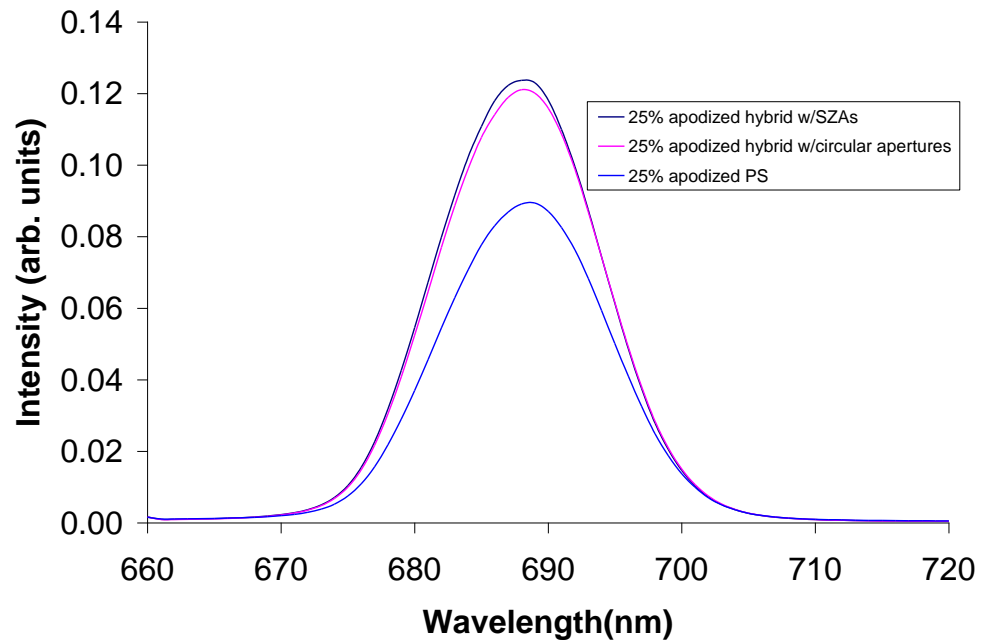


Figure 4-41. Measured transmission for the 25% apodized designs

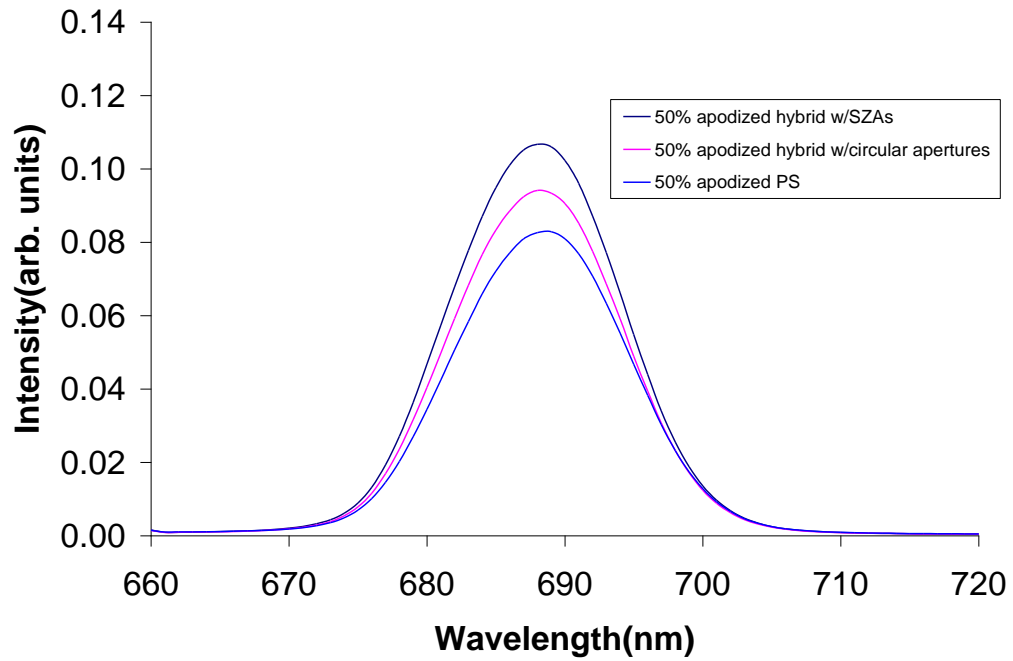


Figure 4-42. Measured transmission for the 50% apodized designs

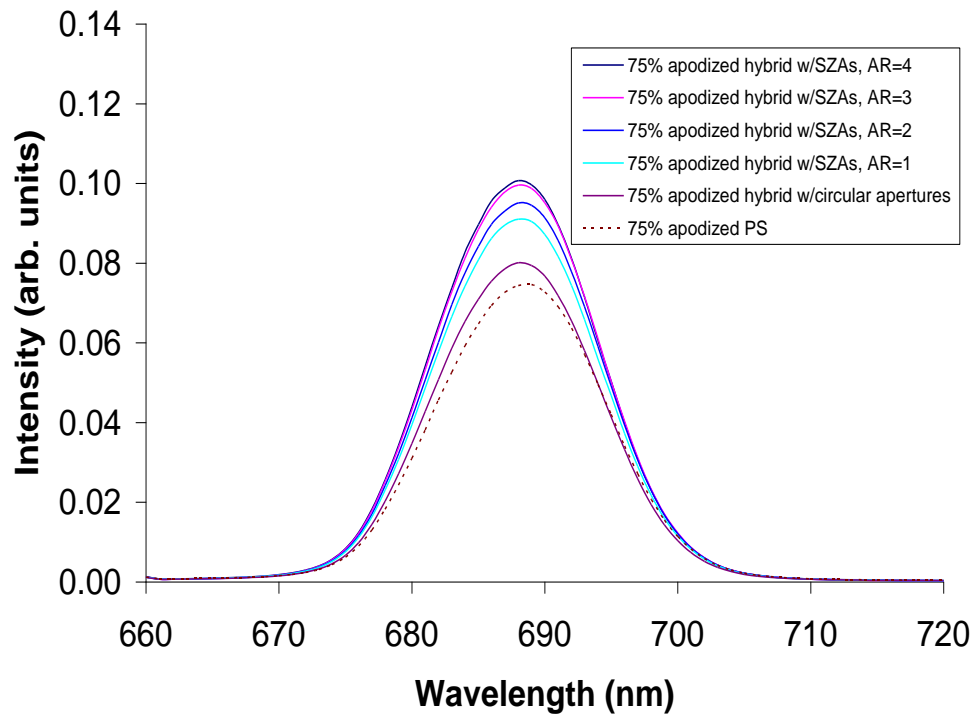


Figure 4-43. Measured transmission for the 75% apodized designs

Numerically integrating the measured transmission vs. wavelength and representing the total transmission of each design as a fraction of the total transmission of a 2.4mm diameter aperture allows a comparison with the calculated open area of the various fabricated designs. Shown in Table 4-7 are the results of using the trapezoid rule to numerically integrate the measured transmission. The integrated areas under the measured transmission curves represent the total transmission and are compared with the total calculated open area of the fabricated designs. The relative measured transmission corresponds closely to the calculated relative open area with none more than $\pm 4.6\%$ and 84% of the designs varying $\pm 2.4\%$ or less, indicating that the fabrication of the photon sieves with larger open areas has produced brighter images of the source aperture without a loss of FWHM resolution. In Table 4-7, FZP refers to Fresnel Zone Plate, PS, refers to Photon Sieve SZ refers to hybrid photon sieves with Segmented Zone apertures, and C refers to hybrid photon sieve with circular apertures.

Table 4-7. Measured transmission and calculated open area for different designs and FZP

Design	Measured Transmission (arb. units)	Measured Percent transmission	Calculated Percent of open area
3mm Aperture	4.484	100.0	100
FZP	2.094	46.7	48.19
0% PS	1.600	42.2	43.77
25% SZ	1.892	41.4	42.00
25% C	1.854	31.4	33.16
25% PS	1.408	35.7	36.25
50% SZ	1.644	36.7	38.90
50% C	1.455	32.4	35.81
50% PS	1.309	29.2	30.06
75% SZ	1.399	31.2	34.26

Table 4-7. continued

Design	Measured Transmission (arb. units)	Measured Percent transmission	Calculated Percent of open area
75% C	1.234	27.5	29.62
75% PS	1.174	26.2	26.75
AR=2	1.461	32.6	34.26
AR=3	1.522	33.9	34.93
AR=4	1.535	34.2	35.15

The peak intensity at the focal point, measured using the Dataray beam profiler setup, as discussed in Section 4.2.1 and shown in Figure 4-3, are consistent with the trends in the measured transmission. The measured peak intensities at the focal point of all of the designs are shown together in Figure 4-44. The designs with larger calculated transmitting area, had a higher measured transmission and higher peak intensity at the focal plane. The 25% apodized hybrid design with circular apertures and with segmented zone apertures, respectively, achieved a 38% and 41% increase in measured intensity at the focal point compared to the 25% apodized traditional photon sieve design. The 50% apodized hybrid design with circular apertures and with segmented zone apertures respectively achieved a 30% and 35% increase in measured intensity at the focal point compared to the 50% apodized traditional photon sieve design. Similarly, in a comparison of the measured intensities of the 75% apodized designs, the hybrid designs outperforming the traditional photon sieve design, with the hybrid with segmented zone apertures and circular apertures respectively achieving a 34% and 23% increase relative to the traditional photon sieve. The 75% apodized hybrid designs incorporating large aspect ratio segmented zone apertures also exhibited increased intensity at the focal point

compared to the traditional photon sieve design. The design incorporating segmented zone apertures with the largest aspect ratio, an aspect ratio of 4, showed an increase of 55% compared to the traditional photon sieve design and a 15.5% increase relative to the design with segmented zone aperture of aspect ratio of one. In all cases the secondary maxima was less 1% of the central peak height and therefore not discernable.

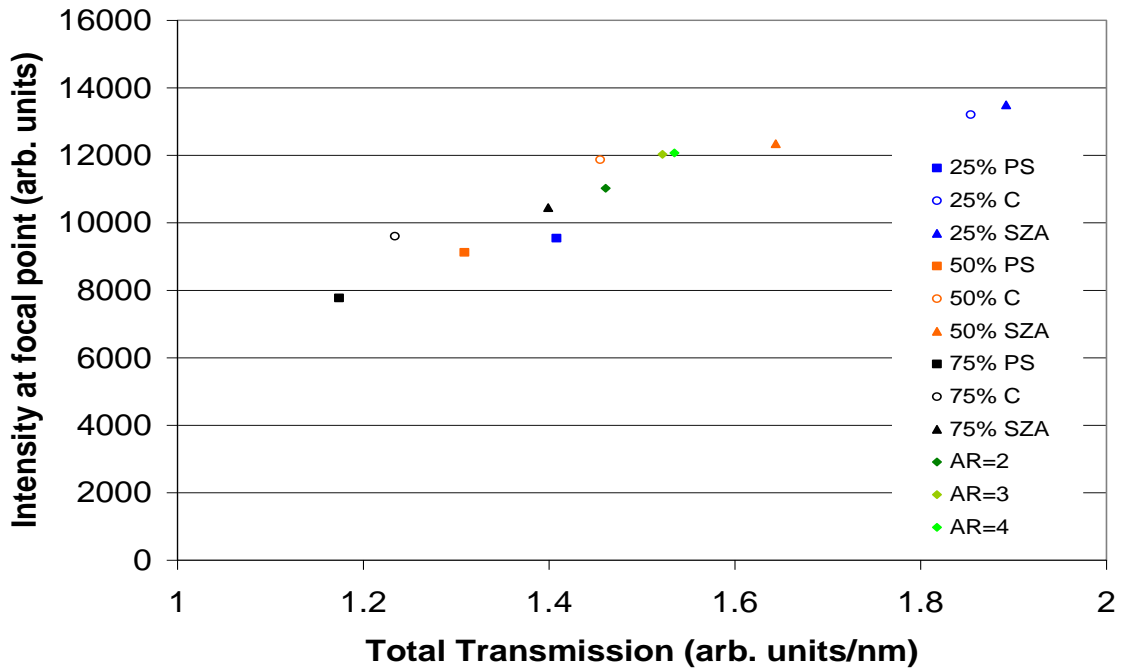


Figure 4-44. Intensity at focal point vs. total transmission for various lens designs

All of the designs exhibited roughly the same resolving power as shown by the resolution test using the aperture pairs and by the measurement of the full width half maximum (FWHM). The measured FWHM in the x direction consistently differed from the FWHM in y direction, with the $FWHM_x$ being, on average, 11% larger than the $FWHM_y$. This probably occurred as a result of the macro used to generate the designs. The macro generated the distribution of apertures in a zone by creating a single aperture and then filling the zone with copies of that initial aperture. Because the macro placed all of the initial apertures for the zone along the same radial line, a symmetrical placement of

the apertures resulted. This is especially discernable in the SEM micrographs of the large aspect ratio segmented aperture designs (Figures 4-36 to 4-39). The reported FWHMs were averages of the FWHM_x and the FWHM_y . This observation and data discussed below are evidence that apodization affects the FWHM and therefore the trends towards smaller FWHM are real. Specifically, the measured FWHMs for all of the designs were $75\mu\text{m}\pm 2.45$ with the exception of the large aspect ratio segmented zone designs which had FWHMs of $72\pm 1.95\ \mu\text{m}$. For all three designs (PS with circular apertures, and Hybrid PS with either circular or SZ apertures) there was consistently a trend to smaller FWHMs at larger degrees of apodization, although the magnitude of change was close to the error limits. There was a systematic decrease in FWHM with increasing aspect ratio for PS with zone segment apertures, from 73.6 ± 0.3 for AR=2 to 70.7 ± 0.2 for AR=4 (Figure 4-48). These trends are consistent with Kipp's¹¹ results, which showed that an apodized photon sieve had a smaller FWHM than a comparable FZP.

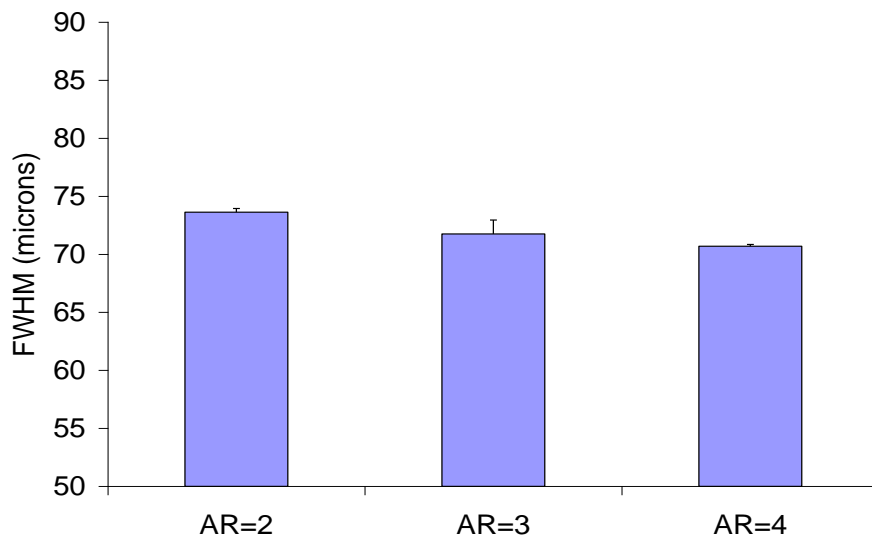


Figure 4-45. Measured FWHM of peak intensity for large aspect ratio segmented zone apertures. Shown are FWHM for segmented zone apertures of aspect ratio 2 (AR=2), 3 (AR=3) and 4 (AR=4).

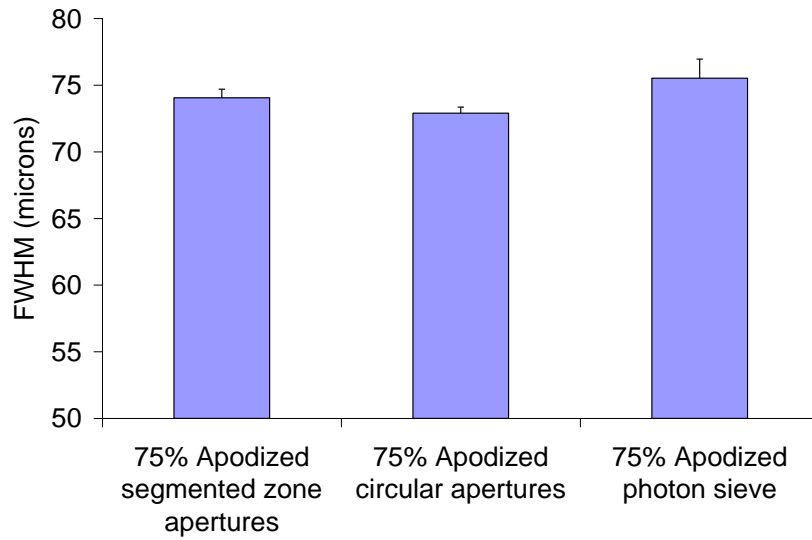


Figure 4-46. Measured FWHM of peak intensity for 75% apodized designs. Shown are FWHM for 75% apodized hybrid designs with segmented zone apertures, 75% apodized hybrid designs with circular apertures, and for traditional photon sieve.

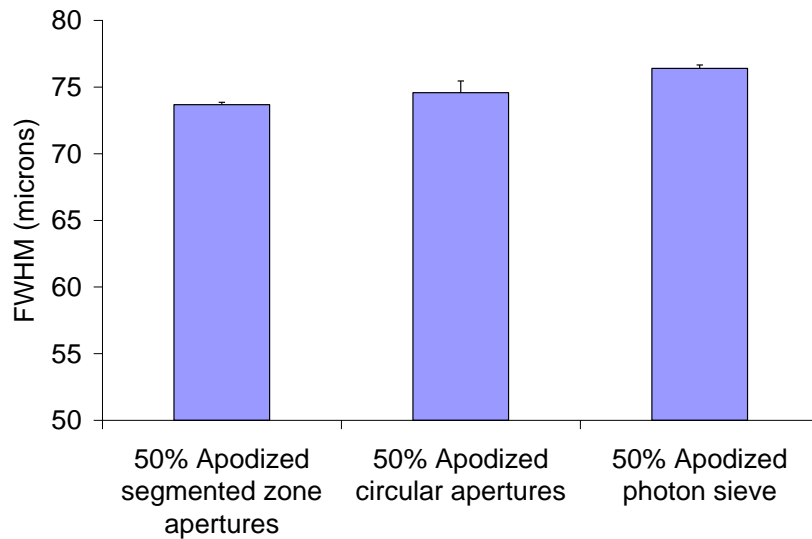


Figure 4-47. Measured FWHM of peak intensity for 50% apodized designs. Shown are FWHM for a 50% apodized hybrid design with segmented zone apertures, a 50% apodized hybrid design with circular apertures, and for a 50% apodized traditional photon sieve design.

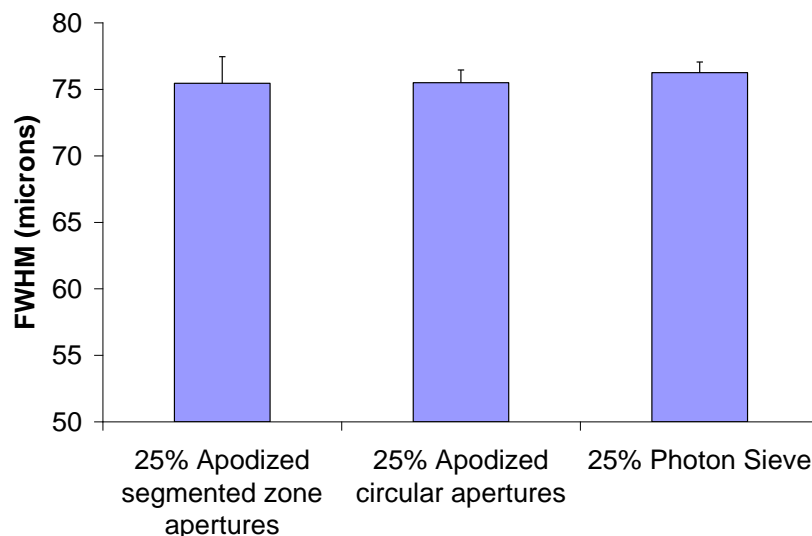


Figure 4-48. Measured FWHM of peak intensity for 25% apodized designs. Shown are FWHM for a 25% apodized hybrid design with segmented apertures, a 25% apodized hybrid design with circular apertures, and for a 25% apodized traditional photon sieve design.

As described in Section 4.2.1, all of the lens designs were tested using three pairs of $100\mu\text{m}$ apertures separated by $100\mu\text{m}$, $18\mu\text{m}$ and $0.5\mu\text{m}$ (Figure 4-4-b). As discussed in Chapter 2, the Rayleigh criterion can be used to define the limits of resolution. The Rayleigh criterion states the limit of the resolution of an optical instrument being used to image two adjacent apertures has been reached when the center of the diffraction pattern from one aperture overlaps the first minima of the diffraction pattern of the adjacent aperture. This condition occurs when there is a 26.5% reduction in intensity between the two maxima. Therefore, according to the Rayleigh criterion, the two apertures can be resolved if the reduction in intensity between the two maxima is 26.5% or greater. By this criterion, all of the lens designs successfully resolved the test aperture pairs separated by either $100\mu\text{m}$ or $18\mu\text{m}$. Just as in the case of FWHM data, all of the designs performed similar to one another with respect to this test of resolution. A representative example of the intensity distributions that resulted from the aperture pair test are shown in Figures

4-49 through 4-51. The intensity distributions are for the 75% apodized with segmented zone apertures with an aspect ratio of 4. The results for the other designs are compiled in Table 4-9.

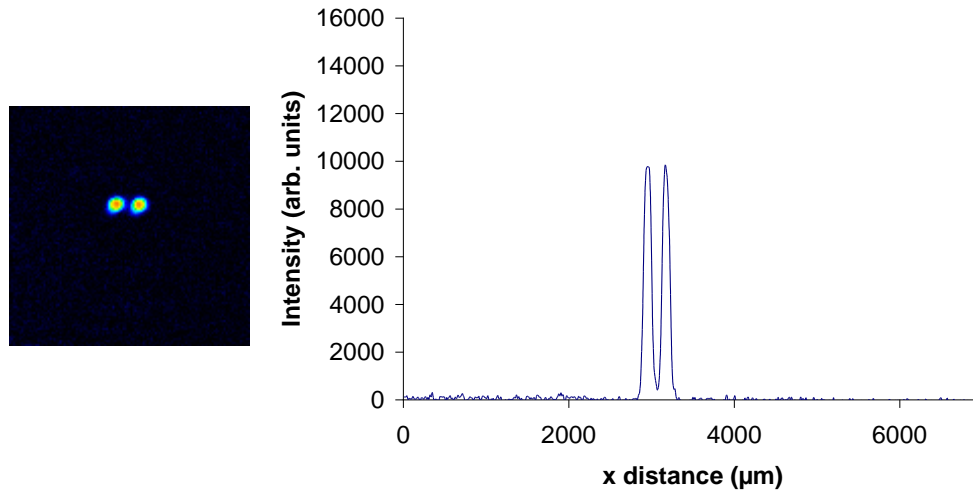


Figure 4-49. Resolution test of aperture pair with a 100μm separation for 75% hybrid apodized photon sieve with SZ apertures and aspect ratio of 4.

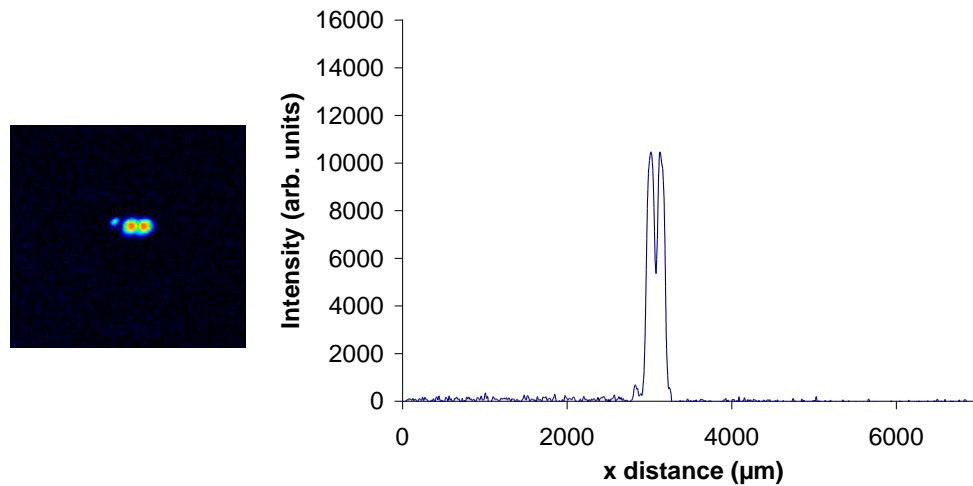


Figure 4-50. Resolution test of aperture pair with a 18μm separation for 75% hybrid apodized photon sieve with SZ apertures and aspect ratio of 4.

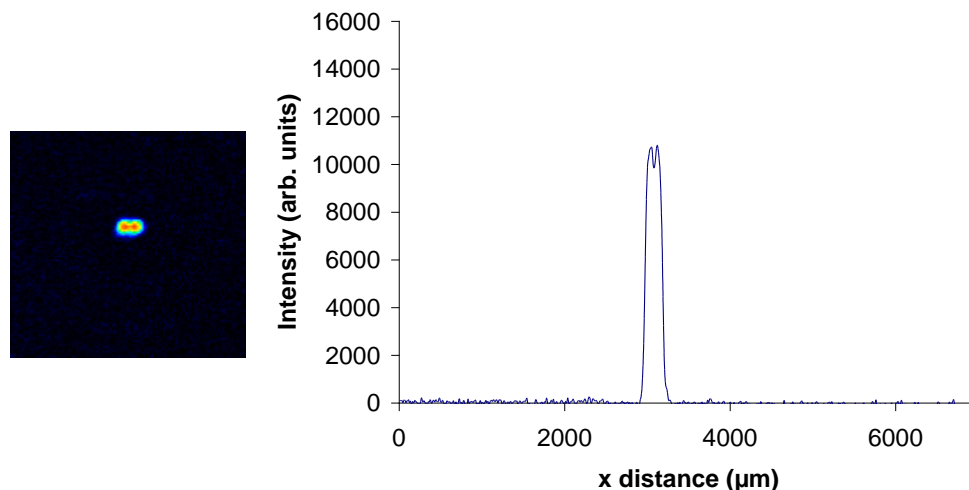


Figure 4-51. Resolution test of aperture pair with a $0.5\mu\text{m}$ separation for 75% hybrid apodized photon sieve with SZ apertures and aspect ratio of 4.

Table 4-8. Resolution Test

	Percent reduction in intensity between	Percent reduction in intensit	Percent reduction in intensity between
FZP	91	40	8
Unapodized PS	93	36	10
25% apodized PS	91	40	7
50% apodized PS	95	48	13
75% apodized PS	95	46	16
25% w/ circular apertures	93	40	7
50% w/ circular apertures	94	43	12
75% w/ circular apertures	96	46	15
25% w/ SZ aperture	92	38	8
50% w/ SZ aperture	96	45	9
75% w/ SZ aperture	97	50	9
AR=2	97	50	11
AR=3	96	48	11
AR=4	96	49	8

4.5 Summary and Conclusions

A variety of photon sieve designs have been developed and tested. All of the photon sieve designs shared a fixed outer diameter of 2.4mm and a resulting design focal length of 50.7mm at 700 nm or 51.1 mm at 688 nm. The focal length was measured using a narrow bandpass filter centered at 688nm, and the measured focal lengths were determined to be 51.1 ± 0.5 mm.

To minimize anticipated second order diffraction effects resulting from an abrupt termination of the diffraction apertures, photon sieves may be designed such that their open or transmitting area is gradually decreased, a process called apodization. For the photon sieve designs that were apodized, a cosine function was applied over the apodized zones, decreasing from the onset of apodization at $\cos 0^\circ$ to the edge of the photon sieve at $\cos 90^\circ$. For the designs tested, the secondary maxima were found to be <1% of the first order focused intensity and were therefore not important.

The FZP exhibited the largest transmissions and peak intensities of all designs. The hybrid PS designs with segmented zone apertures exhibited higher transmissions and peak intensities compared to the traditional PS designs and the hybrid designs with circular apertures, with a measured peak intensity that were 41%, 35%, and 34% higher than the measured peak intensities of the 25%, 50%, and 75% apodized traditional photon sieve designs respectively. The hybrid designs with large aspect ratio (~ 4) segmented zone apertures exhibited the largest relative increases in peak intensity, e.g. with intensities that were 55% higher than the 75% apodized traditional photon sieve design with circular apertures. The large aspect ratio designs also exhibited the smallest FWHM, with a 6% decrease in FWHM compared to the 75% apodized traditional photon sieve

design. The hybrid designs with large aspect ratio apertures achieved a reduction in FWHM, an increased transmission relative to the other 75% apodized designs. Therefore the hybrid designs incorporating large aspect ratio apertures satisfy the goals of improving the transmission of the photon sieve without degrading the resolution.

CHAPTER 5 CONCLUSIONS

5.1 Diffractive Lens Fabrication

A process to fabricate Fresnel zone plates and photon sieves has been developed and implemented. This multi step process consisted of 1) depositing thin metal films on a glass substrate using electron beam deposition, 2) depositing polymethylmethacrylate (PMMA) on the substrate using spin coating 3) patterning the PMMA using electron beam lithography 4) developing the patterned PMMA in a solution of methyl isobutyl ketone and isopropyl alcohol and 5) transferring the pattern from the PMMA to the underlying metal thin film by argon sputter etching. Literature and previous work had shown that PMMA suffers from poor etch resistance and typically leaves residuals on the surface that can be difficult to remove. This poor etch resistance was proposed to be exacerbated in part by heat build up in the substrate resulting from the ion bombardment. Avoiding heat buildup by splitting the etch into several shorter etch steps was found to improve PMMA effectiveness as a mask. Using acetone at room temperature had proven to be successful at removing PMMA under most circumstances. However, when the PMMA had been subjected to extended exposure, either from the electron beam or from ion bombardment, acetone failed to completely remove all of the PMMA. In these instances using a photoresist stripper at elevated temperatures proved to be an effective means of removing the hardened PMMA.

5.2 Diffractive Lens Properties

A variety of diffractive lens designs have been studied. These designs include a Fresnel zone plate, both unapodized and partially apodized traditional photon sieve designs, hybrid photon sieves which incorporate some of the completely open zones of the Fresnel zone plate for a portion of their area, hybrid photon sieves with segmented zone apertures, and hybrid photon sieves incorporating segmented zone apertures of varying aspect ratios.

Although the measured focal lengths did deviate slightly from the design focal length, the deviation was typically very slight, with the largest deviation being no larger than 2.2% from the design focal length. The deviation could be explained in part by the difference in the wavelength used from the design wavelength. The design wavelength was 700nm; however the wavelength actually used was 688nm. When this difference wavelength of the incident illumination is taken into account the difference in calculated focal length and measured focal length is reduced to 1.3%. This difference can be attributed to several factors not accounted for in the calculated focal length. These factors include refraction in the glass substrate and a non ideal source of illumination. The hybrid PS designs with segmented zone apertures exhibited higher transmissions and peak intensities compared to the traditional PS designs and the hybrid designs with circular apertures, with measured peak intensities that were 41%, 35%, and 34% higher than the measured peak intensities of the 25%, 50%, and 75% apodized traditional photon sieve designs respectively. The hybrid designs with large aspect ratio (~4) segmented zone apertures exhibited the largest relative increases in peak intensity, e.g. with intensities that were 55% higher than the 75% apodized traditional photon sieve design with circular

apertures. The large aspect ratio designs also exhibited the smallest FWHM, with a 6% decrease in FWHM compared to the 75% apodized traditional photon sieve design.

5.3 Conclusions

A relatively simple process to fabricate thin film diffractive lens has been developed and successfully implemented in the fabrication of photon sieves. The hybrid photon sieve designs with segmented zone apertures exhibited an increased transmission and an increase first order focus intensity compared to the traditional photon sieve design. This was achieved without any loss of resolution as demonstrated by measurements of the FWHM of the various designs and imaging of a resolution test sample. The hybrid photon sieve design incorporating large aspect ratio segmented zone apertures represents an improvement over the traditional photon sieve design with a 55% increase in intensity and a 6% reduction in FWHM compared to the traditional photon sieve.

CHAPTER 6 FUTURE WORK

Several directions for further research are interesting for future work. Several assertions made in the course of this research are speculative and warrant further investigation. With regards to the fabrication process, the observation that the PMMA suffered from degradation that was exacerbated by the heating of the substrate fit with observations in the course of the experiment and reports in the literature that PMMA etch resistance reduced with increase temperature, however it would be interesting to actually measure the etch resistance as a function of substrate temperature to confirm this speculation. The assertions that the differences in refractive indices from one side of the photon sieve to the other and the non-planar nature of the incident illumination also warrant further investigation. This could be accomplished by using an index matching fluid or applying a film with a similar refractive index to that of glass and by modifying the optical bench setup to incorporate a planar source.

It was observed that prolonged submersion of the sample in the Posistrip EKC830 at elevated temperatures resulted in discoloration of the silver surface. Although this does not occur in the time span required to remove the residue PMMA, it is indicative of some attack by the Posistrip on the silver surface and also warrants further investigation.

One of the advantages of the photon sieve theoretically lies in its ability to reduce secondary maxima through appropriate application of an apodization scheme. When the photon sieve is used as a lens, this has been reported to result in an improvement in the contrast of the image. It would be interesting to image the intensity distribution at the

focal plane to investigate how the design variations implemented in this research affected the intensity of the secondary maxima and subsequently the contrast in the image. This would require use of photographic film, since digital detectors lack the dynamic range to capture the peak intensity at the first order maxima, as well as the secondary maxima.

All of the photon sieve designs fabricated and tested in this research maintained a d/w ratio of 1, where d is the diameter of the pinhole aperture and w is the width of the underlying zone. Because the photon sieve designs were relatively small, the advantages arising from using large d/w ratio would not be realized. It would be interesting to fabricate a series of larger photon sieves and compare traditional designs consisting of circular apertures with d/w ratios of unity close to the center and larger d/w ratio apertures at the outer extents to a hybrid design incorporating segmented zone apertures with large aspect ratios close to the center and circular apertures with larger d/w apertures at the outer extents.

It would also be interesting to attempt to fabricate a series of such photon sieves using a metal foil or metal membrane rather than using a thin film applied to a glass substrate to compare the savings in weight that result. Fabricating the photon sieve in a metal foil would result in media with the same indices of refraction on the incident and transmitting sides of the photon sieve and therefore alleviate any reduction in image quality results from refraction in a substrate.

It was also observed that the FWHM in the x direction consistently differed from the FWHM in y direction, with the FWHM_x being, on average, 11% larger than the FWHM_y . This was speculated to be the result of symmetrical placement of the apertures in the zone which occur as a result of the macro used to generate the designs and is

especially discernable in the SEM micrographs of the large aspect ratio segmented aperture designs (Figures 4-36 to 4-39). The macro generated the distribution of apertures in a zone by creating a single aperture and then filling the zone with copies of that initial aperture. The symmetrical placement resulted because the macro placed all of the initial apertures for the zone along the same radial line. Using a random placement of the initial aperture would break this symmetrical distribution and result in a more consistently circular intensity distribution at the focal plane, i.e. the FWHM in the x and y directions would be in better agreement.

APPENDIX A
MACROS USED TO GENERATE PATTERNS

Fresnel Zone Plate Macro

```
/* opens a text file containing dimensions of a Fresnel zone plate*/  
open "i", 1, "f50mm_d3mm_m64_l695nm.fzp"  
  
/* a counter used to limit the number of zones in the zone plate*/  
p=0  
  
do while p<20  
  
/*read values from the open files specifying the location of the beginning and ending  
edges of even zones*/  
input #1, x, y,  
  
/*define z, the width of the zone*/  
z=y-x  
  
/*define r, the radial distance from the center of the zone plate to the mid point of the  
current zone*/  
r=x+(z/2)  
  
/* write a transparent zone of radius r, width z*/  
>Circle4  
{  
    <Color 0, 255, 255  
    <Linestyle 0, 1, [z]  
    <Type 0  
    <Radius [r]  
    <Pointxyz 0, 0, 0  
    <Pointxyz 0, 0, 0
```

```
<Pointxyz 0, 0, 0
}
/*calculate the are of the transparent zone*/
g=3.1415926535897932384626433832795*(sqr(y)-sqr(x))

/*add the area of the transparent zone to the total transparent area*/
h=g+h

/*iterate the counter*/
p=p+1
loop

/* display the calculated transparent area of the zone plate*/
t$= h, "square microns is the total transmitting area"
>Text
{
  <color 100, 100, 100
  <style 2
  <justification 1
  <size 25
  <font "Courier New"
  <text [t$]
  <angle 0
  <Pointxyz 0, 700, 0
}
```

Photon Sieve Macro

```

/* opens a file for input, the file contains dimensions of a Fresnel zone plate*/
open "i", 1, "f50mm_d3mm_m64_l695nm.fzp"

/*opens a file to output data*/
open "o", 2, "25percentapod_ps50mm_d3mm_m64_l695nm-02-12-06.area"

/* a counter used to limit the number of zones used*/
p=0

/* a counter used to vary the onset of apodization*/
q=1

/* a counter used to keep track of how many zones have been apodized*/
t=1

/*main body of the macro, fills each zone with aperatures until the 20th zone is filled*/
do while p<20

/*read values from the open files specifying the location of the beginning and ending
edges of even zones*/
input #1, x, y,

/*define r, half the width of the zone; also the radius of the circular apertures filling the
zone*/
r=(y-x)/2

/*define z, the distance from the origin to the middle of the zone*/
z=x+r

/*define c, the circumferential distance around the center of a zone*/
c=2*3.1415926535897932384626433832795*z

/*test if condition for onset of apodization is met*/

```

```

if q>15 then
  /*determine number of apertures in the zone using an apodization scheme based on
  cosine distribution*/
  n=cos(90*t/6)*(c/(2*r+1))

  /*update apodization counter*/
  t=t+1

else

  /*determine number of apertures in the zone with no apodization applied*/
  n=c/(2*r+1)

endif

/*this conditional is a work around inserted to avoid a limitation of DesignCad which only
allows the Circular Array command to process a maximum of 198 elements*/
if n<197 then

>Circle4
{
  <Color 0, 255, 255
  <Linestyle 1, 1, 0
  <Layer 1
  <Type 1
  <Radius [r]
  <Pointxyz [z], 0, 0
  <Pointxyz 0, 0, 0
  <Pointxyz 0, 0, 0

}

/*selects the aperture just created*/
>pointselect
{
<pointxyz [x],0,0

```

```

}

/*fills the zone with aperatures*/
>circulararray
{
    <angle 360
    <axis 2
    <ncopy [n]
    <offset 0
    <pointxyz 0, 0, 0
}

/*calculates the area of all of the aperatures in the zone*/
a=n*3.1415926535897932384626433832795*sqr(r)

/*send calculated area and zone number to output file*/
print #2, a,    p

/*total area of all of the zones*/
b=a+b

/*conditional section to address DesignCad limitation. If the number of aperatures in the
zone exceeds the maximum number of elements allowed by DesignCad, the zone is split
into four parts*/

else

>Circle4
{
    <Color 0, 255, 255
    <Linestyle 1, 1, 0
    <layer 2
    <Type 1
    <Radius [r]

```

```
<Pointxyz [z], 0, 0
<Pointxyz 0, 0, 0
<Pointxyz 0, 0, 0

}

e=n*3.1415926535897932384626433832795*sqr(r)

print #2, e,    p

f=e+f
m=n/4
>pointselect
{
<pointxyz [x],0,0
}

>circulararray
{
    <angle 90
    <axis 2
    <ncopy [m]
    <offset 0
    <pointxyz 0, 0, 0
}
endif
q=q+1
p=p+1
loop

layer(2)=14
layer(1)=0
>selectall
{
}
```

```
>circulararray
{
    <angle 360
    <axis 2
    <ncopy 4
    <offset 0
    <pointxyz 0, 0, 0

}
layer(1)=6

/*total area of aperatures*/
k=b+f

/*sends total open area of sieve to outputfile*/
print #2, k,
```

LIST OF REFERENCES

1. J.R. Meyer-Arendt, *Introduction to Classical and Modern Optics*. (Prentice Hall, Englewoodcliffs, 1989).
2. B Kress, *Digital diffractive optics : an introduction to planar diffractive optics and related technology*. (John Wiley, New York, 2000).
3. V. A. Soifer, *Methods for computer design of diffractive optical elements*. (Wiley New York, 2002).
4. A. Walther, *The Ray and Wave Theory of Lenses*. (Cambridge University Press, 1995).
5. Kostrzewa, W. Meyer, S. Laband, W. Terre, P. Petrovich, K. Swanson, C. Sundra, W. Sener, and J. Willmott, *SPIE's oemagazine* **4** (4), 31 (2004).
6. G. Andersen and D. Tullson, *Proceedings of SPIE* **6265**, 626523 (2006).
7. M. Barton, J. A. Britten, S. N. Dixit, L. J. Summers, I. M. Thomas, M. C. Rushford, K. Lu, R. A. Hyde, and M. D. Perry, *Appl. Opt.* **40** (4), 447 (2001).
8. D. Gil, R. Menon, and H. I. Smith, *J. Vac. Sci. Technol., B* **21**, 2810 (2003).
9. R. A. Hyde, *Appl. Opt.* **38** (19), 4198 (1999).
10. F. L. Pedrotti and L. S. Pedrotti, *Introduction to optics*. (Prentice Hall, New Jersey, 1987).
11. Kipp, M. Skibowski, R. L. Johnson, R. Berndt, R. Adelung, S. Harm, and R. Seemann, *Nature* **414** (6860), 184 (2001).
12. S. Patel, J. Marshall, and F. W. Fitzke 3rd, *J. Refract. Surg.* **11** (2), 100 (1995).

13. E. Hecht, *Optics 2nd edition*. (Addison-Wesley Publishing Company, Reading, 1987).
14. St. Luke's Cataract & Laser Institute. *Eye Anatomy*. Retrieved October 12, 2006 from <http://www.stlukeseye.com/Anatomy.asp>.
15. R. Waynant and M. Ediger, *Electro-optics Handbook*. (McGraw-Hill Inc., New York, 1994).
16. E. D. Palik, *Handbook of optical constants of solids*. (Academic Press, New York, 1985).
17. D. Malacara, *Handbook of lens design*. (Marcel Dekker, New York, 1994).
18. Laikin and L. Laikin, *Lens Design*. (CRC Press, 2001).
19. D. J. D. Carter, D. Gil, R. Menon, M. K. Mondol, H. I. Smith, and E. H. Anderson, *J. Vac. Sci. Technol., B* **17**, 3449 (1999).
20. Born and E. Wolf, *Principles of Optics: Electromagnetic Theory of Propagation, Interference and Diffraction of Light*. (Cambridge University Press, 1999).
21. C. R. Nave. *Fraunhofer diffraction geometry*. Retrieved December 10, 2005 from <http://hyperphysics.phy-astr.gsu.edu/hbase/phyopt/sinlitd.html#c1>.
22. C. R. Nave. *Single slit diffraction intensity*. Retrieved Decemeber 10, 2005 from <http://hyperphysics.phy-astr.gsu.edu/hbase/phyopt/sinint.html#c1>.
23. G. R. Fowles, *Introduction to Modern Optics*. (Holt, Rinehart and Winston, New York, 1968).
24. C. R Nave. *Double slit diffraction*. Retrieved Decemeber 10, 2005, from <http://hyperphysics.phy-astr.gsu.edu/hbase/phyopt/dslit.html#c1>.
25. Wes Wallace, Lutz H. Schaefer, and Jason R. Swedlow. *Resolution Criteria and Performance Issues*. Retrieved October 12, 2006 from <http://micro.magnet.fsu.edu/primer/digitalimaging/deconvolution/deconresolution.html>
26. Q. Cao and J. Jahns, *J. Opt. Soc. Am. A* **19** (12), 2387 (2002).

27. Q. Cao and J. Jahns, *J. Opt. Soc. Am. A* **20** (8), 1576 (2003).
28. Q. Cao and J. Jahns, *J. Opt. Soc. Am. A* **20** (6), 1005 (2003).
29. Q. Cao and J. Jahns, *J. Opt. Soc. Am. A* **21** (4), 561 (2004).
30. Q. Cao and J. Jahns, *Proceedings of SPIE* **6027**, 602702 (2006).
31. Z. Lin, H. Wang, C. Song, W. Ji, and B. Qi, *Proceedings of SPIE* **6149**, 61493A (2006).
32. R. Menon, D. Gil, G. Barbastathis, and H. I. Smith, *J. Opt. Soc. Am. A* **22** (2), 342 (2005).
33. G. Andersen, *Opt. Lett.* **30** (22), 2976 (2005).
34. S. T. Ridgway, *EAS Publications Series* **12**, 49 (2004).
35. G. E. Artzner, J. P. Delaboudiniere, and X. Song, *Proceedings of SPIE* **4853**, 158 (2003).
36. Guyon and S. Ridgway, *American Astronomical Society Meeting* **203**, 03.01 (2003).
37. M. Martinez-Corral, M. Kowalczyk, C. J. Zapata-Rodríguez, and P. Andrés, *Appl. Opt.* **37** (29), 6914 (1998).
38. Andres and M. Martinez-Corral, *Proceedings of SPIE* **4829**, 644 (2004).
39. Y. Bu, G. Wang, L. Yang, J. Wang, and Z. Xu, *Proceedings of SPIE* **3863**, 327 (2003).
40. R. H. Norton and R. Beer, *Optical Society of America, Journal* **66**, 259 (1976).
41. B. Tooke, V. Patel, K. P. Williams, and S. F. Parker, *Proceedings of SPIE* **1575**, 248 (2005).
42. Eric W. Weisstein *Apodization Function*. Retrieved October 12, 2006 from <http://mathworld.wolfram.com/ApodizationFunction.html>.

43. W. Chao, B. D. Harteneck, J. A. Liddle, E. H. Anderson, and D. T. Attwood, *Nature* **435** (7046), 1210 (2005).
44. E. H. Anderson, D. L. Olynick, B. Harteneck, E. Veklerov, G. Denbeaux, W. Chao, A. Lucero, L. Johnson, and D. Attwood, *J. Vac. Sci. Technol., B* **18**, 2970 (2000).
45. G. Cheng, T. Xing, W. Lin, J. Zhou, C. Qiu, Z. Liao, Y. Yang, L. Hong, and J. Ma, *Proceedings of SPIE* **6517**, 651736 (2007).
46. J. Djomehri, T. A. Savas, and H. I. Smith, *J. Vac. Sci. Technol., B* **16**, 3426 (1998).
47. D. Gil, R. Menon, D. J. D. Carter, and H. I. Smith, *J. Vac. Sci. Technol., B* **18**, 2881 (2000).
48. D. Gil, R. Menon, X. Tang, H. I. Smith, and D. J. D. Carter, *J. Vac. Sci. Technol., B* **20**, 2597 (2002).
49. Menon, A. Patel, D. Chao, M. Walsh, and H. I. Smith, *Proc. SPIE* **5751**, 330 (2005).
50. Menon, A. Patel, D. Gil, and H. I. Smith, *Materials Today* **8** (2), 26 (2005).
51. H. I. Smith, *J. Vac. Sci. Technol. B* **14** (6), 4318 (1996).
52. Dixit, R. Hyde, A. Weisberg, J. Early, M. Rushford, and J. Britten, *43 rd AIAA/ASME/ASCE/AHS/ASC Structures, Structural Dynamics, and Materials Conference, Denver, CO* (2002).
53. Hsiu Hsin Chung, Dissertation, University of Florida, 2006.
54. P. Rai-Choudhury, *Handbook of microlithography, micromachining and microfabrication. Vol. 1, Microlithography*. (Spie Optical Engineering Press,; 1997).
55. W. Chen and H. Ahmed, *J. Vac. Sci. Technol., B* **11**, 2519 (1993).
56. W. Chen and H. Ahmed, *Appl. Phys. Lett.* **62** (13), 1499 (2006).
57. Zailer, J. E. F. Frost, V. Chabasseur-Molyneux, C. J. B. Ford, and M. Pepper, *Semiconductor Science and Technology* **11** (8), 1235 (1996).

58. C. Vieu, *Applied Surface Science* **164** (1), 111 (2000).
59. K. D. Schock, F. E. Prins, S. Strähle, and D. P. Kern, *J. Vac. Sci. Technol., B* **15**, 2323 (1997).
60. Thomas George, Richard Muller, Paul Maker, and David Barsic, NASA Technical Brief Report No. NPO-20649, 2000.
61. K. Mochiji, Y. Wada, and H. Obayashi, *Journal of the Electrochemical Society* **129** (11), 2556 (2006).
62. Erie Scientific Company, *Erie Electroverre Glass Specification Sheet*, Retrieved October 12, 2006 from <http://www.eriesci.com/custom/evr-tech.aspx>
63. K. Seshan, *Handbook of Thin-film Deposition Processes and Techniques: Principles, Methods, Equipment and Applications*. (Noyes Publications/William Andrew Pub., 2002).
64. J. F. O'Hanlon, *A User's Guide to Vacuum Technology*. (Wiley-Interscience, 2003).
65. INFICON. *INFICON Quartz Monitoring Crystals Specification Sheet*. Retrieved October 12, 2006 from <http://www.quartzmonitoringcrystals.com/en/crystals.html>
66. INFICON. *XTC/2 Deposition Controller Specification Sheet*. Retrieved from <http://www.inficonthinfilmdeposition.com/en/xtc2thinfilm.html>
67. Microchem Corporation. *PMMA Specification and Data Sheet*. Retrieved from http://www.microchem.com/products/pdf/PMMA_Data_Sheet.pdf
68. J.C. Nability, *Nanometer Pattern Generation System*. Retrieved from <http://www.jcnability.com/>
69. Ted Pella Incorporated. *Gold on carbon SEM resolution specification*. Retrieved from http://www.tedpella.com/technote_html/617%20TN.pdf.
70. J. I. Goldstein, *Scanning electron microscopy and X-ray microanalysis*. (Plenum Press New York, 1992).
71. Smith College. *Scanning Electron Microscope (SEM) Machine Variables*. Retrieved October 12, 2006 from <http://131.229.114.77/microscopy/semvar.html>

72. Y. W. Yau, R. F. W. Pease, A. A. Iranmanesh, and K. J. Polasko, *J. Vac. Sci. Technol.* **19**, 1048 (1981).
73. M. A. McCord and T. H. Newman, *J. Vac. Sci. Technol., B* **10**, 3083 (1992).
74. M. Parikh, *J. Vac. Sci. Technol.* **15**, 931 (1978).
75. H. Eisenmann, T. Waas, and H. Hartmann, *J. Vac. Sci. Technol., B* **11**, 2741 (1993).
76. K. Harafuji, A. Misaka, K. Kawakita, N. Nomura, H. Hamaguchi, and M. Kawamoto, *J. Vac. Sci. Technol., B* **10**, 133 (1992).
77. K. D. Cummings, R. C. Frye, and E. A. Rietman, *Appl. Phys. Lett.* **57** (14), 1431 (2006).
78. B. D. Cook and S. Y. Lee, *J. Vac. Sci. Technol., B* **11**, 2762 (1993).
79. J. C. Jacob, S. Y. Lee, J. A. McMillan, and N. C. MacDonald, *J. Vac. Sci. Technol., B* **10**, 3077 (1992).
80. G. Owen and P. Rissman, *J. Appl. Phys.* **54** (6), 3573 (2006).
81. M. A. Gesley and M. A. McCord, *J. Vac. Sci. Technol., B* **12**, 3478 (1994).
82. L. Alford, P. Nguyen, Y. Zeng, and J. W. Mayer, *Microelectronic Engineering* **55** (1-4), 383 (2001).
83. L. Gao, J. Gstoettner, R. Emling, P. Wang, W. Hansch, and D. Schmitt-Landsiedel, *MRS Proc.* (2004).
84. P. Nguyen, Y. Zeng, and T. L. Alford, *J. Vac. Sci. Technol., B* **19**, 158 (2001).
85. P. Nguyen, Y. Zeng, and T. L. Alford, *J. Vac. Sci. Technol., B* **17**, 2204 (1999).
86. LS1 Specification Sheet Available at <http://www.oceanoptics.com/products/ls1.asp>, (2006).

87. Edmund Industrial Optics. *Narrow Bandpass filter Specifications*. Retrieved October 12, 2006, from <http://www.edmundoptics.com/onlinecatalog/displayproduct.cfm?productID=1903&search=1>
88. DataRay Coporation. *WinCamD Specification Sheet*. Retrieved October 12, 2006 from http://www.dataray.com/pdf/WinCamD_Uxx_Datasheet.pdf

BIOGRAPHICAL SKETCH

Narada Muni Bradman was born in Coconut Grove, Florida on September 26, 1978. Although he grew up in a variety of places across the United States including Los Angeles and upstate New York, the majority of his childhood was spent in Miami Florida.

He was home schooled and as a result, virtually all of his pre-collegiate education was received from his parents. In 1995, he acquired both his General Education Diploma from the State of Florida and his Associates of Arts from Miami Dade Community College. He attended Florida International University from 1995 to 1998, when he graduated with a Bachelor of Science in mechanical engineering. During his undergraduate studies, he interned at Lawrence Livermore National Laboratory, in Livermore California, where he worked on several projects including designing renewable energy capture and storage systems optimized for remote communities. He was admitted to the University of Florida, Department of Material Science and Engineering in June of 2001 and joined Dr. Paul Holloway's research group. While a member of Dr. Holloway's research group, he worked on several projects including a testing of a MEMs optical shutter, modeling the behavior of an HgI detector and designing and optimizing thin film diffractive lens for focusing visible and NIR wavelengths. He received his Ph.D from the Department of Materials Science and Engineering at the University of Florida under the advisement of Dr. Paul H. Holloway in August 2007.